

Award Number: DAMD17-02-1-0593

TITLE: X-ray Polarization Imaging

PRINCIPAL INVESTIGATOR: Andrew D. Maidment, Ph.D.

CONTRACTING ORGANIZATION: University of Pennsylvania
Philadelphia, PA 19175

REPORT DATE: July 2006

TYPE OF REPORT: Final

PREPARED FOR: U.S. Army Medical Research and Materiel Command
Fort Detrick, Maryland 21702-5012

DISTRIBUTION STATEMENT: Approved for Public Release;
Distribution Unlimited

The views, opinions and/or findings contained in this report are those of the author(s) and should not be construed as an official Department of the Army position, policy or decision unless so designated by other documentation.

REPORT DOCUMENTATION PAGE

Form Approved
OMB No. 0704-0188

Public reporting burden for this collection of information is estimated to average 1 hour per response, including the time for reviewing instructions, searching existing data sources, gathering and maintaining the data needed, and completing and reviewing this collection of information. Send comments regarding this burden estimate or any other aspect of this collection of information, including suggestions for reducing this burden to Department of Defense, Washington Headquarters Services, Directorate for Information Operations and Reports (0704-0188), 1215 Jefferson Davis Highway, Suite 1204, Arlington, VA 22202-4302. Respondents should be aware that notwithstanding any other provision of law, no person shall be subject to any penalty for failing to comply with a collection of information if it does not display a currently valid OMB control number. **PLEASE DO NOT RETURN YOUR FORM TO THE ABOVE ADDRESS.**

1. REPORT DATE (DD-MM-YYYY) 01-06-2006		2. REPORT TYPE Final		3. DATES COVERED (From - To) 24 Jun 20902 – 23 Jun 2006	
4. TITLE AND SUBTITLE X-ray Polarization Imaging				5a. CONTRACT NUMBER	
				5b. GRANT NUMBER DAMD17-02-1-0593	
				5c. PROGRAM ELEMENT NUMBER	
6. AUTHOR(S) Andrew D. Maidment, Ph.D. E-Mail: Andrew.Maidment@uphs.upenn.edu				5d. PROJECT NUMBER	
				5e. TASK NUMBER	
				5f. WORK UNIT NUMBER	
7. PERFORMING ORGANIZATION NAME(S) AND ADDRESS(ES) University of Pennsylvania Philadelphia, PA 19175				8. PERFORMING ORGANIZATION REPORT NUMBER	
9. SPONSORING / MONITORING AGENCY NAME(S) AND ADDRESS(ES) U.S. Army Medical Research and Materiel Command Fort Detrick, Maryland 21702-5012					
10. SPONSOR/MONITOR'S ACRONYM(S)				11. SPONSOR/MONITOR'S REPORT NUMBER(S)	
13. SUPPLEMENTARY NOTES- original document contains color					
14. ABSTRACT Conventional mammography evaluates the spatial arrangement of tissue in the breast; the recorded signal is determined by the x-ray attenuation of the materials in each projection. Due to the low x-ray energy, every x-ray attenuated by the breast is absorbed by the breast (i.e., all of the x-ray energy is deposited in the breast). We have investigated whether it is possible to produce breast images based on x-ray polarization. Polarization radiography appeared to have the potential to supplement mammographic images by imaging the ability of breast tissue to rotate the x-ray polarization vector. We had hoped that new information about the breast could be gleaned at a low dose to the breast; preference being given to x-rays which would pass through the breast and have altered polarization, rather than being absorbed by the breast). We performed fundamental experiments regarding x-ray polarization to determine whether the polarization effect was sufficiently large to allow it to be used to produce images. Two different x-ray polarimeters were developed and tested. We were able to demonstrate polarization of the incident x-ray beam. However, neither polarimeter allowed successful measurement of polarization alterations of any material. We did, however, develop an excellent model of x-ray spectra, which has already seen wide usage.					
15. SUBJECT TERMS Breast Cancer, Mammography, X-ray Polarization					
16. SECURITY CLASSIFICATION OF:			17. LIMITATION OF ABSTRACT	18. NUMBER OF PAGES	19a. NAME OF RESPONSIBLE PERSON USAMRMC
a. REPORT U	b. ABSTRACT U	c. THIS PAGE U			19b. TELEPHONE NUMBER (include area code)

Table of Contents

Introduction.....	4
Body.....	5
Key Research Accomplishments.....	26
Reportable Outcomes.....	27
Conclusions.....	29
References.....	30
Appendices.....	32

Introduction

At optical energies, the polarization of light passing through biological tissue is altered. X-rays are similarly transverse waves; thus, one can preferentially produce x-rays in one polarization state. In this grant, we hypothesized that the polarization of x-rays passing through tissue might be altered in a detectable manner. Since x-rays are capable of passing through many inches of tissue, changes in the polarization state can reflect information about the tissue deep inside the body.

Conventional mammography only evaluates the spatial arrangement of tissue in the breast, as it depends upon the fact that some materials attenuate and absorb x-rays more than other materials (the x-ray energy must be deposited in the body to produce an image). If our hypothesis had proved true, polarization radiography would have had the potential to supplement mammographic images with information about the function, composition, and/or metabolism of the breast. Additionally, the ability to rotate the polarization of x-rays is conferred by the passage of the x-rays through the body, not the attenuation of the x-rays in the breast. Thus, while speculative, it might be possible to significantly reduce the dose needed to image the breast if a polarization imaging system could be developed.

In this grant, we proposed to investigate the potential of x-ray polarization imaging. We proposed to build an x-ray polarimeter (a device designed to measure polarization) and determine the factors that affect its design. In the end, we built and tested two polarimeters; both designs functioned to the extent that they could be used to measure the polarization of the incident x-ray beam. However, neither design was capable of measuring polarization changes from any material. Our original design lacked the angular precision needed for the measurement. Our second design lacked adequate photon fluence. This work did, however, contribute to our knowledge of (1) the polarization of x-ray tubes; (2) modeling the spectra of x-ray tubes; (3) methods for producing near mono-energetic x-ray spectra for breast imaging; (4) the mechanisms of contrast in radiography (especially of the breast); and (5) the mechanisms of polarization at x-ray energies. This work has led to new innovations in developing imaging contrast agents. In addition, some potential avenues for future research of polarization radiography have come to light; however, it is likely that x-ray polarization research is best done with a synchrotron light source.

This research, while quite fundamental in its nature, had the potential for a significant impact in breast cancer diagnosis. The use of effects related to the polarization of x-rays largely remains an unexplored field. However, based on our research, the use of polarization imaging is not likely to be clinically realizable.

Report Body

1. Statement of Work

The work for this grant was divided into four tasks. They are outlined as follows:

Task 1: Design and Develop X-ray Polarimeter

The initial task in this project was to design and build a polarimeter. The polarimeter design should give consideration to: (1) the mechanical gantry; (2) the x-ray tube and generator; (3) the analyzer crystal; (4) the beam stop and shielding; (5) the detector and associated electronics; and (6) control and analysis software.

Task 2: Validate the Polarimeter Design

The polarimeter design needed to be calibrated and tested prior to full and independent operation. This components of the work included: (1) detector calibration; (2) data analysis validation; (3) measurement of detector linearity; (4) determination of polarization as a function of radiographic parameters; and (5) determination of the effect of binding energy on polarization.

Task 3: Tabulate optical activity for common materials

Catalog the optical activity of various biological and inorganic materials.

Task 4: Postulate the design of an imaging system(s)

Using the information gathered above, we shall postulate upon the likelihood of success of polarization imagers, and evaluate a variety of possible designs.

2. Administrative Note

When first awarded, Dr. Maidment (the PI) was employed at Thomas Jefferson University. Effective February 1st, 2003, Dr. Maidment resigned his position at Thomas Jefferson University and began working at the University of Pennsylvania. At that time, Dr. Maidment requested that the grant be transferred to the University of Pennsylvania. The grant transfer was approved by the DOD in a letter dated April 14, 2004. A grant account at the University of Pennsylvania was formally opened on May 19, 2004, covering the period 01-Mar-04 to 26-June-06.

In January/February 2004, Dr. Maidment moved his laboratory from temporary quarters in the Stemmler Building, to permanent quarters in the Chemistry Building (Suites 283, 286 and 287, 34th and Spruce Streets). The suites encompass almost 1000 sq. ft. of office and laboratory space. The laboratory is lead-lined to allow x-ray experiments. The laboratory is equipped with excellent power and air conditioning systems, which are ideal for x-ray experiments. A new x-ray generator and x-ray tube were purchased for this project (by the University of Pennsylvania) as part of the move to the new facilities, in addition to other new laboratory equipment.

A number of people have worked on this project. The grant was used to provide salary support for Dr. Andrew Maidment, Dr. Michael Albert, Dr. Ann-Katherine Carton, and

Mr. Dhinakaren Chinappen. In addition, Dr. Harry Kao spent some time working on this project while being paid from University funds, and Mr. Raymond Acciavati worked on this project last summer as an AAPM Undergraduate Scholar. Dr. Michael Albert was responsible for the majority of the experimental work on the design, development and testing of the x-ray polarimeters. Dr. Carton was responsible for the modeling and experimental validation of the x-ray spectra. Mr. Acciavati worked with Dr. Carton on the spectral modeling.

The combination of moving the laboratory to the University of Pennsylvania; designing, building and moving into new laboratory space; obtaining appropriate equipment; and selecting appropriate people took some time, and significantly delayed the grant from its original time line. At the end of the grant period, Dr. Albert resigned from the University of Pennsylvania. As a result, the final report for the grant was delayed.

3. Background:

3.1. Polarization and Optical Activity:

The term optical activity derives from the interaction of chiral materials with polarized light. An enantiomer can be named by the direction in which it rotates the plane of polarized light. A solution of the (–)-enantiomer rotates the plane of polarization of a beam of plane polarized light in a counterclockwise direction, while for the (+)-enantiomer rotation is clockwise. Many biologically-active molecules are chiral, including the naturally-occurring amino acids (and hence proteins), and sugars. In biological systems most of these compounds are of the same chirality: most amino acids are L and sugars are D. As a result, most biological materials are optically active to visible light.

Like other materials, optically active materials can refract, absorb and scatter light; however, such materials demonstrate a different response to radiation depending upon whether the radiation is left or right circularly polarized. The differential absorption of light of these two polarizations is called circular dichroism, and the differential refraction is called circular birefringence, which for plane-polarized light is observed as optical rotation. Plane polarized light is composed of equal amplitudes of left- and right-polarized light. The magnitude of the optical rotation of plane-polarized light is proportional to the difference between the indices of refraction for left and right circularly polarized light and the thickness of the optically active material.

For some time, we have been developing methods to determine the composition of breast calcifications *in vivo*. Breast calcifications are one of the primary markers of both benign and malignant diseases in mammograms. Calcifications can be divided into two broad categories: Type I are composed of weddellite (calcium oxalate dihydrate) and whewellite (calcium oxalate monohydrate); all type II calcifications have some phosphorus content, most typically calcium hydroxyapatite. Type II calcifications are known to be associated with carcinoma, while it is generally accepted that the exclusive finding of type I calcifications is indicative of benign lesions. Under polarized light, Type I calcifications are birefringent. One of our primary motivations for this work has been to determine whether we can distinguish between type I and type II calcifications based on optical activity at x-ray energies.

3.2. X-ray Polarization

Like other forms of electromagnetic radiation, x-ray photons can exhibit phenomena related to polarization. Bremsstrahlung x-rays produced by electrons accelerated from the cathode to the anode of an x-ray tube are partially plane-polarized with the electric field vector parallel to the cathode-anode axis [Dyson90, Agar79]. Classically, an accelerating or decelerating charged particle emits radiation whose electric field vector (at each point in space) is coplanar with the axis of acceleration or deceleration [Barut80, Rohr65, Schwing98, Jackson99]. The physical reason for this geometric fact is clearer in the related process of an electron being scattered by a photon, as it is the electric field of the incident (or emitted) photon which is chiefly responsible for accelerating (or decelerating) the electron. By way of comparison, synchrotrons produce coherent, circularly polarized radiation.

On the order of 5-10% of the Bremsstrahlung radiation from diagnostic x-ray tubes is polarized, with greater polarization for x-rays whose energy is nearly that of the incident electron. Lower energy x-rays are produced by processes in which the electron's direction might have changed prior to emission of the x-ray, and thus have less polarization. These effects were experimentally documented as early as 1905 [Barkla05], as reviewed in [Steve57]. More recent research has tended to deal with thin targets (for example, [Kuck73]) so that the kinematics at the interaction vertex are well defined. A measurement of polarization from a Phillips x-ray tube [Staun78], in a study aimed at crystallographic applications, showed general agreement with the older results. Similar agreement was reported in an abstract [Slivin71].

4. Results

As a brief summary, the tasks involved in this research are: develop a viable polarimeter design; characterize its operation and validate the results obtained; characterize and tabulate the optical activity of specific material; and use these data to develop a design for a x-ray polarization imaging system.

Unfortunately, as will be made clear in the detailed discussion of results (below), the development of an x-ray polarization imaging system based on conventional x-ray tubes does not appear to be practical. The vast majority of the time in this project was spent trying to develop a viable polarimeter. Ultimately, two different polarimeters were developed and tested. Both failed to demonstrate optical activity; one using a broad spectrum x-ray beam; the other using an essentially mono-chromatic x-ray spectrum. The first system (as originally proposed in the grant application) lacks sufficient angular resolution, while the second system (described and approved in our interim reports) ultimately lacked sufficient fluence to allow measurement of x-ray polarization.

That said, this project has not been without positive results. We have been able, by benefit of this grant, to contribute to the fields of (1) polarization of x-ray tubes; (2) modeling the spectra of x-ray tubes; (3) methods for producing near mono-energetic x-ray spectra for breast imaging; (4) mechanisms of contrast in radiography (especially of the breast); and (5) mechanisms of polarization at x-ray energies. This work has led us to conceive new innovations in developing imaging contrast agents. In addition, some potential avenues for future research of polarization radiography have come to light;

however, it is likely that x-ray polarization research is best done with a synchrotron light source. Thus, while we are disappointed that our original premise could not be developed to the extent originally planned, we believe that the research has ultimately had significant impact. While the departure of Dr. Albert from our lab near the end of this research project has delayed this report and our efforts at publication, Drs. Maidment and Carton are in the process of preparing papers for peer-review at this time.

4.1. Broad Spectrum X-ray Polarimeter

4.1.1 Polarimeter Design

The original premise of this grant was to develop a broad-spectrum x-ray polarimeter. While there are many ways to measure the polarization of mono-energetic x-ray beams, there is one prime method of measuring polarization of poly-energetic x-ray beams. This polarimeter design relies upon the angular distribution of the scattered beam to measure the polarization of the incident beam. Such a polarimeter is shown in Figure 1. It consists of a collimated x-ray tube, an analyzer, and two or more x-ray detectors at right angles. To measure polarization rotation by a sample material, the material must be placed in the primary beam, and the detectors must be mounted on a rotating gantry. In such experiments, the intensity of the scattered radiation recorded by the detectors would have a sinusoidal angular dependence.

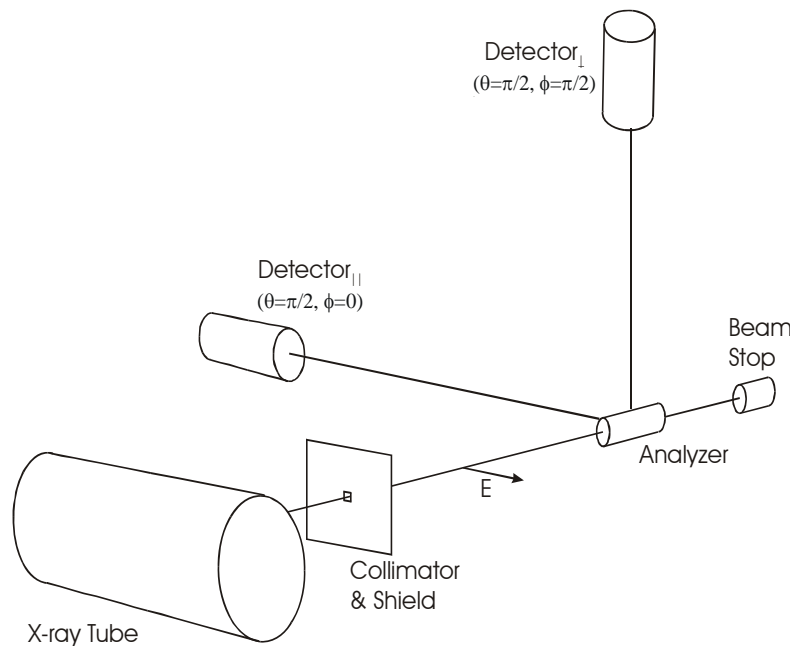


Figure 1: Schematic of the Broad-Spectrum Polarimeter

The angular dependence of x-rays scattered from a polarized beam can be understood at the classical level. If a plane-polarized wave is incident upon a charged particle, the resulting acceleration \mathbf{a} of the particle will be parallel to the electric vector \mathbf{E}_{in} of the incident wave. The electric field component of the resulting scattered radiation at a distance \mathbf{R} away from the scatterer in the direction $\hat{\mathbf{n}}$ (a unit vector) will be proportional

to $\vec{n} \times (\vec{n} \times \mathbf{a}) / \mathbf{R}$ [Barut80, Rohr65, Schwing98, Jackson99]. This formula has a simple geometric interpretation in that the electric field vector is proportional to the acceleration projected onto a plane perpendicular to the line of sight from the field point back to the scatterer. For a wave moving along the z-axis and plane polarized so that the electric vector lies along the x-axis (parallel to the anode-cathode axis), the angular distribution of scattered radiation per solid angle will have the form

$$d\Phi/d\Omega = r_o^2 [1 - \sin^2(\theta)\cos^2(\phi)]$$

where θ is the polar angle ($0 < \theta < \pi$) and ϕ is the azimuthal angle ($0 < \phi < 2\pi$).

The azimuthal variation is maximal for scattering at 90° relative to the incident radiation ($\theta = \pi/2$). In this plane, scattering would be 100% suppressed at $\phi = 0$ or π (the direction of the electric field vector \mathbf{E}_{in} of the incident beam) if the beam were completely polarized. For incompletely polarized beams, the azimuthal variation will be less pronounced. Using radiation scattered at 90° , if I_{\parallel} represents the intensity of the scattered radiation in the direction parallel to the preferred direction of the electric field vector ($\phi = 0$) and I_{\perp} represents scattering in the orthogonal direction ($\phi = \pi/2$), the degree of planar polarization of the incident beam can be quantified in terms of $P_{pol} = (I_{\perp} - I_{\parallel}) / (I_{\perp} + I_{\parallel})$ which would be 1 for a completely plane-polarized beam and is on the order of 0.05-0.1 for conditions similar to clinical x-ray tubes.

4.1.2 Poly-energetic Experiments:

Barkla [Barkla05] and others have demonstrated polarization of conventional x-ray tubes. However, such experiments have been chiefly concerned with the nature of the Bremsstrahlung process or, for the earliest experiments, the nature of x-rays themselves. Work on optical activity in the x-ray region has generally used low energy x-rays (< 1 keV). At the time of submission of the application for this grant, we were only aware of one measurement of optical activity at diagnostic energies is for quartz ($< 2^\circ \text{ cm}^{-1}$ at 19 keV) [Hart81]. While this experiment was conducted with monoenergetic x-rays, there was no reason to believe that the optical activity seen would be different at other energies in the diagnostic x-ray regime; quartz in and of itself does not have any materials with binding energies near 19 keV. This report now appears anomalous. Virtually all other reports would tend to indicate that observable polarization effects are related to phenomena associated with the binding of orbital electrons. As summarized by Creagh [Creagh99], “(polarization) is not very pronounced away from an absorption edge. Near an edge, the crystal field forces a symmetry on the scattering process”. However, that said, our initial experiments were based on the work of Hart and involved polyenergetic x-ray spectra./

We conducted experiments our first polarization experiments using an apparatus similar to that shown in Figure 1. The analyzer consisted of a Lucite rod 2.5 cm diameter, and 13 cm long. The analyzer was positioned 40 cm from a tungsten target x-ray tube (Siemens Bi 150/30/50R), operated at 100 kVp and 100 mAs. The x-ray beam was collimated by a 6 mm diameter circular aperture, located 20 cm from the x-ray source. Thus, the irradiating beam was 12 mm in diameter at the analyzer. Two ion chambers where mounted at right angles to the beam, and at right angles to each other ($\theta = \pi/2$, $\phi = 0$

and $\pi/2$), 60 cm from the analyzer. The primary photon fluence incident upon the analyzer was estimated to be 2×10^{11} , while the scattered fluence at the detector in the direction perpendicular to polarization was $2 \times 10^6 \text{ cm}^{-2}$. We have thus observed x-ray polarization, measuring $P_{\text{pol}}=0.10$.

We have subsequently repeated these measurements upon moving to the University of Pennsylvania. In this instance, we used a specially constructed device. The system was based on a General Electric Senographe 500T, with a molybdenum target x-ray tube. The tube was operated within a shielded enclosure constructed for the purpose. (As an aside, this enclosure has proved to be extremely useful and has been used routinely for a variety of x-ray experiments since the completion of this grant). Typical operating conditions were 40 kVp and 200 mAs. In this instance, the fluence incident upon the analyzer was estimated to be on the order of 10^{11} photons and the polarization was measured to be $P_{\text{pol}}=0.08$.

Using the second system we developed at the University of Pennsylvania, we attempted to measure changes in the polarization of the x-ray beam. Introduction of materials between the x-ray source and the analyzer crystal failed to reveal any change in polarization. These measurements were hampered by the relatively significant attenuation that occurred with materials sufficiently thick to potentially induce a rotation of the polarization vector. As noted by Creagh [Creagh99], 18 of the 32 crystal groups will exhibit optical activity at x-ray energies. Fluids will similarly demonstrate optical activity if they lack a center of symmetry; these findings are independent of birefringence. However, birefringence results in a significantly larger optical effect than that of optical activity. As such, we chose to concentrate our evaluation of materials to those known to be highly scattering (such as wax, etc.) and calcium oxalate (both the mono- and dehydrate forms) which are known to be birefringent and of biological value in breast cancer research. No material tested showed the ability to alter the polarization of the x-ray beam.

These disappointing results ultimately led us to seek an alternative method for measuring polarization.

4.2. Pseudo Mono-energetic X-ray Polarimeter

4.2.1 Polarimeter Design

We have separately been examining the use of niobium as an x-ray filter. Niobium has a k-shell energy of 18.986 keV, which is between the $K\alpha$ ($K\alpha_1 = 17.4793 \text{ keV}$ and $K\alpha_2 = 17.3743 \text{ keV}$) and $K\beta$ (19.6083 keV) energies of molybdenum. The result is that the $K\alpha$ x-ray beam is more highly attenuated than the $K\beta$. Thus, a nearly mono-energetic x-ray beam can be produced. We have used this method to evaluate the coherent scatter of breast calcifications. This work, however, motivated us to consider methods of measuring x-ray polarization using a narrow range of x-ray energies.

Our second polarimeter design was based on a molybdenum x-ray source and a reflecting crystal placed at 45° to the x-ray beam. The complete polarimeter is shown in Figure 2. The polarimeter consists of an x-ray tube, a reflecting crystal, a series of collimators to

isolate the x-ray energy desired and to eliminate scattered radiation, a sample holder, and a detector consisting of an x-ray image intensifier and CCD camera.

The x-ray tube produces a poly-energetic spectrum. The silicon crystal reflects the $K\alpha$ radiation at ~ 90 degrees. Reflection of electromagnetic radiation at right angles results in complete polarization of the reflected beam. Thus, this method will lead to a polarized, mono-energetic beam, which can then be passed through a series of collimators to irradiate the test sample. The test sample then scatters the incident x-rays. The angular distribution of the scattered x-rays varies due to the x-ray polarization. The angular dependence scatter produces an image which is incident on the x-ray image intensifier (XRII) and then recorded by the CCD camera.

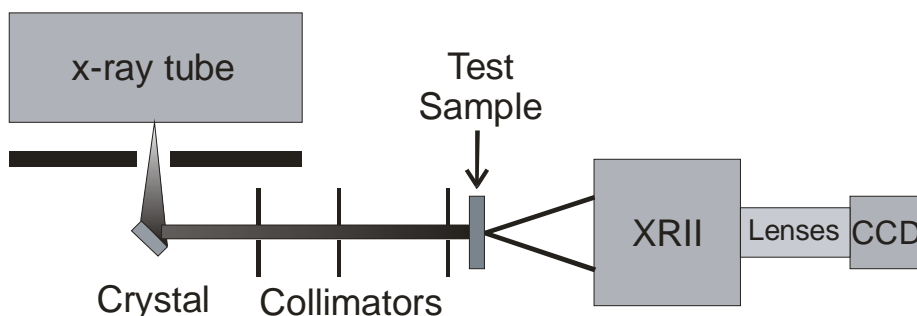


Figure 2: The schematic for the mono-energetic polarimeter. The x-ray tube produces a poly-energetic spectrum. The crystal reflect the $K\alpha$ radiation (~ 17.3 keV) at 90 degrees. This polarized, mono-energetic beam is passed through a series of collimators and hits the test sample. The test sample then scatters the incident x-rays. The angular distribution of the scattered x-rays varies due to the x-ray polarization. This image is produced with the x-ray image intensifier (XRII) and then recorded by the CCD.

4.2.2 Mono-energetic Polarimeter Development

We considered two crystals. We first evaluated the idea using an existing calcite crystal available in the lab. Calcite will reflect the Mo $K\alpha$ radiation at a Bragg angle of $\sim 45^\circ$ (reflected beam is emitted at 90°) on the 11 0 1 plane of the crystal. Under these conditions, the reflected beam is nearly 100% polarized. We subsequently purchased a high-quality silicon wafer to further explore this method of polarimetry. We used a polished Si wafer, 1 mm thick, with a $\langle 111 \rangle$ crystal orientation (Cemat Silicon SA, Warsaw, Poland). Silicon will reflect the Mo $K\alpha$ radiation at a Bragg angle of $\sim 45^\circ$ (reflected beam is emitted at 90°) on the 11 11 11 plane of the crystal. Again, this beam should be essentially 100% polarized.

Our initial work on this method was performed with calcite crystals. We had appropriate crystals available in the lab. The goal of this work was to ensure that the $K\alpha$ and $K\beta$ characteristic radiation lines were separable. A sample image of the reflected x-ray beam from a calcite crystal is shown in Figure 3. The image shows a series of lines corresponding to the reflected $K\alpha$ and $K\beta$ characteristic radiation lines; double lines correspond to the $K\alpha_1$ and $K\alpha_2$ radiation, single lines to the $K\beta$. A vertical profile through this image (figure 4) shows that the addition of a niobium filter has the effect of

preferentially removing the $k\beta$ radiation. This motivated us to continue in this direction using a higher quality crystal.

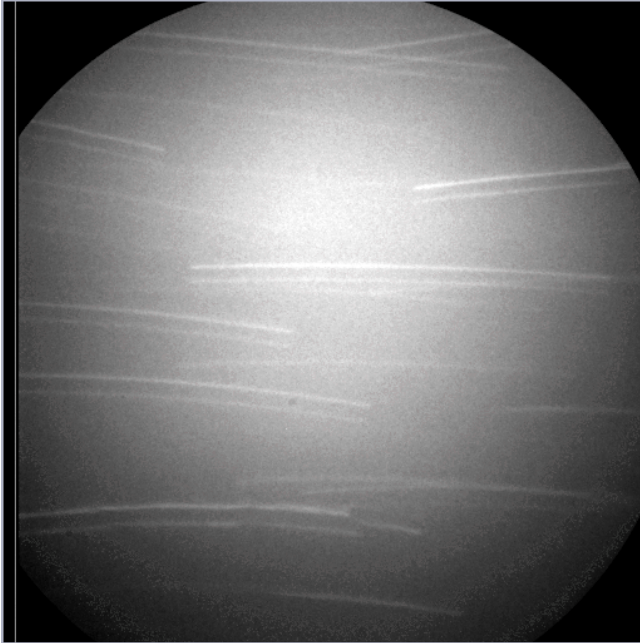


Figure 3: An image of the reflected x-ray beam without intervening collimation. The $K\alpha$ lines are clearly seen. Multiple lines are seen due to imperfections in the calcite crystal. A cross-section through this image and a similar image filtered with niobium is shown in Figure 5.

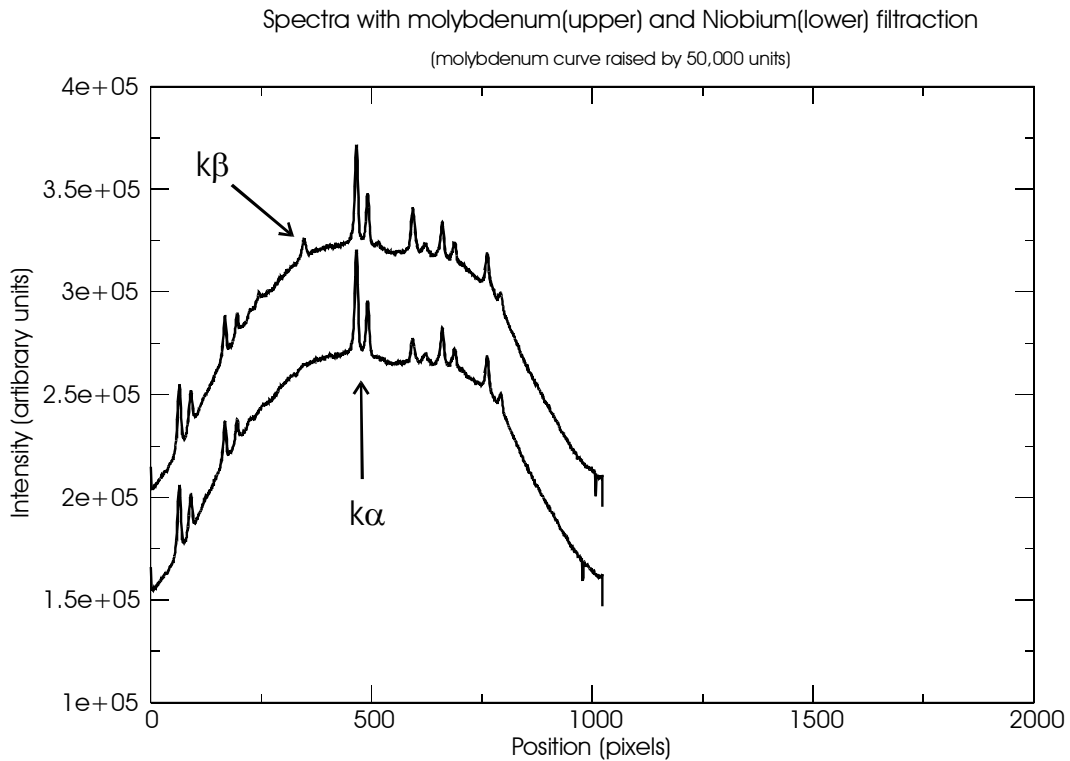


Figure 4: The intensity of as a function of position across the x-ray detector. The two graphs differ by the beam filtration. One allows $k\beta$ radiation to be imaged, the other does not. Note that the $k\beta$ lines are missing in the one graph. The two graphs are displaced for illustrative purposes only. Due to imperfections in the crystal used, there are multiple replicates of the K lines.

At this point, we conducted fluence estimates to determine the viability of this technique. For a 40 keV Mo beam, the $K\alpha$ radiation result in a dose of 125 $\mu\text{Gy}/\text{mAs}$ at 0.5 m. This corresponds to 1.5×10^{11} $K\alpha$ x-rays per steradian per mAs. The integrated reflection from the [11 0 1] plane is 9.5×10^{-8} radians (i.e., the crystal acts like a slit to select one energy from the spectrum). The result is a irradiating beam on the target material of 9.3×10^3 x-rays/radian/mAs. In our geometry, this results in a signal of 29 x-rays per mAs.

Experimentally, we observed a signal in the CCD (based on the above calculations) of 27 DV per x-ray. By comparison, calculation of the sensitivity of the imaging system based on optical and radiation measurements for a polyenergetic Mo spectrum resulting in a signal of 36 ± 6 DV/x-ray. The degree of consistency is high. For this reason, we continued to develop this technique using a better crystal.

Figure 5 shows the energy resolved x-ray spectra from a single crystal of silicon. The left image is acquired with the crystal at 45° . Multiple reflections of the $K\alpha$ and $K\beta$ lines of molybdenum from different crystal planes are shown. In addition, there is a general background signal from the molybdenum bremsstrahlung spectrum. The right image is acquired under the same geometry, with a niobium filter in the reflected beam. Now, the $K\beta$ lines (19.6083 keV) have been removed, as the k-edge of Niobium (18.986 keV) is of a lower energy. This is consistent with the results shown for calcite

Figure 6 shows a collimated image of the $K\alpha_1$ (17.4793 keV) and $K\alpha_2$ (17.3743 keV) characteristic radiation of Mo. The reflection is from the 11 11 11 crystal plane of the Si crystal, which for the $K\alpha_1$ reflection occurs at 45.9179° and for the $K\alpha_2$ reflection occurs at 46.2767° , thus the x-rays in this collimated beam are essentially 100% polarized. This (essentially) mono-energetic x-ray beam was then used measure the angular distribution of the scatter of a number of materials.

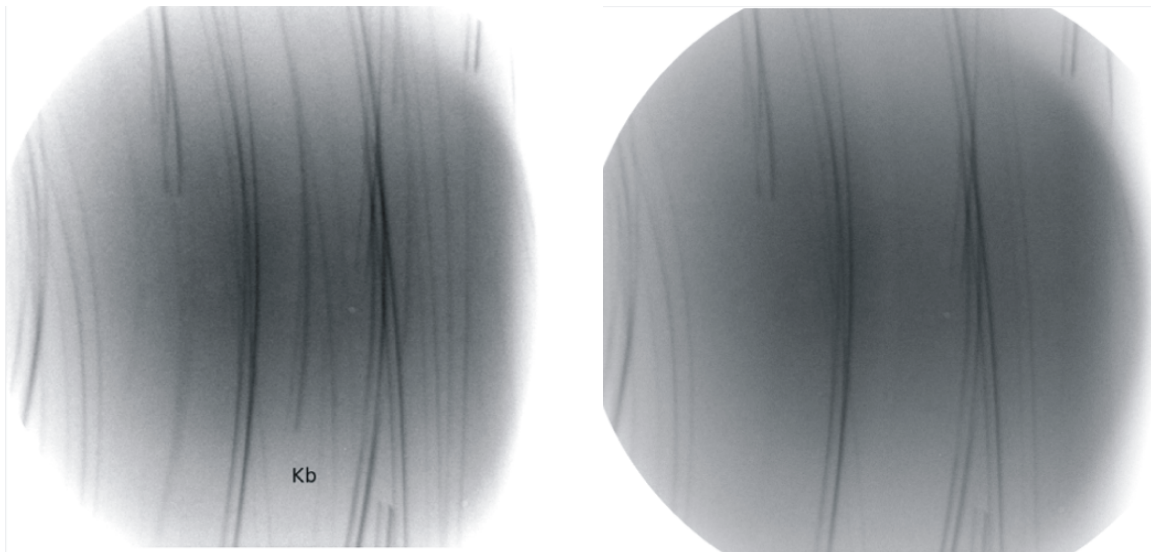


Figure 5: The intensity of radiation scattered from the Si crystal. Multiple $K\alpha$ and $K\beta$ lines of Mo are seen, as well as the background Bremsstrahlung radiation. The image on the left shows the unfiltered x-ray beam. The image on the right shows the beam filtered by 50 μm of Niobium, in which the $K\beta$ lines have been removed.

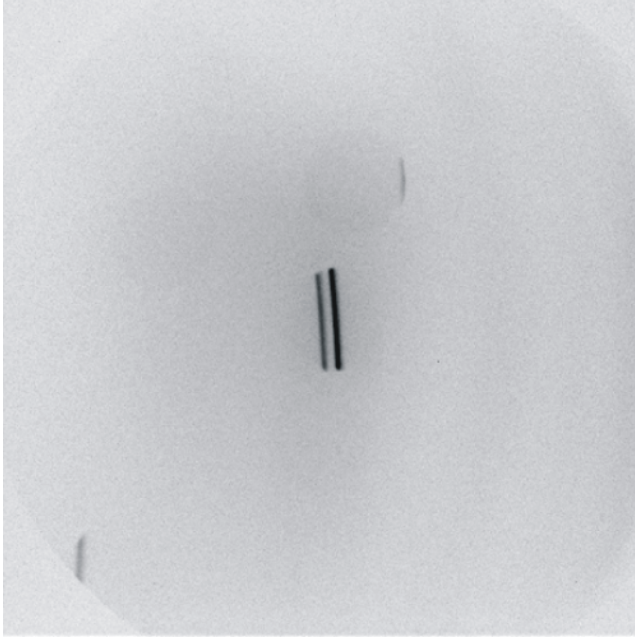


Figure 6: After insertion of collimators into the beam line, a small (highly magnified) image of the interrogating beam was produced. This beam was used to irradiate the test samples.

4.2.3 Mono-energetic Polarization Measurement

A series of experiments were conducted to determine whether the scatter distribution varies when materials are added to the x-ray beam, and whether this scatter distribution is angularly dependent. In this report, I will concentrate on two specific experiments. In Figure 7, the scattering of a 25 μm Mo foil is shown. The foil was positioned in the $[1\ 1\ 0]$ orientation, and a series of images was obtained. The foil was then rotated 90° and the procedure repeated. These two sets of images were then subtracted. The net result is two sets of three bright spots (left and right of the center), and similar sets of dark spots (above and below the center). These are characteristic of the scatter from the $[1\ 1\ 0]$ plane of Mo. These data were used to calibrate the image in terms of scattering angle, and also demonstrated that scattering could be observed.

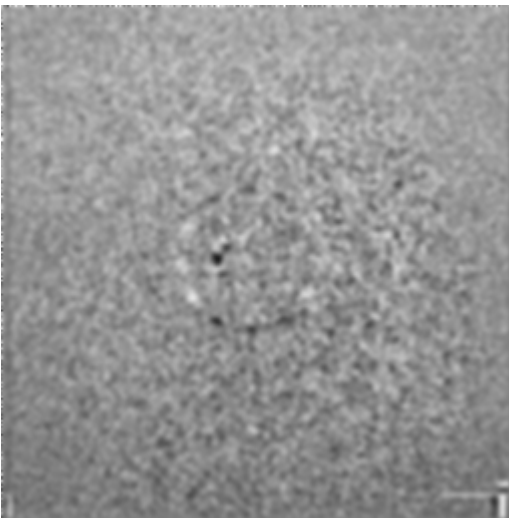


Figure 7: A single $k\alpha$ line was selected to irradiate 25 μm Mo foil. Shown is the difference of the scattered pattern when the foil is rotated 90 degrees. (see text for further details). The image is noisy due to limitations on x-ray exposure; to reduce the impact of the noise, the image has been smoothed.

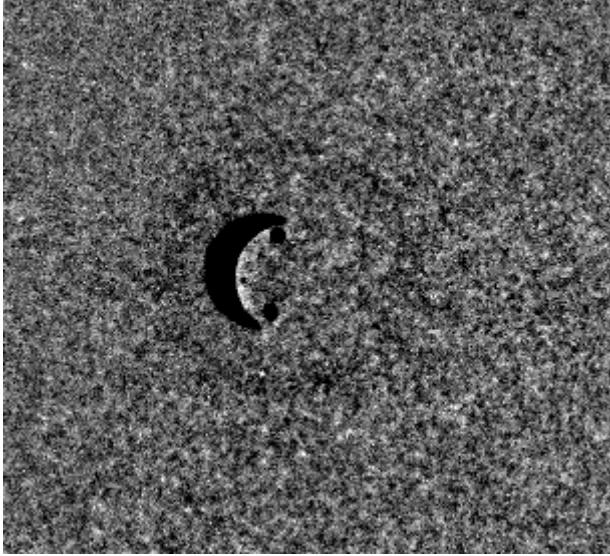


Figure 8: A single $k\alpha$ line was selected to irradiate a thin layer of wax. Shown is the beam scattered at an angle of approximately 10 degrees. (The crescent shape is an artifact). The image is quite noisy in spite of the fact that this image represents the average of 40 exposures.

We next attempted to test the dependence of the scattering of several test materials. We were only able to evaluate those materials which we previously knew to be highly scattering. For example a sample polarization scatter image is shown in Figure 8. This image is the scatter pattern of a thin layer of wax. The image represents the average of 40 individual exposures of 40 kV, 100 mAs each. The image is quite noisy, and the scattered radiation is barely visible. We were not able to determine whether there was an angular dependence to the scattering due to the low fluence.

4.3. Summary of Polarimeter Development

The first polarimeter design has the advantage that the irradiating beam is broad-spectrum and of high fluence. The scatter from the analyzer crystal must be measured at right angles, and will be dependent upon the polarization of the incident beam. Unfortunately, the polarized portion of the beam is small ($P_{pol} = 0.05 - 0.10$), thus the variation in the scatter is equally small. The scatter distribution must be fitted to a sinusoidal function, and the phase of the sinusoid determine. We calculated that we could achieve an angular resolution of about 3 degrees, based on the incident and scattered fluence. Evaluation of a number of materials failed to show rotation of the polarization vector. The poor angular resolution may have been at least partly responsible. An evaluation of quartz (a material known to have high optical activity) failed to show rotation due to the high absorption of the quartz. This limitation led us to consider the second polarimeter design.

The second polarimeter design has the advantage that rather than attempting to measure changes in polarization with a signal of $\sim 10\%$, the polarization signal has 100% amplitude. However, there are two problems with this second technique. First, only a small fraction of the incident x-rays are so reflected by the crystal, thus the signal recorded is very weak. Secondly, the x-rays scattered by the sample need to be scattered at close to 90° to show 100% polarization. This further reduces the number of scatter events that can be successfully recorded.

In the end, we were forced to conclude that polarization imaging is unlikely to succeed. First, it is highly unlikely that x-ray polarization will be capable of being measured with a diagnostic x-ray tube. The fluence and lack of a single polarization state make this nearly

impossible. A synchrotron light source would alleviate this problem, as synchrotrons produce x-rays in a single polarization. Secondly, the high fluence needed to measure polarization would result in an excessively high radiation dose and hence is not practical.

4.4. X-ray Spectra Modeling

Fortunately, certain positive findings can be reported. The polarization modeling required that we model the x-ray spectrum in order to simulate our experimental conditions. In particular, we needed these data to determine the fluence rates in the two polarimeter designs. For spectra below 40 kV, we used the Boone model [Boone97]. However, we simulated x-ray spectra in the range of 40 to 49 kV by extrapolating Boone's model. Boone parameterized spectra measured at the FDA for Mo, Rh and W target x-ray tubes operated between 18 and 40 kV. Each energy bin in the spectra was fitted in terms of the photon fluence as a function of kV using first, second order or third order polynomials. We believe that these data are over-fitted. This will become evident when we consider how to extrapolate the data.

In this report, we will concentrate on the extrapolation of the Rh target spectra. The extrapolation was split in two parts. Below 24 keV we used the parameters from Boone's paper for the extrapolated kVs. Above 24 keV, which we will refer to as the tails of the spectra, we refitted the spectra. In performing our fits, we assumed that: 1) for a given kV the photon fluence in the tails are linear with keV; 2) the slopes of the linear fits of the tails decrease with increasing kV; and 3) the photon fluence is zero at the maximum energy of each spectrum.

In Figure 9 we show spectra between 26 and 49 kV using Boone's parameters. Note that the shapes of the extrapolated spectra (grey) are similar to the published ones (black). Figure 9-b shows the low energy part in detail. The fluctuations in the extrapolated data are clearly artifactual. We have not addressed these artifacts as this low energy range is typically filtered from the beam. Next, consider the characteristic radiation peaks. Theoretically, for a thin target, the ratio of the K_{α} to K_{β} peak is constant; for a Rh target this ratio is 5.46. The target of an x-ray tube is not thin, but to a first approximation we can consider it as thin because the electrons incident on the anode are much less penetrating than the fluorescent x-rays. Figure 10 shows that K_{α}/K_{β} decreases starting at 38 kV. This decrease may be due to erroneous fitting. However, it could also be explained by beam hardening in the thick Rh target. This would be consistent with our data, as beam hardening would cause the fraction of K_{β} to increase. Figure 9-c is a detail of the tails. Again one can see the effect of over-fitting. We could have kept the tails as they are and extrapolated them beyond 40 keV. However, as this energy range is of significance in our experiments, we chose to refit them. Using the assumptions stated above, we calculated the slopes of the tails for the spectra from 34 to 40 kV. The slopes were calculated from 26.5 keV using linear interpolation. We applied a least squares fit and used this fit to estimate the slopes of the tails of the extrapolated spectra. Figure 9-c shows our fits. In analogy with Boone's model, the photon fluence were fitted as function of kV for each energy bin. We applied first, second and third order fits. We chose the simplest fit for each energy bin. The residuals between the fits and the data were 2 orders of magnitude smaller than the actual data.

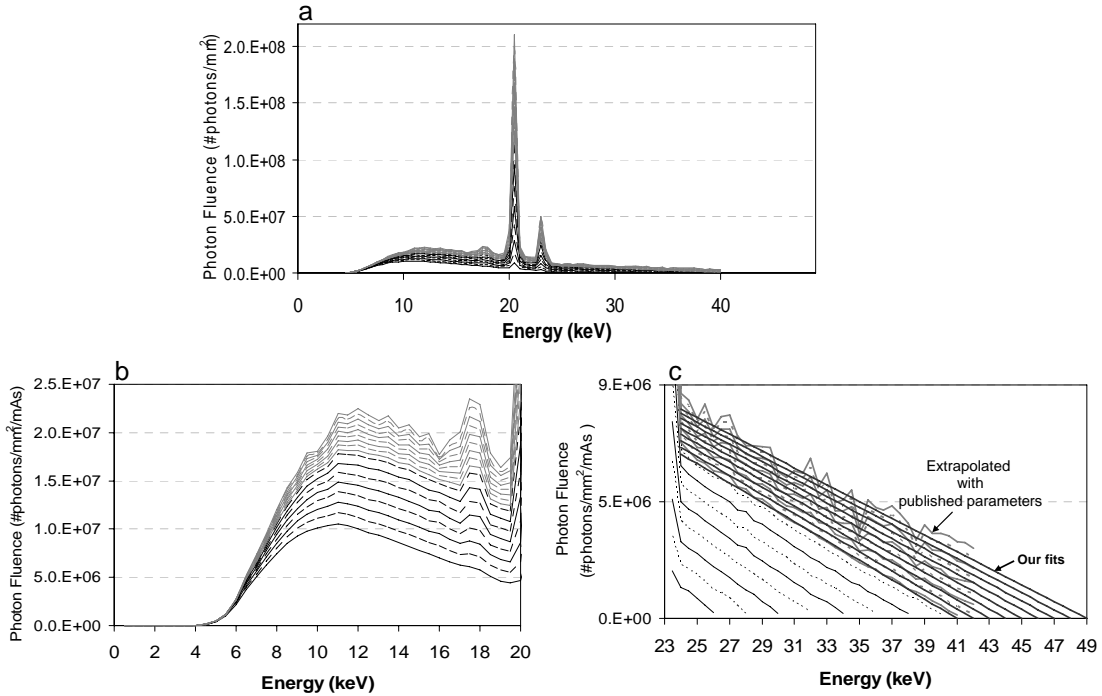


Figure 9: a) X-ray spectra from 26 kV to 49 kV using Boone’s parameters. Note that the extrapolated spectra (grey) have the same shape as the published spectra by Boone (black). b) Detail of the low-energy region of the spectra shown in a). Note that the fluctuations in the extrapolated spectra are artifactual. c) Detail of the tails of the spectra shown in a). These fluctuations are also artifactual.

We validated our simulations using a least-squares comparison (i.e., minimizing the χ^2 values) between measured and simulated attenuation data. We used Al filters (99.997 % pure, Alfa Aesar, Ward Hill, MA) to determine the attenuation curves. The minimum χ^2 was found by adjusting the kV ($kV_{\text{equivalent}}$) and adding extra Al ($Al_{\text{equivalent}}$) to the simulated spectra. We also compared the half value layers (HVL), quarter value layers (QVL), eight value layers (EVL) and tenth value layers (TVL) of the measurements and the simulations. The measurements were performed with a Senographe 2000D (GE Medical Systems, Milwaukee, WI). The Senographe 2000D was operated with a Rh target and 0.25 mm Rh or 0.27 mm Cu filtration. We used the Cu filter to emphasize the tails. The tube has a 0.69 mm thick Be window; a 2 mm thick compression paddle was in the x-ray beam; the distance from the target to the exposure meter was 43 cm.

We modeled this system by filtering our fitted Rh spectra with added filtration simulated to match the experimental setup. Tables 1 and 2 demonstrate that the extrapolation of Boone’s spectral models agree well with our measurements. Shown are the equivalent kV ($kV_{\text{equivalent}}$) and equivalent Al filtration ($Al_{\text{equivalent}}$) of the simulated spectra for a nominal kV that results in the smallest χ^2 . HVL and QVL are also presented for Rh and Cu filters; EVL and TVL are only presented for the Rh filter. The largest difference between the measured and simulated HVL, QVL, EVL and TVL is 1.8 % for the QVL at 49 kV with a Rh filter (48 $kV_{\text{equivalent}}$ and 0 mm $Al_{\text{equivalent}}$). Figure 12 show examples of Rh spectra filtered with 0.27 mm Cu. The largest difference between the measured and simulated HVL and QVL is 1.3 % for the QVL at 34 kV (33.5 $kV_{\text{equivalent}}$ and 0 mm $Al_{\text{equivalent}}$). This occurs in the range of energies fitted by Boone. In the extrapolated

range, the largest difference, 0.6 %, was found for the QVL at 49 kV (48.4 kV_{equivalent} and 0 mm Al_{equivalent}).

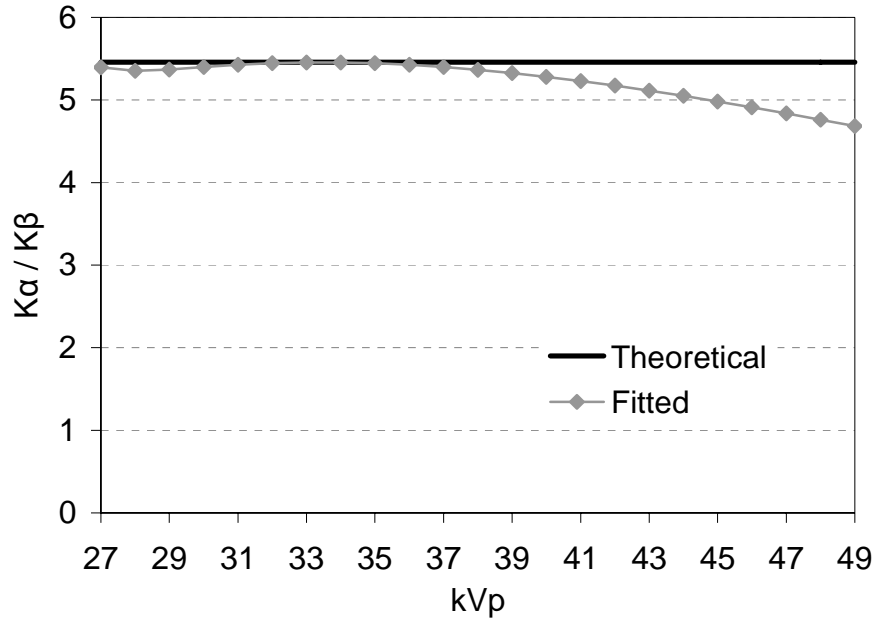


Figure 10: K_{α}/K_{β} for a thin Rh target (theoretical) and as calculated in the fitted spectra. Note that K_{α}/K_{β} decreases from 38 kV.

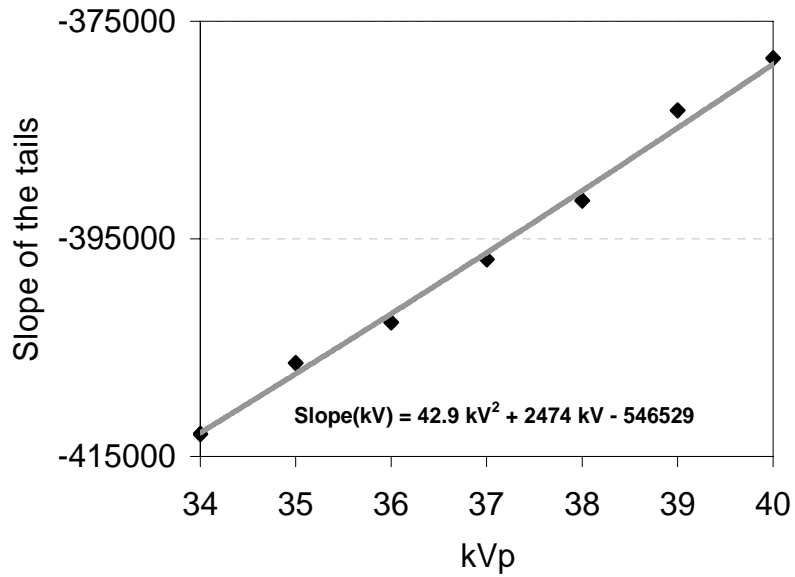


Figure 11: Slopes of the tails for the published spectra from 34 to 40 kV. A least squares fit was used to determine the slopes of the tails of the extrapolated spectra.

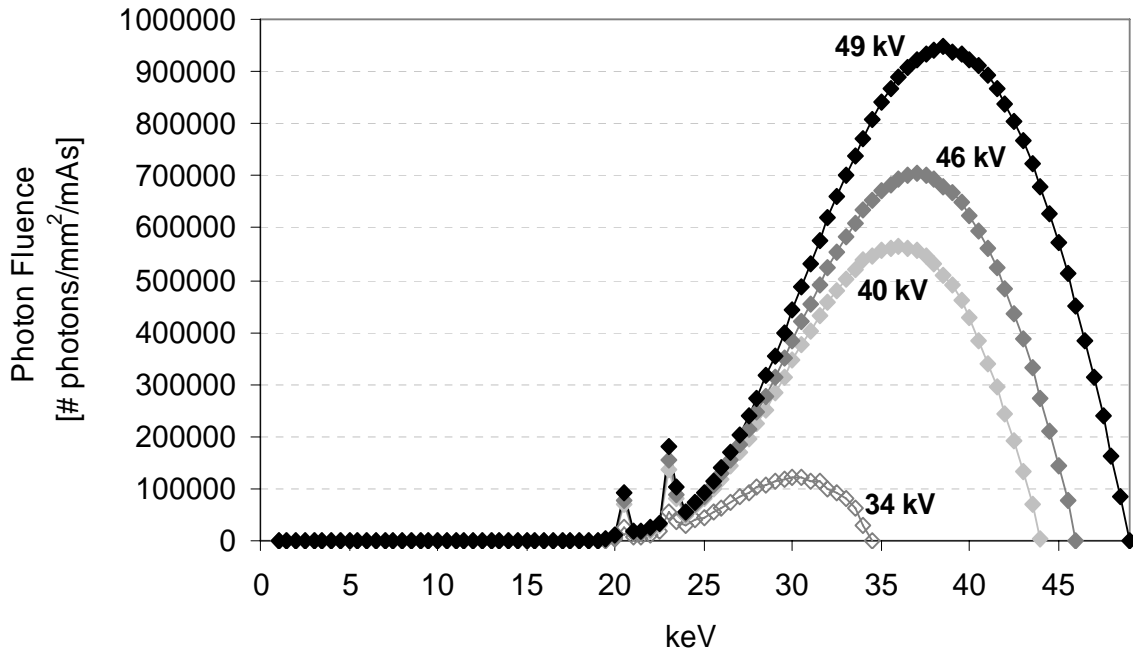


Figure 12: Examples of x-ray spectra from a Rh target filtered with 0.27 mm Cu. The fluence is specified 43 cm from the target.

Table 3 shows data from a GE DMR, acquired with a Mo-target x-ray source and 1 mm Al filtration. The x-ray tube window was composed of 0.69 mm thick Be and a 2 mm compression plate was again in place. Shown are $kV_{\text{equivalent}}$ and $Al_{\text{equivalent}}$ of the simulated spectra for a nominal kV that results in the smallest χ^2 . The measured and simulated estimates of the HVL and QVL are also presented. The simulated values are those that minimize the χ^2 . Again, the results in this table demonstrate that the extrapolation of the Boone’s spectral models agree well with our measurements.

Table 1: Comparison of the measured and simulated attenuation data for a Rh target filtered with 0.25 mm Rh. HVL, QVL, EVL and TVL are expressed in mm Al.

Nominal kV	$kV_{\text{equivalent}}$	$Al_{\text{equivalent}}$	Measured				Simulated				
			HVL	QVL	EVL	TVL	HVL	QVL	EVL	TVL	χ^2
25	25.3	0.000	0.361	0.820	1.382	1.574	0.359	0.822	1.378	1.573	0.0001
28	28.4	0.000	0.412	0.949	1.589	1.818	0.411	0.950	1.593	1.819	0.0001
34	33.5	0.000	0.478	1.116	1.868	2.120	0.482	1.114	1.859	2.118	0.0001
40	39.8	0.000	0.556	1.244	2.088	2.382	0.546	1.258	2.092	2.384	0.0001
46	45.0	0.000	0.578	1.341	2.228	2.575	0.586	1.346	2.243	2.563	0.0005
49	48.0	0.000	0.612	1.365	2.309	2.625	0.605	1.390	2.325	2.662	0.0006

Table 2. Comparison of the measured and simulated attenuation data for a Rh-target tube filtered with 0.27 mm Cu.

Nominal kV	$kV_{\text{equivalent}}$	$Al_{\text{equivalent}}$	Measured		Simulated		χ^2
			HVL	QVL	HVL	QVL	
34	33.5	0.0	1.711	3.532	1.713	3.579	0.00009
40	39.4	0.0	2.232	4.750	2.238	4.738	0.00012
46	45.5	0.0	2.779	5.978	2.787	5.978	0.00005
49	48.4	0.0	3.060	6.619	3.063	6.578	0.00006

Table 3. Comparison of the measured and simulated attenuation data for a Mo-target tube filtered with 1 mm Al.

nominal kV	kV _{equivalent}	Al _{equivalent}	Measured		Simulated		χ^2
			HVL	QVL	HVL	QVL	
22	21.1	0.075	0.388	1.285	0.385	1.286	0.00007
28	28.0	0.100	0.538	1.844	0.540	1.841	0.00005
34	35.0	0.050	0.607	2.050	0.609	2.197	0.00009
40	39.4	0.100	0.654	2.420	0.649	2.442	0.00070
46	45.4	0.150	0.698	2.734	0.686	2.736	0.00071
49	49.0	0.175	0.739	2.907	0.703	2.911	0.00422

We originally had planned on publishing these extrapolated data in the peer-reviewed literature. These data have been widely used since we first published them 2 years ago. However, based upon our these results, we were approached by the FDA (Kyle Myers, Private Communication) to assist them in fitting newly measured spectra that cover the range to 50 kV. This work is described in detail in the next section

4.5. X-ray spectral fitting

4.5.1 Data

Mo, Rh, and W-target spectra between 20 *kVp* and 50 *kVp* were measured at the Center for Devices in Radiological Health (US FDA, Rockville, MD). Spectra were measured in two *kVp* intervals. The measured photon fluence were binned into 0.5 keV intervals. Figure 13 shows the measured photon fluence of the Rh spectra as a function of *keV* and *kVp*.

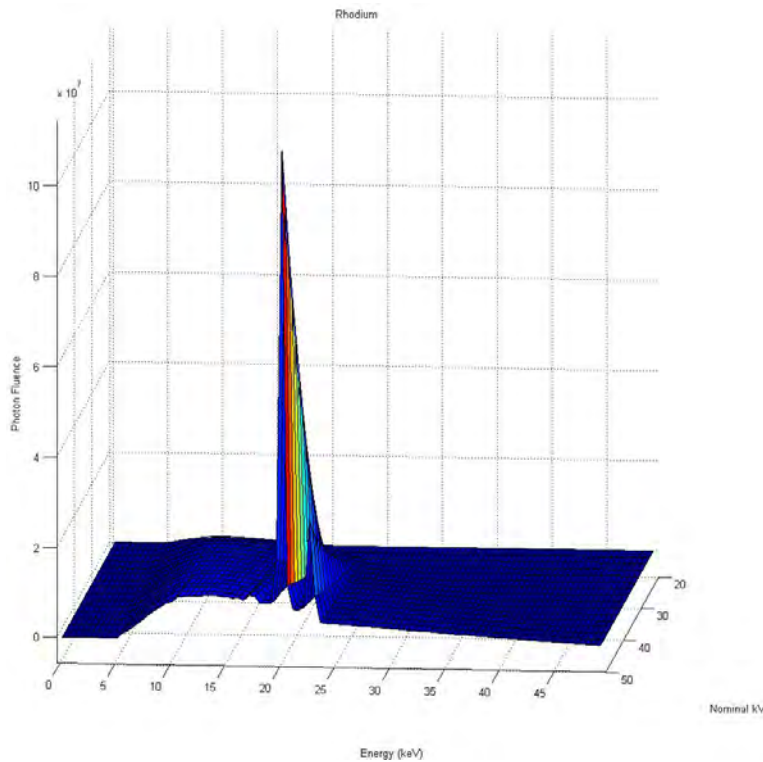


Figure 13: Measured Rh spectra as a function of *keV* and *kVp*.

4.5.2 Fitting energies up to 16.2 keV

For each experimentally obtained spectrum, the photon fluence in each energy bin was fitted versus keV using a least square fit:

$$photon\ fluence(kVp, keV) = A_{kVp_i} (keV - B_{kVp_i})(keV - C_{kVp_i})^2$$

where A_{kVp_i} , B_{kVp_i} and C_{kVp_i} are fit parameters for each kVp_i , with $i = 26$ to 50 kVp .

Next, A_{kVp_i} , B_{kVp_i} and C_{kVp_i} were fit versus kVp :

$$A_{kVp_i} = U_1 \cdot kVp_i^3 + U_2 \cdot kVp_i^2 + U_3 \cdot kVp_i + U_4$$

$$B_{kVp_i} = U_5 \cdot kVp_i + U_6$$

$$C_{kVp_i} = U_7 \cdot kVp_i^3 + U_8 \cdot kVp_i^2 + U_9 \cdot kVp_i + U_{10}$$

Figure 14 shows the values of A_{kVp_i} , B_{kVp_i} and C_{kVp_i} as a function of kVp and their fits. This figure shows that B_{kVp_i} and C_{kVp_i} can be satisfactorily fit using a second and third order polynomial, A_{kVp_i} varies “in steps” with kVp . Therefore, we modified our fit using:

$$photon\ fluence(kVp, keV) = A'_{kVp_i} (keV - B'_{kVp_i}) \left(1 - \frac{keV - B'_{kVp_i}}{C'_{kVp_i}}\right)^2$$

The transformations from the original fit to this new fit are:

$$A'_{kVp_i} = A_{kVp_i} \cdot (B_{kVp_i} - C_{kVp_i})^2$$

$$B'_{kVp_i} = B_{kVp_i}$$

$$C'_{kVp_i} = C_{kVp_i} - B_{kVp_i}$$

A'_{kVp_i} , B'_{kVp_i} and C'_{kVp_i} vary smoothly with kVp (Figure 15). Figure 16a shows a surface fit through the low energy part of the spectra using the 10 parameters that were derived above. Figure 16b is a profile through the 3D fit (photon fluence versus keV at 30 kVp); this figure shows that the experimental photon fluence data and the fit match well. The fit and the experimental spectra differed up to 7%.

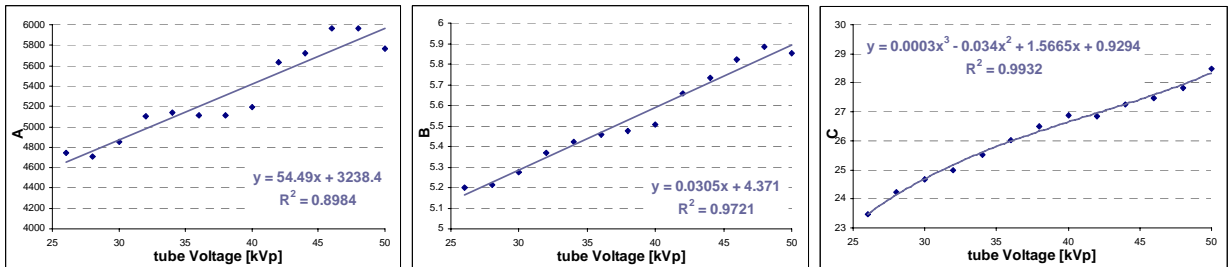


Figure 14: A_{kVp_i} , B_{kVp_i} and C_{kVp_i} values versus kVp (solid diamonds) and their fits (solid lines) as a function of kVp .

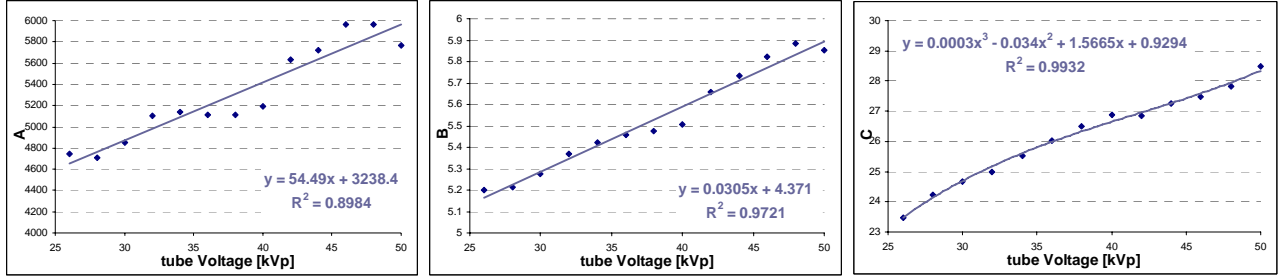


Figure 15: Modified fit parameters A'_{kVp_i} , B'_{kVp_i} and C'_{kVp_i} (solid diamonds) and their fits (solid lines) as a function of kVp.

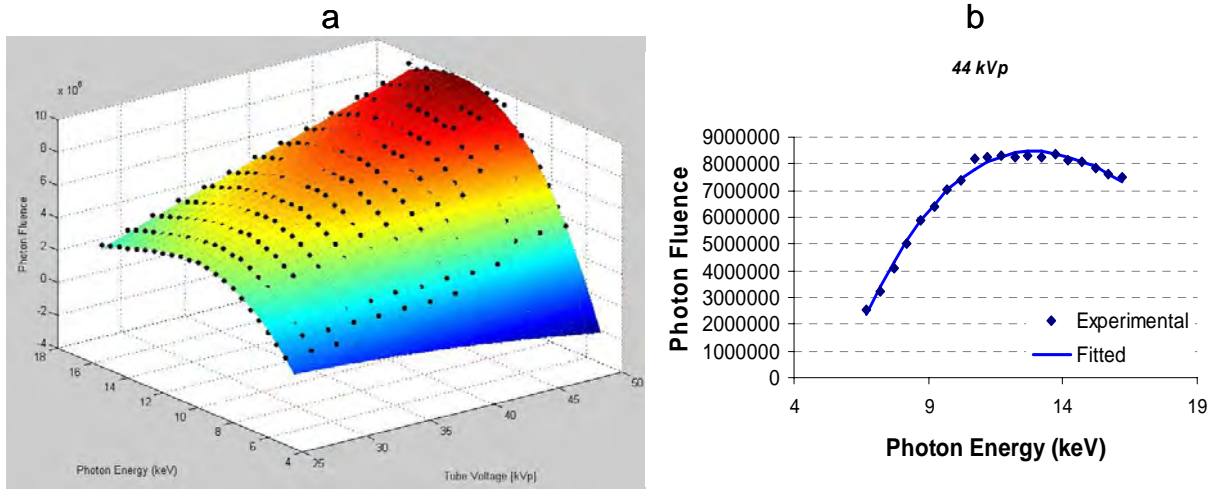


Figure 16: a. Photon fluence as a function of kVp and keV . The solid circles are experimentally obtained photon fluences, the surface plot is the fit using the 10 parameter model. b. is a profile through a. It shows the measured photon fluence (solid diamonds) and the fitted photon fluence (solid line) as a function of keV at 44 kVp .

4.5.3 Fitting energies from 23.7 keV to kVp

In performing our fits in this energy regime, we assumed that: 1) for a given kVp the photon fluence in the tails are linear with keV ; 2) the slopes of the linear fits of the tails decrease with increasing kVp ; and 3) the photon fluence is zero at the maximum energy of each spectrum. Figure 17a shows the high energy part of the experimental spectra as a function of keV for tube voltages between 26 kVp and 48 kVp . This photon fluence as a function of keV was fit using first order polynomials (Figure 17a). Note that the slopes decreases as a function of kVp . Figure 17b shows the slopes from the linear fits as a function of kVp . The slopes as a function of kVp were fit using a third order polynomial. The 3D photon fluence; *i.e.* as a function of keV and kVp ; was plot as:

$$photon\ fluence(kVp, keV) = slope(kVp_i) \cdot (keV - keV_{0_i})$$

where keV_{0_i} is the keV where the photon fluence equals zero; in other words it equals kVp_i . Figure 18 shows a surface fit through the high energy part of the spectra using the parametric fit that was derived above.

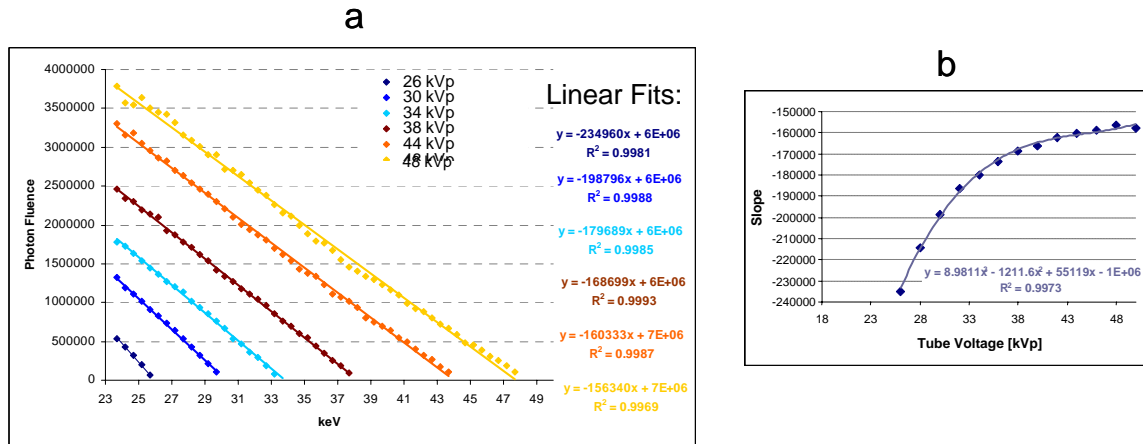


Figure 17: a. High energy part of the experimental spectra (solid diamonds) as a function of *keV* for various *kVps*. The solid lines are linear fits through the experimental data. b. Slopes from the linear fits in a. as a function of *kVp*.

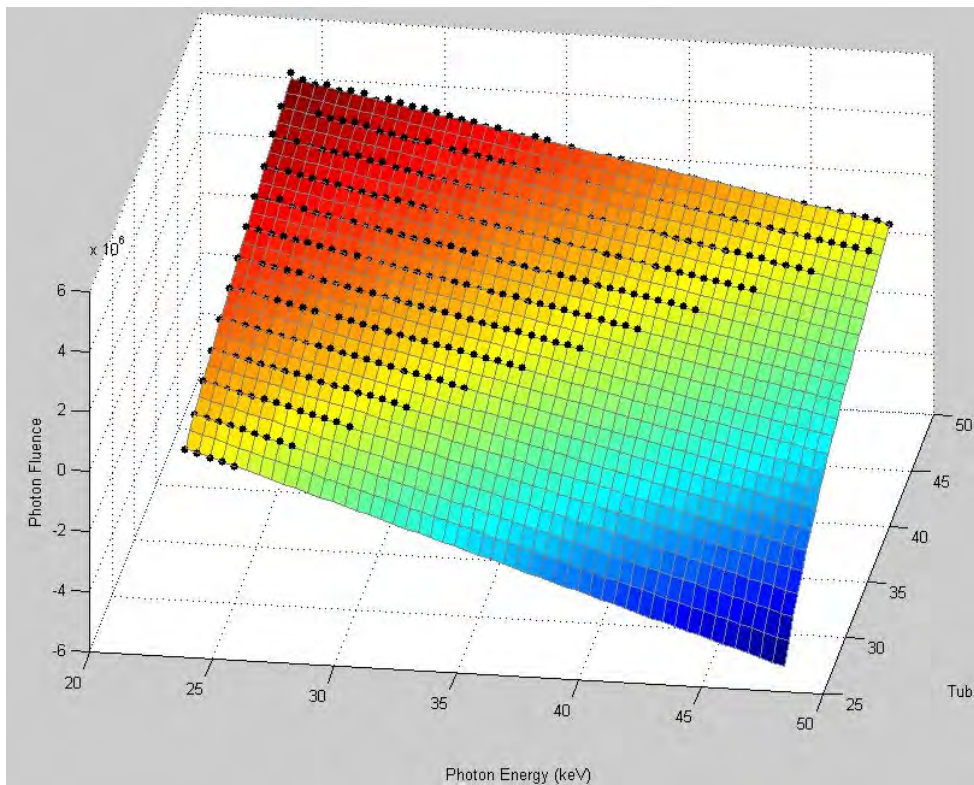


Figure 18: Photon fluence as a function of *kVp* and *keV*. The solid circles are experimentally obtained photon fluences, the surface plot is the fit using the model.

4.5.4 Fitting energies from 16.7 to 23.2 keV

For the mid energy regime, which includes the K-edges, we fitted, for each keV, the photon fluence as a function of kVp. It was impossible to fit this part of the spectra using

a 3D fit. Figure 19 shows some examples. The optimal fits were 1st order polynomials at all keVs except at 19.7 keV, 20.2 keV (K-edge of Rh), and 20.7 keV, 22.7 keV and 23.2 keV (K-edge of Rh) where a 2nd order polynomial fit give the best results.

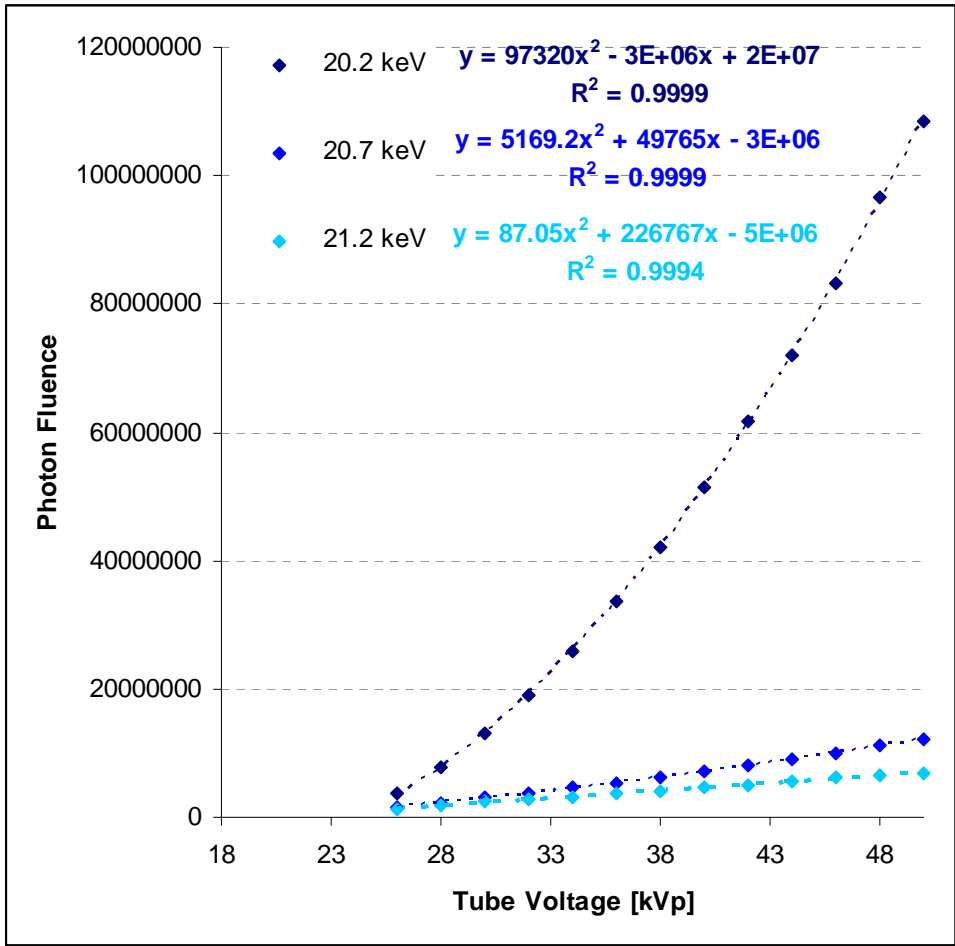


Figure 19: Photon fluence as a function of *kVp* for the energy bins 20.2, 20.7 and 21.2 keV.

4.5.5 Summary

At this time, we are continuing to work with the FDA on fitting these data, with the intention of publishing the data and fits towards the end of 2007. The data fitting has led the investigators at the FDA to question certain aspects of the data corrections applied to the measured spectra (so-called “stripping algorithms”). We are working with the FDA on these analyses and will then subsequently publish these data and the fits to the data.

It is important to understand the relevance of these results. Prior to our analysis, the most widely used spectral model for breast imaging was that of Boone [Boone97]. Those data were severely overfit; a total of 84 fitting parameters were used. By carefully choosing a spectral model and fitting methodology, we have reduced this to a total of 17 parameters. We expect these data to become the industry standard for modeling mammography spectra when published.

4.6. Mechanisms for Contrast in Radiography

As stated above, the difficulties encountered in our quest to develop polarization radiography has led us to think more broadly about the mechanisms for contrast in radiography. Attached (Appendix 1) is a book chapter that discusses the concepts of intrinsic and extrinsic contrast in breast imaging. These have led us to develop a number of methods for enhancing the intrinsic contrast of breast lesions. In particular, we have pioneered the concept of contrast-enhanced breast tomosynthesis [Chen07], and have since obtained a DOD concept award to evaluate the potential of gold nanoparticle-based contrast agents. We have also actively espoused this taxonomy as a valuable pedagogical tool.

Key Research Accomplishments:

The following is a brief summary of key research accomplishments arising from this grant:

- A broad spectrum x-ray polarimeter was constructed and tested. The device was found to lack sufficient angular precision to measure optical activity at diagnostic x-ray energies.
- A near-monoenergetic x-ray polarimeter was constructed and tested. A monoenergetic beam of x-rays was produced by using a crystal spectrometer, elemental beam filtration and selective windowing of the resulting spectrum. The resulting device lacked sufficient photon fluence to observe optical activity at diagnostic x-ray energies
- Based on these experiments, we have come to conclude the imaging of breast tissue based upon the optical activity or birefringence in the diagnostic x-ray range is not practical
- Based on these experiments, we have come to conclude that polarization measurements (e.g., optical activity or birefringence) requires an intense linearly or circularly polarized x-ray source, such as a synchrotron.
- To complete the modeling of our polarimeter designs, we developed a validated extrapolation of Boone's spectral models. This extrapolation was presented at the SPIE Medical Imaging Conference in 2006, and has become widely cited and used. The model has application in a number of fields including contrast-enhanced mammography and tomosynthesis.
- Based on these results, we have formed a collaboration with the FDA to fit new x-ray spectral data. Our preliminary fit is described, and we are currently working with the FDA to complete this work for publication this year.
- Based on this effort, we have developed a new pedagogical approach to considering the intrinsic and extrinsic contrast achievable with breast radiography. We have used to approach to consider new methods of imaging the breast.

Reportable Outcomes:

Research Paper, Peer-Reviewed

None

Research Papers, Non-peer Reviewed

1. Maidment ADA and Albert M. "Tissue Discrimination Methods in Mammography". In: Advances in Digital Radiography: RSNA Categorical Course in Diagnostic Radiology Physics 2003. Radiological Society of North America, Oak Brook, IL, 2003. (and CD-ROM)
2. Carton, AK, Li J, Albert M, Chen S, and Maidment ADA. "Quantification for Contrast Enhanced Digital Breast Tomosynthesis," Physics of Medical Imaging: Proc. SPIE 6142, edited by E.L. Siegel, E.A. Krupinski, and M. Sonka (2006).
3. Carton AK, Li J, Chen S, Conant EF, and Maidment ADA. "Optimization of Contrast-Enhanced Digital Breast Tomosynthesis". In "Digital Mammography: 8th International Workshop, IWDM 2006", edited by SM Astley, M Brady, C Rose and R Zwigelaar. LNCS 4046, Springer-Verlag, Berlin (2006), pp183-189.

Abstracts:

1. Boone JM, Carson P, Cherry S, Giger ME, Hendrick RE, Lewin J, Maidment ADA, and Niklason LT. "New Advances in Breast Imaging", Medical Physics, **30**(6), 1391 (2003).
2. Maidment ADA. "Tissue Discrimination Methods in Mammography" (abstr.), In: Radiological Society of North America scientific assembly and annual meeting program. Oak Brook, IL, 35-6 (2003).
3. Maidment ADA. "Tissue Discrimination Methods in Mammography" (abstr.), In: Radiological Society of North America scientific assembly and annual meeting program. Oak Brook, IL, 123 (2004).
4. Maidment ADA, Albert M, and Kao Y-H. X-ray Polarization Imaging. Proceedings, "Era of Hope", DOD Breast Cancer Research Meeting. p. 290. (2005).
5. Maidment ADA. "Tissue Discrimination Methods in Mammography" (abstr.), In: Radiological Society of North America scientific assembly and annual meeting program. Oak Brook, IL, (2005).
6. Carton AK, Chen SC, Albert M, Conant EF, Schnall MD, and Maidment ADA. Technical Development of contrast-enhanced Digital Breast Tomosynthesis. (abstr.), In: Radiological Society of North America scientific assembly and annual meeting program. Oak Brook, IL, (2005).

Invited Lectures:

1. Boone JM, Carson P, Cherry S, Giger ME, Hendrick RE, Lewin J, Maidment ADA, and Niklason ET. "New Advances in Breast Imaging", 45th Annual Meeting of the American Association of Physicists in Medicine, San Diego, CA, August 12, 2003.
2. Maidment ADA. "Tissue Discrimination Methods in Mammography". 89th Scientific Assembly of the Radiological Society of North America, Chicago, IL, Dec. 4, 2003.
3. Maidment ADA. "Looking towards the Future of Mammographic Imaging". Royal Marsden Hospital, London, England, April 5, 2004.
4. Maidment ADA. "Looking towards the Future of Mammographic Imaging". General Electric Medical Systems, Buc, France, April 26, 2004.
5. Maidment ADA. "Tissue Discrimination Methods in Mammography". 90th Scientific Assembly of the Radiological Society of North America, Chicago, IL, Dec. 2, 2004.
6. Maidment ADA. "Thoughts on the Future of Radiology", Grand Rounds, University of California San Diego, Department of Radiology, San Diego, CA, February 15, 2005.
7. Maidment ADA. "Tissue Discrimination Methods in Mammography". 91st Scientific Assembly of the Radiological Society of North America, Chicago, IL, Nov. 27, 2005.

Proffered Presentations and Posters:

1. Maidment ADA, Albert M, and Kao Y-H. X-ray Polarization Imaging. "Era of Hope", DOD Breast Cancer Research Meeting. Philadelphia, PA, June 8-11, 2005.
2. Carton AK, Chen SC, Albert M, Conant EF, Schnall MD, and Maidment ADA. Technical Development of contrast-enhanced Digital Breast Tomosynthesis. 91st Scientific Assembly of the Radiological Society of North America, Chicago, IL, December 2, 2005.
3. Carton, AK, Li J, Albert M, Chen S, and Maidment ADA. "Quantification for Contrast Enhanced Digital Breast Tomosynthesis," SPIE Medical Imaging 2005 (Physics of Medical Imaging) San Diego, California, February 12, 2006.
4. Carton AK, Li J, Chen S, Conant EF, and Maidment ADA. "Optimization of Contrast-Enhanced Digital Breast Tomosynthesis". 8th International Workshop, IWDM 2006", Manchester, UK, June 19, 2006.

Conclusions:

In this grant, we hypothesized that the polarization of x-rays passing through tissue might be altered in a detectable manner. We proposed to build an x-ray polarimeter and determine the factors that affect its design. In the end, we built and tested two polarimeters; both designs functioned to the extent that they could be used to measure the polarization of the incident x-ray beam. However, neither design was capable of measuring polarization changes from any material. Our original design lacked the angular precision needed for the measurement. Our second design lacked adequate photon fluence. This work did, however, contribute to our knowledge of (1) the polarization of x-ray tubes; (2) modeling the spectra of x-ray tubes; (3) methods for producing near mono-energetic x-ray spectra for breast imaging; (4) the mechanisms of contrast in radiography (especially of the breast); and (5) the mechanisms of polarization at x-ray energies. This work has led to new innovations in developing imaging contrast agents. In addition, some potential avenues for future research of polarization radiography have come to light; however, it is likely that x-ray polarization research is best done with a synchrotron light source.

This research, while quite fundamental in its nature, had the potential for a significant impact in breast cancer diagnosis. The use of effects related to the polarization of x-rays largely remains an unexplored field. However, based on our research, the use of polarization imaging is not likely to be clinically realizable.

References:

- [Agar79] B.K. Agarwal, X-Ray Spectroscopy, Springer-Verlag (1979).
- [Barkla05] Barkla, C.G., Phil. Trans. Roy. Soc., **204**, 467 (1905).
- [Barut80] Barut, A.O., Electrodynamics and classical theory of fields and particles, Dover (1980).
- [Boone97] Boone, J.M., Fewell T.R., and Jennings R.J., Molybdenum, rhodium, and tungsten anode spectral models using interpolating polynomials with application to mammography. Medical Physics, 1997. **24**(12), 1863-74.
- [Chen07] Chen, S.C., Carton, A.K., Albert, M., Conant, E.F., Schnall, M.D., Maidment, A.D.A. Initial clinical experience with contrast-enhanced digital breast tomosynthesis. Acad Radiol. (2007), **14**(2), 229-38.
- [Creagh99] Creagh, D.C., The atomic form factor and the X-ray dispersion corrections as tensor quantities: comparisons between theory and experiment. Rad. Phys. Chem. (1999), **56**, 61-83.
- [Dyson90] Dyson, N.A., X-Rays in atomic and nuclear physics, 2nd ed., Cambridge University Press (1990).
- [Hart81] Hart M. and Rodrigues, A.R.D., Phil. Mag. (1981), **B43**, 321.
- [Itzak80] Itzykson, C. and Zuber, J.-B., Quantum Field Theory, McGraw-Hill (1980).
- [Jackson99] Jackson, J.D., Classical Electrodynamics, Wiley (1999).
- [Johns83] Johns, H.E. and Cunningham, J.R., The Physics of Radiology, Thomas (1983).
- [Kuck73] Kuckuck, R.W. and Ebert, P.J., "Linear Polarization of Low-Energy-Electron Bremsstrahlung", Phys. Rev. A (1973), **7**, 456-462.
- [Rohr65] Rohrlich, F., Classical charged particles, Addison-Wesley (1965).
- [Schwing98] Schwinger, J., L.L. DeRaad, Jr., K.A. Milton, and W. Tsai, Classical Electrodynamics, Perseus Books, Reading, Massachusetts (1998).
- [Slivin71] Slivinsky, V. W., Am. Phys. Soc. Bull. (1971), **16**, 546 (Abstract).
- [Staun78] Staun., J. et. al., "Influence of Polarization of the Incident Beam on Integrated Intensities in X-ray Energy-Dispersive Diffractometry", Acta. Cryst. (1978), **A34**, 84-87.

[Steve57] S. Town Stephenson, "The Continuous X-Ray Spectrum", in Encyclopedia of Physics, S. Flügge, ed., Vol. XXX X-Rays, Springer-Verlag (1957).

Appendices:

1. Maidment ADA and Albert M. "Tissue Discrimination Methods in Mammography". In: *Advances in Digital Radiography: RSNA Categorical Course in Diagnostic Radiology Physics 2003*. Radiological Society of North America, Oak Brook, IL, 2003. (and CD-ROM)
2. Carton, AK, Li J, Albert M, Chen S, and Maidment ADA. "Quantification for Contrast Enhanced Digital Breast Tomosynthesis," *Physics of Medical Imaging: Proc. SPIE 6142*, edited by E.L. Siegel, E.A. Krupinski, and M. Sonka (2006).
3. Carton AK, Li J, Chen S, Conant EF, and Maidment ADA. "Optimization of Contrast-Enhanced Digital Breast Tomosynthesis". In "Digital Mammography: 8th International Workshop, IWDM 2006", edited by SM Astley, M Brady, C Rose and R Zwigelaar. LNCS 4046, Springer-Verlag, Berlin (2006), pp183-189.
4. Maidment ADA, Albert M, and Kao Y-H. *X-ray Polarization Imaging. Proceedings, "Era of Hope", DOD Breast Cancer Research Meeting. p. 290. (2005).*
5. Maidment ADA, Albert M, and Kao Y-H. *X-ray Polarization Imaging. "Era of Hope", DOD Breast Cancer Research Meeting. Philadelphia, PA, June 8-11, 2005.*

Tissue Discrimination Methods in Mammography¹

The new generation of digital x-ray mammography systems is capable of using x rays more efficiently than screen-film systems, which will result in some combination of increased image quality and decreased dose to the patient. In addition, this increase in detector efficiency, along with the availability of the data in a digital format convenient for further processing, holds the promise of new techniques that would otherwise be either impossible or extremely awkward to implement. These techniques include dual-energy mammography, digital subtraction mammography, and even more exotic possibilities, such as phase-contrast imaging. This chapter reviews the fundamentals of these approaches and presents some new and preliminary work in these fields. The advantages and disadvantages of these methods are described, and some further areas of investigation are proposed.

INTRINSIC SOURCES OF CONTRAST

Conventional screen-film mammography depends on the intrinsic x-ray attenuation properties of the breast tissue to provide contrast. X rays generated at the focal spot of the x-ray tube pass through the breast. Various regions of the breast remove x rays from the incident beam, either by absorption or scattering, to a greater or lesser extent. Digital mammography devices, like screen-film systems, record the x-ray flux that has been transmitted by the breast, producing an image that can be interpreted as the shadows of objects that removed x rays from the primary beam. By recording the flux of x rays leaving the breast more efficiently, as quantified by the detective quantum efficiency, digital detectors should provide better discrimination than screen-film systems, given the same dose to the patient.

The degree to which a given material attenuates an incident x-ray beam can be quantified in terms of the linear attenuation coefficient μ which represents the fraction of the incident x rays that will be removed from the incident beam per unit of distance traveled in a given material. Differences in opacity observed on mammograms then correspond to differences in μ between tissues. For example, consider a typical x-ray energy² of 18 keV and the values of linear attenuation as measured by Johns and Yaffe

Advances in Digital Radiography: RSNA Categorical Course in Diagnostic Radiology Physics 2003; pp 189–197.

¹ From the Department of Radiology, Hospital of the University of Pennsylvania, 1 Silverstein, 3400 Spruce St, Philadelphia, PA 19104 (e-mail: maidment@rad.upenn.edu).

² Note that 18 keV is the energy corresponding to individual x rays, as measured in kilo electron volts, and not the potential set on the generator, which typically has a value of between 25 and 40 kVp.



(1). At this energy, fibrous tissue was found to have a linear attenuation of $\mu = 1.028 \text{ cm}^{-1}$, so that for a 0.3-cm layer of fibrous tissue,³

$$(1.028 \text{ cm}^{-1}) (0.3 \text{ cm}) \cong 0.3, \quad (1)$$

and thus a 0.3-cm layer of fibrous tissue will remove approximately 30% of the x rays in the primary beam. If the same anatomic region were instead occupied by a 0.3-cm layer of fatty tissue, then using the measured value of $\mu = 0.558 \text{ cm}^{-1}$, one would calculate

$$(0.558 \text{ cm}^{-1}) (0.3 \text{ cm}) \cong 0.2, \quad (2)$$

and only approximately 20% of the x rays would be removed from the primary beam. Thus, regions of the film or x-ray detector under fatty tissue will receive more x rays than regions under layers of equally thick fibrous tissue. For film, this will mean that regions of the film underneath fatty tissue appear darker. Most digital systems will be configured to display images in the same manner as film by default, although digital images can also be displayed so that regions of the detector receiving a greater x-ray exposure appear brighter (ie, they can be displayed with a polarity opposite to that of film). In either case, the differences in linear attenuation coefficient mean that various regions of the detector receive different exposures, yielding an image that represents the x-ray shadow of the breast tissue. Johns and Yaffe (1) report a linear attenuation coefficient for infiltrating ductal carcinoma of $\mu = 1.085 \text{ cm}^{-1}$, only 5% higher than that for fibrous tissue, which is consistent with the low contrast observed clinically between fibrous and cancerous tissues.

The ability of radiologists to detect and interpret such small differences in opacity is limited by several factors, including limitations in contrast discrimination by the human eye and the intrinsic noise in x-ray images. Digital detectors address both of these issues. The data can be postprocessed (“windowed and leveled”) so that the displayed image appropriately represents the range of x-ray intensities in the acquired data. In addition, screen-film systems record only about one-half of the x rays incident on the cassette (as quantified by the zero-frequency detective quantum efficiency), with a considerable fraction of the incident x rays passing through the screen and film without interacting and thus without being recorded. Hence, these x rays do not contribute to image quality but do contribute to patient exposure. More x rays

would be recorded if screens were made thicker, but this change would introduce an unacceptable degree of blurring. The current generation of digital detectors will allow a much smaller fraction of x rays to go unrecorded; that is, the quantum efficiency is increased, thus allowing better image quality for a given dose and enabling discrimination between tissues that produce smaller variations in recorded density.

DUAL-ENERGY IMAGING

The linear attenuation coefficient μ depends on both the material and the energy of the x rays being used. By combining images at two different choices of peak kilovoltage, it is possible to obtain additional information about the tissues being imaged and to emphasize various aspects of the anatomic structures. Johns and Yaffe (2), building on the work of Alvarez and Macovski (3) and that of Lehmann et al (4), discuss a method for producing a combination image in which contrast between fibroglandular tissue and fat has been suppressed; that is, the resulting image demonstrates no contrast between a layer of fibroglandular tissue and an equally thick layer of fat. The resultant images (5) are thus relatively free from clutter by the parenchymal structure, which increases the conspicuity of other materials, such as calcifications. A discussion of the benefits of dual-energy imaging in chest radiography is presented in the syllabus chapter by Heber MacMahon, MD.

An explanation of how dual-energy techniques work requires only a brief excursion into the underlying physical principles. Additional information is given in the syllabus chapter by James T. Dobbins III, PhD, and Richard J. Warp, MS. Over the diagnostic range, the linear attenuation coefficient of tissue decreases with increasing x-ray energy. For example, in going from 18 to 40 keV, Johns and Yaffe (1) found that the linear attenuation coefficient for fat drops from 0.558 to 0.215 cm^{-1} , or to 39% of the value at 18 keV; and the linear attenuation coefficient of fibrous tissue drops from 1.028 to 0.273 cm^{-1} , or to 27% of the value at 18 keV. To understand how measurements at two energies can be exploited, recall that radiography can be thought of as a measure of the total thickness of material, weighted by the linear attenuation coefficient, between the x-ray focus and each position on the x-ray detector, whether it is film or a digital device. Thus, if an image is acquired with 18-keV x rays, each position on the image would represent the sum,

$$T_{18} = [(0.558 \text{ cm}^{-1})(L_{\text{fat}})] + [(1.028 \text{ cm}^{-1})(L_{\text{fib}})], \quad (3)$$

where L_{fat} is the thickness of fatty tissue above the image point, and L_{fib} is the thickness of fibrous tissue above the image point; for simplicity, we have consid-

³In this chapter, we present a heuristic argument rather than a precise mathematical derivation. As a result, one would more precisely use $1 - \exp[-(1.028 \text{ cm}^{-1})(0.3 \text{ cm})]$, or one would perform such calculations after taking the logarithm of the image data. See the syllabus chapter by Heber MacMahon, MD, for an exact derivation.

ered only these two tissue types. Similarly, for an image acquired with 40-keV x rays, each position in the image would represent a measurement of

$$T_{40} = [(0.215 \text{ cm}^{-1})(L_{\text{fat}})] + [0.273 \text{ cm}^{-1}(L_{\text{fib}})]. \quad (4)$$

By forming a weighted sum of these images with carefully chosen weighting factors, the resultant image can be made to display information that would not have been as obvious in either of the source images. Thus, by subtracting 0.123 times the 18-keV image from the 40-keV image, one obtains

$$\begin{aligned} T_{\text{sub}} &= [(0.215 \text{ cm}^{-1}) - (0.123)(0.558 \text{ cm}^{-1})] \cdot L_{\text{fat}} \\ &+ [(0.273 \text{ cm}^{-1}) - (0.123)(1.028 \text{ cm}^{-1})] \cdot L_{\text{fib}} \\ &= (0.146 \text{ cm}^{-1}) \cdot L_{\text{fat}} + (0.146 \text{ cm}^{-1}) \cdot L_{\text{fib}}. \quad (5) \end{aligned}$$

Note, therefore, that the effective attenuation coefficients of the fat and fibroglandular tissue are the same, and thus there is no contrast between fat and fibroglandular tissue in the subtracted image. Other materials such as calcifications or neoplastic tissue, if present, will generally have linear attenuation coefficients with an energy dependence different from that of fat or fibroglandular tissue. Such materials will thus produce contrast in the subtracted image and are more easily visible because the parenchymal clutter has been removed. Any implementation that uses conventional x-ray sources must, of course, take into account both (a) the fact that a given peak kilovoltage setting produces a range of x-ray energies (expressed in kilo electron volts) and (b) the effect of scatter.

Clinical implementation of this technique requires, among other things, the ability to process image data conveniently, as well as high detector quantum efficiency over a larger range of energies than has been conventionally used in mammography. The current generation of digital detectors addresses both issues, by having a higher quantum efficiency and by generating the data in a convenient digital format, making this a technique ripe for development. The promise of this technique is suggested in a report by Asaga et al (6). They used a computed radiography (CR) system in 42 cases. In 21 of those cases, dual-energy techniques provided more diagnostically useful images than conventional mammography. Benign lesions tended to show relatively less contrast on the subtracted images, while malignant lesions were enhanced. Because of the nature of CR systems, registration of the two images was nontrivial. The current generation of digital radiography systems will not require manual positioning and repositioning of the detector, as is necessary in loading and changing a CR cassette. Thus, digital radiography systems will have

an advantage over previous technologies in the prerequisite image registration, which must be done before subtraction.

Asaga et al (6) reported using a Mo anode at 28 and 40 kVp. The question of optimal technique is open. Johns and Yaffe (2), on the basis of theoretical considerations, have recommended 18 and 65 keV. The actual choice of technique must take into account the imaging device that will be used and the available sources of x rays. A Mo anode x-ray tube with a peak kilovoltage in the mammographic range will produce x rays with energies near 18 keV. However, to get a substantial flux near 65 keV would require a tungsten anode x-ray tube operated at high peak kilovoltage. In either case, one would be working with a broad spectrum of x-ray energies, and appropriate elemental filtration would need to be evaluated. The use of monoenergetic beams has been considered in detail (7), but the requirement for exotic x-ray sources such as synchrotrons places practical limits on such techniques.

VASCULAR CONTRAST ENHANCEMENT METHODS

Solid tumors generally cannot grow beyond a few millimeters without developing a blood supply to provide nutrients to the tumor cells and remove metabolic wastes. In a 1992 review, Folkman (8) discussed the accumulated clinical and laboratory evidence of the essential nature of neovascularization for tumor growth, following on the early work of Folkman et al (9). By using a contrast agent, it should be possible to demonstrate the tumor vasculature and the tumor itself radiographically. This technique is now feasible because of (a) the enhanced quantum efficiency of current digital detectors, which permits subtle changes in contrast to be detected with acceptable doses, and (b) the availability of the images in digital form, so that the differences between precontrast and postcontrast images can be conveniently calculated, as in digital subtraction angiography.

Experience in recent years with gadolinium-based contrast agents in breast magnetic resonance (MR) imaging should provide guidance for the use of vascular contrast agents in breast radiography. Cancerous tumors are found to have increased vascularization (perfusion), and the vessels appear to permit the contrast agent to move more quickly across the vessel wall into the tissue (increased permeability) (10). As a result, the signal from tumors appears enhanced. This enhancement permits depiction of architectural features, such as irregularity of the lesion boundary or spiculations; the importance of this was recently emphasized in a study of how the timing of image acquisition relative to injection affects the discernment of such features (11). Much attention has been paid in the MR imaging literature to the time dependence of the

enhancement of the lesion and the later “washout,” which Leach (12) has reviewed concisely. By acquiring multiple images, the enhancement and washout as a function of time can be quantified. Various attempts have been made to interpret this time dependence in terms of models of movement of the contrast agent across the vessel wall and to find differences between benign and malignant lesions in the time dependence of the enhancement.

The vascularity of breast neoplasms has also been demonstrated with Doppler ultrasound (US), but although such quantities as the peak systolic flow velocity, resistance index, and pulsatility index show increased vascularity of malignant tumors on average, it is unclear whether these differences are diagnostically important (13). The utility of iodinated vascular radiographic contrast material in computed tomography (CT) has also been explored with promising results (14,15).

Temporal Subtraction Angiography

The use of digital x-ray techniques for contrast-enhanced imaging of the breast dates to the mid-1980s. Watt et al (16,17) and Ackerman et al (18) performed digital subtraction angiography of the breast, using an x-ray image intensifier in a conventional angiography system. They were able to demonstrate that benign and malignant lesions could be differentiated according to the strength of enhancement (referred to as “blush”). Subtracted images of benign lesions showed little or no enhancement, while those of malignant lesions showed rapid intense enhancement, followed by gradual washout.

Watt et al (16,17) and Ackerman et al (18) used temporal subtraction to depict the contrast enhancement. This technique, illustrated in Figure 1a, is analogous to the vast majority of digital subtraction angiography performed today. A precontrast mask image is first obtained. The contrast agent is then administered intravenously. This method typically involves slow (4–5 mL/sec) injection of contrast material into the antecubital vein of the contralateral arm. The amount injected is variable, but 60 mL is representative. After injection, additional postcontrast images are obtained. A weighted logarithmic subtraction is performed between each postcontrast image and the precontrast mask. The resultant images will show a perceptible signal only where there has been uptake of the contrast agent.

More recently, Skarpathiotakis et al (19) reported performing temporal subtraction contrast-enhanced digital mammography. A computer model of contrast mammography was developed to determine optimal image acquisition conditions. In addition, both phantom and clinical results were presented. These investigators (19) recommend a spectrum obtained with a Mo target x-ray tube operated at 45–49 kVp, with 0.2–

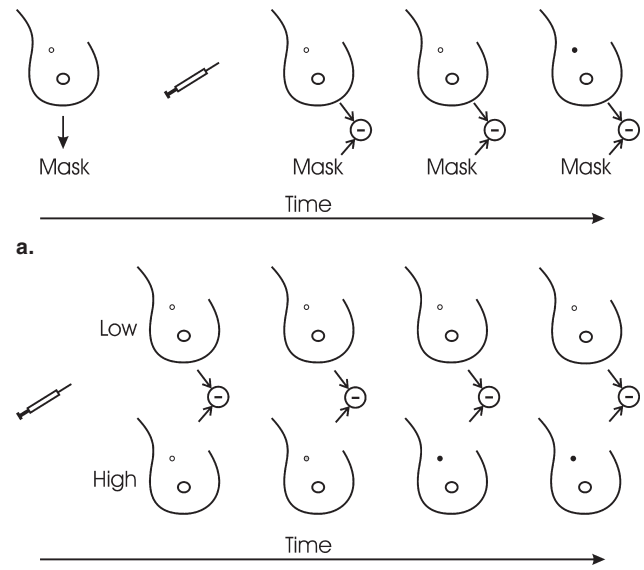


Figure 1. Schematic diagrams illustrating the differences between temporal and dual-energy subtraction contrast-enhanced digital mammography. **(a)** In temporal subtraction, a precontrast image is stored as a mask. After injection, multiple images are acquired at specific intervals and subtracted from the mask image. **(b)** In dual-energy subtraction, after injection of the contrast agent, low- and high-energy images are obtained at specific intervals. A weighted difference of the low- and high-energy images is obtained to produce subtraction images.

0.4-mm Cu filtration. This combination achieves optimum signal-to-noise ratio squared per unit dose (a common metric for optimization), without excessive tube loading or exposure time. Jong et al (20) reported the results for the first clinical examples of this work. One such example is provided in Figure 2.

In a recent report, Diekmann et al (21) described a series of seven patients undergoing digital breast radiography with iodine as a vascular contrast agent. Radiographs were acquired before and at 1, 2, and 3 minutes after patients were injected with 80 mL of the iodine-based contrast agent, iopromide. The radiographs were produced by using a Mo anode with Cu filtration and a potential of 45–48 kVp. This method produces an x-ray beam that is “harder” than that conventionally used in mammography but suitable for detecting the iodinated contrast agent, and the method is similar to what is recommended by Skarpathiotakis et al (19). The precontrast image was then subtracted from each of the postcontrast images. The patients also underwent contrast-enhanced dynamic MR imaging. Diekmann et al (21) reported that the contrast-enhanced mammograms thus obtained showed enhanced features similar to what would be expected on the basis of the corresponding MR imaging examinations.

Technically, temporal subtraction breast angiography has the disadvantage of motion artifacts, which can be only partially addressed with motion correction software and breast compression. As a result, temporal sub-

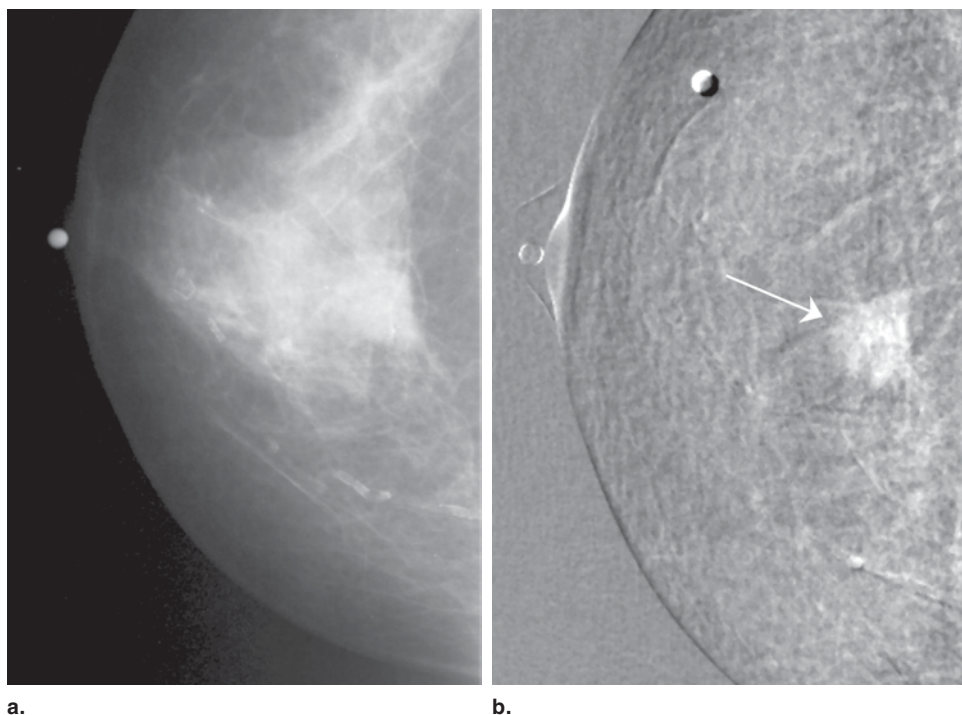


Figure 2. Example of temporal subtraction contrast-enhanced digital mammography. **(a)** Digitized screen-film mammogram, similar to the pre-contrast image. **(b)** Result of subtraction with a postcontrast image obtained 7 minutes after the start of contrast material injection. This subtraction image clearly shows an irregular spiculated enhancement (arrow). The advantages of contrast mammography are clearly illustrated because the anterior margin of the mass is clearly seen in **b**, while it is obscured by fibroglandular tissue in **a**. (Images courtesy of Roberta A. Jong, MD, and Martin J. Yaffe, PhD, University of Toronto, Toronto, Ontario, Canada.)

traction breast angiographic images often exhibit slight residual signals. However, temporal subtraction does provide superior separation of the pre- and postcontrast signals because the spectra can be optimized to distinguish the contrast agent. The use of high-kilovolt-peak beams for both pre- and postcontrast images also helps to minimize the total dose for the study.

Energy Subtraction Angiography

Another approach to implementing breast angiography involves dual-energy imaging, which allows one to perform a weighted subtraction that preferentially suppresses the signal from certain tissue types. Thus, for instance, it is possible to suppress the signals from adipose and glandular tissue preferentially, while enhancing (in a relative sense) the contrast of calcifications or contrast agents.

Figure 1b illustrates the process of dual-energy angiography. A contrast agent is first administered to the patient. The site of injection, injection rate, and the type and amount of contrast agent are similar to those used in temporal subtraction. After injection of the contrast agent, multiple images of the breast are obtained at various intervals after injection. At each time interval, a low-energy (low peak kilovoltage) and a high-energy (high peak kilovoltage) image are obtained in rapid succession. A weighted logarithmic subtraction is then performed between each pair of low- and high-energy images to produce an image with suppressed anatomic information.

Lewin et al (22) have recently reported on the first clinical examples of dual-energy contrast-enhanced digital mammography. A total of 26 patients with mammo-

graphic or clinical findings warranting biopsy were imaged. A single compression was performed in the medio-lateral oblique projection. The low-energy images were obtained either (a) at 30 kVp with a Mo anode material and 0.03 μm of Mo filtration or (b) at 33 kVp with a Rh anode material and 0.025 μm of Rh filtration. The high-energy image was obtained at 44–49 kVp with a Rh anode material and 0.025 μm of Rh filtration. In addition, during the high-energy projection, 8 mm of Al was also added to the beam. The mean interval between low- and high-energy images was approximately 30 seconds. Typically, 100 mL of iohexol was injected.

Lewin et al (22) observed that most of the known cancers were depicted by using subtraction. These investigators also noted that calcifications were depicted, allowing correlation of results. By means of comparison, Lewin et al (22) also performed contrast-enhanced MR imaging. One example is provided in Figure 3, which shows a screen-film mammogram, a contrast-enhanced digital mammogram, and a series of MR images. Results were clearly correlated.

As with temporal subtraction, dual-energy subtraction has certain limitations. Although motion artifacts are suppressed, systems used for performing dual-energy imaging do need to be more extensively modified. First, compared with mammography today, additional or entirely different filtration will be needed for dual-energy contrast-enhanced imaging. Second, the generator must be capable of rapidly switching both the filtration and the radiographic technique used for the low- and high-energy images. Third, the detector will necessarily have to provide rapid image readout, so that the two images can be rapidly sequenced, which not all

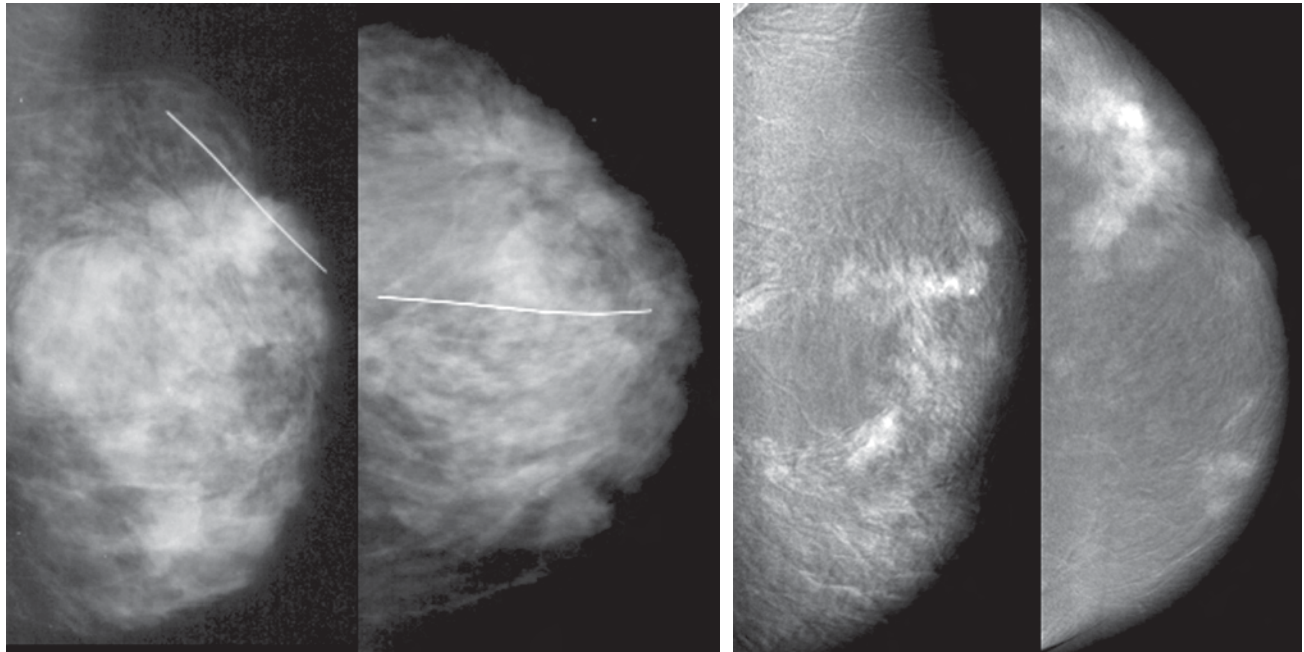
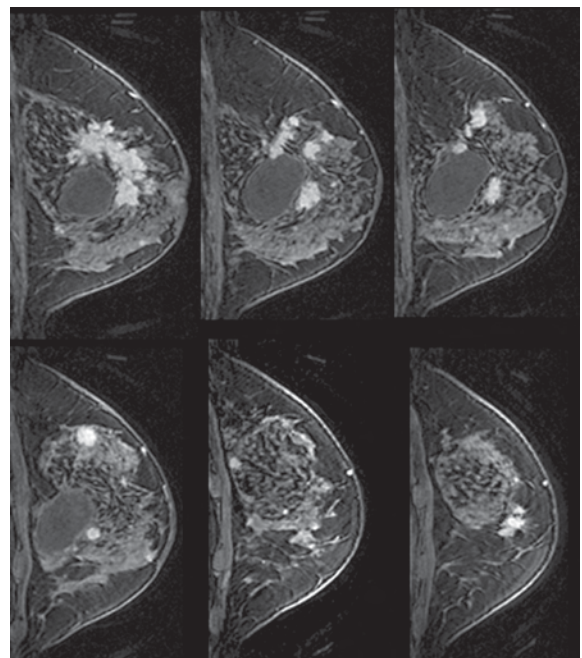


Figure 3. Example of dual-energy contrast-enhanced digital mammography. **(a)** Mediolateral oblique and craniocaudal digitized screen-film mammograms. A cyst and spiculated lesion are marginally visible. **(b)** Result of postcontrast subtraction. This image clearly shows the cyst and multiple regions of contrast enhancement, demonstrating multiple foci of cancer. **(c)** For comparison, a contrast-enhanced MR image of the same breast is shown. Images are arranged laterally to medially. (Images courtesy of John Lewin, MD, University of Colorado Health Science Center, Denver.)

digital mammography implementations can currently do. Finally, dual-energy contrast subtraction will not provide as much signal for the same quantity of contrast agent as temporal subtraction provides because the contrast agent is present in both low- and high-energy images. In the end, however, there is no clear reason to prefer one method over the other, and more research is necessary. Because both methods involve subtraction of images, the noise from random fluctuations in x-ray flux will be emphasized, increasing the relative appearance of x-ray quantum noise.

Future Work

Vascular contrast agents thus show great potential as a diagnostic tool. Among the issues yet to be addressed, two will be mentioned. Breast MR imaging is generally done without much compression, while mammography requires compression to obtain adequate images. It is not clear whether compression affects blood flow enough to change the radiographic appearance. Second, the rate of transport of various contrast agents across the vessel boundary might vary with the nature of the contrast agent. Thus, the radiographic use of vascular contrast agents in breast radiography raises many interesting questions that might be diagnostically important.



c.

GALACTOGRAPHY

Galactography is the imaging of the ductal system with the introduction of a contrast agent and is generally used in the differential diagnosis of abnormal nipple discharge. The contrast agent is generally introduced via the orifice in the nipple that has been identified as the source of the problematic discharge, but percutaneous injection with US guidance has been reported (23). Generally, a water-soluble iodine-based contrast agent is used, but Kaltenborn et al (24) reported the use of gadopentetate dimeglumine in a

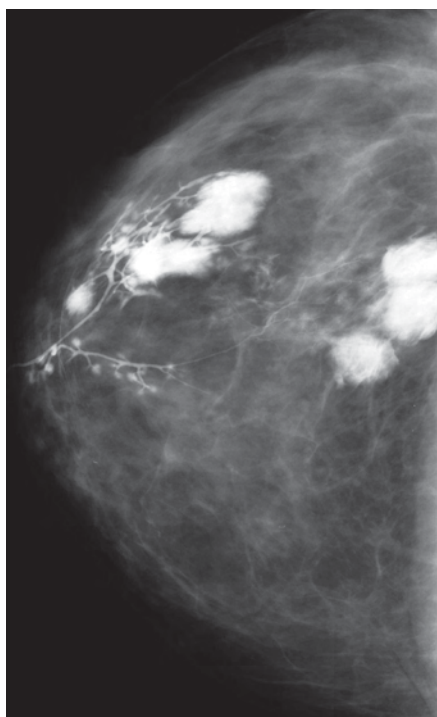


Figure 4. Galactogram showing enhancement of the ductal system and some areas of ductal extravasation.

patient who had previously had an adverse reaction to an iodinated contrast agent administered for a urographic examination. These investigators (24) also noted that approximately 10 years earlier, a patient undergoing galactography with an iodinated contrast agent did have an adverse reaction. Although adverse reactions to iodinated agents are well known with respect to protocols that introduce iodinated contrast material into the bloodstream, galactography intends to introduce contrast material only into the ductal lumen. In this context, it is noteworthy that Cabioglu et al (25), in a study of the differential diagnosis of nipple discharge, reported that one patient had "an unusual communication between the ductal system and a large mammary vein just medial to the nipple." This patient had presented with a bloody nipple discharge, and this discharge was reported to have resolved spontaneously over the course of several months.

Galactography permits examination of the ductal system because the ductal lumen is made opaque by the introduction of contrast material. The study by Cabioglu et al (25) used a classification system that fairly well represents the variety of findings typical for galactography. Typical abnormal findings on galactograms (25,26) include (a) filling defects and dilatation; (b) cutoff, narrowing, and irregularity; (c) duct ectasia and dilatation; and (d) extravasation of contrast material. Figure 4 is an example of a screen-film alactogram. Although some investigators, like Cabioglu et al (25), have found galactography to be sensitive but not specific, others suggest that a negative galactogram should not be seen as definitive (27,28). However, even if galactography is of limited diagnostic use, it can be

useful in localizing lesions and preparing for surgery (26).

The introduction of digital detectors will probably have only modest effects on the practice of galactography. The increased quantum efficiency might permit a somewhat lower dose, and the images will be available within seconds, as opposed to the several minutes required to process film. It is reasonable, however, to consider temporal subtraction techniques in digital galactography, which should result in increased conspicuity of opacified structures. Sufficient experience with screen-film galactography has accrued to show the broad outlines of what the technique can accomplish, although the findings from some recent preliminary work to quantify the branching structures of ductal trees indicates that there might be important information in galactograms that has not yet been exploited clinically (29).

Along the lines of galactography, several other possible examinations involve injection of contrast agent directly into the breast. Suga et al (30) reported the results of a study of contrast-enhanced CT of the lymph nodes in a canine model and also reported the depiction of mammary lymph nodes in one human volunteer. In 1975, Weshler et al (31) described (a) "pneumomammography," in which oxygen was injected under pressure to inflate the breast, and (b) "pneumocystography," in which oxygen was used to inflate aspirated cysts. The breast would then be imaged by using the trapped oxygen as a negative contrast agent.

OTHER IMAGING TECHNIQUES

All techniques discussed so far use the differential attenuation of the primary x-ray beam by various tissues. Here, *attenuation* refers to either photoelectric absorption of the incident x-ray beam or scattering at a relatively large angle (1° or more). The linear attenuation coefficient, however, is only one of the physical parameters with which tissues can be differentiated. X-rays are electromagnetic waves, although the small wavelength (a few billionths of a centimeter) makes the wavelike properties difficult to observe. For example, it is conventional and useful to picture x-rays traveling along straight lines from the x-ray focus to the imaging plane (unless they undergo attenuation). Sound waves, on the other hand, readily travel around obstacles, so that one can hear sounds emanating from other rooms and places outside of one's line-of-sight. However, by looking at scattering at angles substantially less than 1° , and by using appropriate x-ray sources, such as microfocus x-ray tubes or synchrotrons, one can demonstrate that x-rays undergo refraction by ordinary materials, as light does when passing through bent glass. In addition, one can also detect small-angle diffraction of x-rays.

From a physical point of view, refraction is related to the fact that basic electromagnetic parameters (eg, the dielectric constant) vary across relatively macroscopic boundaries, on the scale of the border of a small cyst, while diffraction can be considered the result of these parameters varying periodically either on the scale of atoms or, more important for small angles, on the scale of macromolecules. The methods for collecting and interpreting such data are in the early stages of development, so only a few examples will be given here.

Pisano et al (32) used a synchrotron light source to obtain a relatively wide (about 10 cm), coherent monoenergetic x-ray beam. *Coherent* here means that the crests and troughs of the electromagnetic waves emanating from the x-ray source are crest-to-crest and trough-to-trough across the width of the beam. This beam was passed through an appropriately mounted anatomic specimen and then reflected from a carefully adjusted, nearly perfect crystal, so that the reflected beam fell on an imaging device, in this case a CR system. Thus, a reflection of the x-ray shadow was recorded. However, unlike an x-ray shadow achieved with conventional devices, by imaging the reflection from an appropriately positioned crystal, all x rays that have been scattered by as little as a few seconds of arc⁴ were removed from the image. This is somewhat like using a grid with a million-to-one aspect ratio! Further, at this level of angular resolution, part of the observed "scatter" is due to effects such as refraction of the x-ray beam at various anatomic surfaces or diffraction from macromolecules such as collagen. In addition, by rotating the crystal slightly from the position appropriate for maximum scatter rejection, it is possible to produce images in which both the attenuated direct beam and part of the scattered beam contribute to the observed signal. Pisano et al (32) refer to their work as "diffraction-enhanced" imaging.

A related class of techniques are the "phase-contrast" techniques, which seek to use the refraction and diffraction of x rays passing near the boundaries of anatomic structures to enhance the contrast of images. Again, one needs an x-ray source that is more "coherent" than ordinary sources, for example, a synchrotron or a micro-focus x-ray tube placed several meters from the object or patient to be imaged. Further, the imaging device must also be placed several meters away from the object or patient being imaged so that the pattern of diffraction and refraction, which subtends only a fraction of a degree of arc, can spread out sufficiently to be discernible on the imaging device but not so far away that the resulting patterns from all regions being examined overlap. Recently, Olivo et al (33) described attempts to overcome some of these problems, in particular the limited sampling pitch of digital detectors.

Clearly, these technologies, while interesting, are still speculative. Even when adapted to use micro-focus tubes, the increased source-detector distances required result in the need for great tube loading, if one is to perform an examination in a reasonable amount of time. Future developments are difficult to predict, but major advances in x-ray sources would seem to be needed to make these technologies affordable for general use. In the meanwhile, there is clearly room for basic research on the nature and sources of contrast related to both the wave and particulate nature of x rays.

References

1. Johns PC, Yaffe MJ. X-ray characterization of normal and neoplastic breast tissues. *Phys Med Biol* 1987; 32:675–695.
2. Johns PC, Yaffe MJ. Theoretical optimization of dual-energy x-ray imaging with application to mammography. *Med Phys* 1985; 12:289–296.
3. Alvarez RE, Macovski A. Energy-selective reconstructions in x-ray computerized tomography. *Phys Med Biol* 1976; 21:733–744.
4. Lehmann LA, Alvarez RE, Macovski A, Brody WR. Generalized image combinations in dual kVp digital radiography. *Med Phys* 1981; 8:659–667.
5. Johns PC, Drost DJ, Yaffe MJ, Fenster A. Dual-energy mammography: initial experimental results. *Med Phys* 1985; 12:297–304.
6. Asaga T, Masuzawa C, Yoshida A, Matsuura H. Dual-energy subtraction mammography. *J Digit Imaging* 1995; 8:70–73.
7. Fabbri S, Taibi A, Longo R, et al. Signal-to-noise ratio evaluation in dual energy radiography with synchrotron radiation. *Med Phys* 2002; 47:4093–4105.
8. Folkman J. The role of angiogenesis in tumor growth. *Semin Cancer Biol* 1992; 3:65–71.
9. Folkman J, Long D, Becker F. Growth and metastasis of tumor in organ culture. *Cancer* 1963; 16:453–467.
10. Knopp MV, Weiss E, Sinn HP, et al. Pathophysiologic basis of contrast enhancement in breast tumors. *J Magn Reson Imaging* 1999; 10:260–266.
11. Nunes LW, Englander SA, Charafeddine R, Schnall MD. Optimal post-contrast timing of breast MR image acquisition for architectural feature analysis. *J Magn Reson Imaging* 2002; 16:42–50.
12. Leach MO. Application of magnetic resonance imaging to angiogenesis in breast cancer. *Breast Cancer Res* 2001; 3: 22–27.
13. Chao TC, Lo YF, Chen SC, Chen MF. Color Doppler ultrasound in benign and malignant breast tumors. *Breast Cancer Res Treat* 1999; 57:193–199.
14. Akashi-Tanaka S, Fukutomi T, Miyakawa K, Uchiyama N, Nanasawa T, Tsuda H. Contrast-enhanced computed tomography detection of occult breast cancers presenting as axillary masses. *Breast Cancer Res Treat* 1999; 55:97–101.
15. Akashi-Tanaka S, Fukutomi T, Miyakawa K, Uchiyama N, Tsuda H. Diagnostic value of contrast-enhanced computed tomography for diagnosing the intraductal component of breast cancer. *Breast Cancer Res Treat* 1998; 49:79–86.
16. Watt AC, Ackerman LV, Shetty PC, et al. Differentiation between benign and malignant disease of the breast using digital subtraction angiography of the breast. *Cancer* 1985; 56:1287–1292.
17. Watt AC, Ackerman LV, Windham JP, et al. Breast lesions: differential diagnosis using digital subtraction angiography. *Radiology* 1986; 159:39–42.

18. Ackerman LV, Watt AC, Shetty P, et al. Breast lesions examined by digital angiography: work in progress. *Radiology* 1985; 155:65–68.
19. Skarpathiotakis M, Yaffe MJ, Bloomquist AK, et al. Development of contrast digital mammography. *Med Phys* 2002; 29:2419–2426.
20. Jong RA, Yaffe MJ, Skarpathiotakis M, et al. Contrast-enhanced digital mammography: initial clinical experience. *Radiology* 2003; 228:842–850.
21. Diekmann F, Diekmann S, Taupitz M, et al. Use of iodine-based contrast media in digital full-field mammography: initial experience. *Rofo Fortschr Geb Rontgenstr Neuen Bildgeb Verfahr* 2003; 175:342–345. [German]
22. Lewin JM, Isaacs PK, Vance V, Larke FJ. Dual-energy contrast-enhanced digital subtraction mammography: feasibility. *Radiology* 2003; 228:261–268.
23. Rissanen T, Typpo T, Tikkakoski T, Turunen J, Myllymaki T, Suramo I. Ultrasound-guided percutaneous galactography. *J Clin Ultrasound* 1993; 21:497–502.
24. Kaltenborn H, Schadmand S, Beck T, Thelen M. Gadolinium-DTPA (Magnevist) as contrast medium for galactography. *Rofo Fortschr Geb Rontgenstr Neuen Bildgeb Verfahr* 1995; 163:457–459. [German]
25. Cabioglu N, Hunt KK, Singletary SE, et al. Surgical decision making and factors determining a diagnosis of breast carcinoma in women presenting with nipple discharge. *J Am Coll Surg* 2003; 192:354–364.
26. Rongione AJ, Evans BD, Kling KM, McFadden DW. Ductography is a useful technique in evaluation of abnormal nipple discharge. *Am Surg* 1996; 62:785–788.
27. Dawes LG, Bowen C, Venta LA, Morrow M. Ductography for nipple discharge: no replacement for ductal excision. *Surgery* 1998; 124:685–691.
28. Sickles EA. Galactography and other imaging investigations of nipple discharge. *Lancet* 2000; 356:1622–1623.
29. Bakic PR, Albert M, Maidment AD. Classification of galactograms with ramification matrices: preliminary results. *Acad Radiol* 2003; 10:198–204.
30. Suga K, Ogasawara N, Yuan Y, Okada M, Matsunaga N, Tangoku A. Visualization of breast lymphatic pathways with an indirect computed tomography lymphography using a nonionic monometric contrast medium iopamidol. *Invest Radiol* 2003; 38:73–84.
31. Weshler Z, Horn Y, Siew F. Experience with contrast mammography in the diagnosis of various breast diseases. *Isr J Med Sci* 1975; 11:448–457.
32. Pisano ED, Johnston RE, Chapman D, et al. Human breast cancer specimens: diffraction-enhanced imaging with histological correlation—improved conspicuity of lesion detail compared with digital radiography. *Radiology* 2002; 214:895–901.
33. Olivo A, Arfelli F, Cantatore G, et al. An innovative digital imaging set-up allowing a low-dose approach to phase contrast applications in the medical field. *Med Phys* 2001; 28:1610–1619.

Quantification for contrast-enhanced digital breast tomosynthesis

Ann-Katherine Carton*, Jingjing Li, Michael Albert, Sara Chen, Andrew D.A. Maidment
Hospital of the University of Pennsylvania, 19104 Philadelphia, PA USA

ABSTRACT

Digital breast tomosynthesis (DBT) is a tomographic technique in which individual slices through the breast are reconstructed from x-ray projection images acquired over a limited angular range. In contrast-enhanced DBT (CE-DBT) functional information can be observed by administration of an x-ray contrast agent. We have investigated the technical requirements necessary to quantitatively analyze CE-DBT exams. Using a simplified physiological model, a maximum aerial concentration of approximately 2.2 mg iodine/cm² in a 0.5 cm thick breast lesion is expected when administering 70 ml of 320 mg iodine/ml Visipaque-320®. This corresponds to a small change in x-ray transmission; up to 5 % for a 4 cm thick compressed breast. We have modeled CE-DBT acquisition by simulating Rh target x-ray spectra from 40 to 49 kV. Comparison of attenuation data of our simulated and measured spectra were found to agree well. We investigated the effect of scatter, patient motion and temporal stability of the detector on quantifying iodine uptake. These parameters were evaluated by means of experiments and theoretical modeling.

Keywords: Digital breast tomosynthesis, quantification, contrast agents, angiography

1. INTRODUCTION

Breast tumor growth and metastasis are accompanied by the development of new blood vessels¹. These vessels are of poor quality and tend to leak. As a result, blood pools around the tumor. An imaging technique using a vascular contrast agent should be able to demonstrate and characterize the tumor and its vessels. Today, the best choice for imaging tumor vasculature in 3D is Contrast Enhanced-Magnetic Resonance imaging (CE-MRI) with a gadolinium based contrast agent². CE-MRI is, however, expensive and time consuming and therefore unlikely to become widely available. We believe that Contrast-Enhanced Digital Breast Tomosynthesis (CE-DBT) would be a less expensive and less time consuming alternative to CE-MRI. It would potentially integrate the benefits of both CE digital mammography³⁻⁵ and DBT⁶; thus, providing both functional information and improved breast cancer morphology by minimizing the superimposition of nonadjacent breast tissues that occurs with projection mammograms. Temporal analysis of contrast enhancement may further help to distinguish benign and malignant lesions.

In CE-DBT an iodinated contrast agent is used. The greatest subject contrast that can be produced with an iodinated contrast agent is by using x rays with energies just above the K-edge of iodine. In the experiments described, we have used temporal subtraction. High energy images are acquired before and after administration of the contrast agent^{3, 4} (Figure 1). Logarithmic subtraction of these images is then performed. The signal intensities (SI) of the resulting images are proportional to the uptake of iodine.

The uptake of iodine in the breast is very small and thus causes only small changes in x-ray transmission; less than 5 %. This presents significant technical challenges if quantitative assessment of contrast agent uptake is desired. Technical factors that significantly influence quantitative analysis of CE-DBT exams are exposure reproducibility, linearity of the detector as a function of position, scatter, patient motion and temporal stability of the detector. In this paper, we will discuss scatter, patient motion and the temporal stability of the detector.

We have used a modified GE 2000D under IRB approval, to gain initial experience in CE-DBT. To date we have acquired 13 CE-DBT clinical cases.

* Ann-Katherine.Carton@uphs.upenn.edu; Phone: 215 746 8759; Fax: 215 746 8764

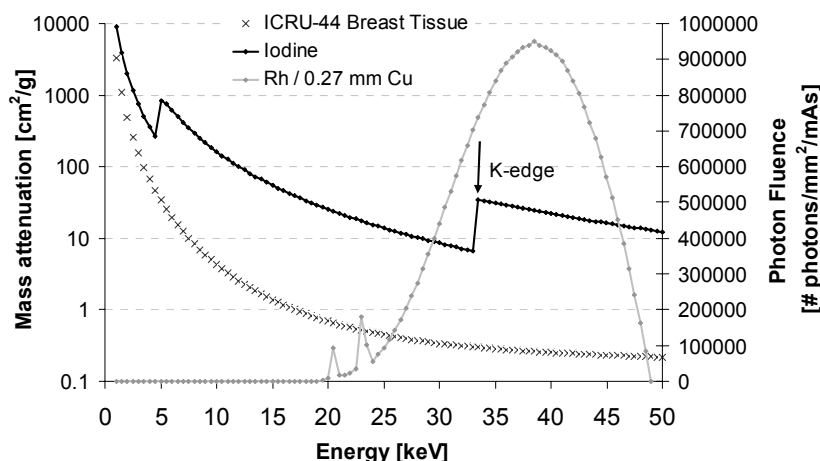


Figure 1: Mass attenuation data of ICRU-44 breast tissue and iodine. Example of a high energy x-ray spectrum from a Rh target exposed at 49 kV filtered with 0.27 mm Cu.

2. SIMPLE PHYSIOLOGICAL MODEL

We have developed a simple physiological model of breast tumors in order to determine the maximum uptake of a breast lesion. This uptake will be used as a point of comparison when considering factors which can alter the quantitative measurement of iodine uptake. We have considered a uniform contrast-agent/blood mixing model. Our model is based on the following assumptions: 1) the average adult has 5 l of blood pumped by the heart through the entire body in 1 min; 2) the time for an intravenous injection of contrast-agent is comparable to time for the heart to pump 5 l of blood; 3) the maximum concentration in the extracellular space is equal to the maximum intravascular concentration; and 4) the half-life of iodine in blood is long compared to the time of the clinical exam (~ 10 min). In our clinical trial, we used Visipaque-320® (320 mg iodine/ml iodixanol, Amersham, Princeton, NJ) injected at 1 ml/kg bodyweight followed by a saline flush. As an example, for a 70 ml Visipaque-320® injection, the maximum iodine concentration expected in the blood will be 4.5 mg/ml. In this instance, a 0.5 cm thick tumor would have an aerial density of ~ 2.2 mg/cm².

3. X-RAY SPECTRUM

We have modeled the x-ray spectrum in order to study how the quantification of iodine uptake is influenced by scatter, patient motion and temporal response of the detector. We simulated x-ray spectra in the range of 40 to 49 kV by extrapolating Boone's model⁷. Boone parameterized spectra measured at the FDA for Mo, Rh and W target x-ray tubes operated between 18 and 40 kV. Each energy bin in the spectra was fitted in terms of the photon fluence as a function of kV using first, second order or third order polynomials. We believe that these data are over-fitted. This will become evident when we consider how to extrapolate the data.

In this paper, we will only discuss the extrapolation of the Rh target spectra as Rh is the target that we have used to acquire our CE-DBT exams. The extrapolation was split in two parts. First, below 24 keV we used the parameters from Boone's paper for the extrapolated kVs. Second, above 24 keV, which we will refer to as the tails of the spectra, we refitted the spectra. In performing our fits, we assumed that: 1) for a given kV the photon fluence in the tails are linear with keV; 2) the slopes of the linear fits of the tails decrease with increasing kV; and 3) the photon fluence is zero at the maximum energy of each spectrum.

In Figure 2 we show spectra between 26 and 49 kV using Boone's parameters. Note that the shapes of the extrapolated spectra (grey) are similar to the published ones (black). Figure 2 b shows the low energy part in detail. The fluctuations in the extrapolated data are clearly artifactual. We have not addressed these artifacts as this low energy range is not of significance in imaging iodine. Next, consider the characteristic radiation peaks. Theoretically, for a thin target, the ratio of the K_{α} to K_{β} peak is constant⁸; for a Rh target this ratio is 5.46. The target of an x-ray tube is not thin, but to a first approximation we can consider it as thin because the electrons incident on the anode are much less penetrating than the

fluorescent x rays. Figure 3 shows that K_{α}/K_{β} decreases starting at 38 kV. This decrease may be due to erroneous fitting. However, it could also be explained by beam hardening in the thick Rh target. This would be consistent with our data, as beam hardening would cause the fraction of K_{β} to increase. Figure 2 c is a detail of the tails. Again one can see the effect of over-fitting. We could have kept the tails as they are and extrapolated them beyond 40 keV. However, as this energy range is of significance in imaging iodine, we chose to refit them. Using the assumptions stated above, we calculated the slopes of the tails for the spectra from 34 to 40 kV. The slopes were calculated from 26.5 keV using linear interpolation. We applied a least squares fit and used this fit to estimate the slopes of the tails of the extrapolated spectra. Figure 2 c shows our fits. In analogy with Boone's model, the photon fluences were fitted as function of kV for each energy bin. We applied first, second and third order fits. We chose the simplest fit for each energy bin. The residuals between the fits and the data were 2 orders of magnitude smaller than the actual data.

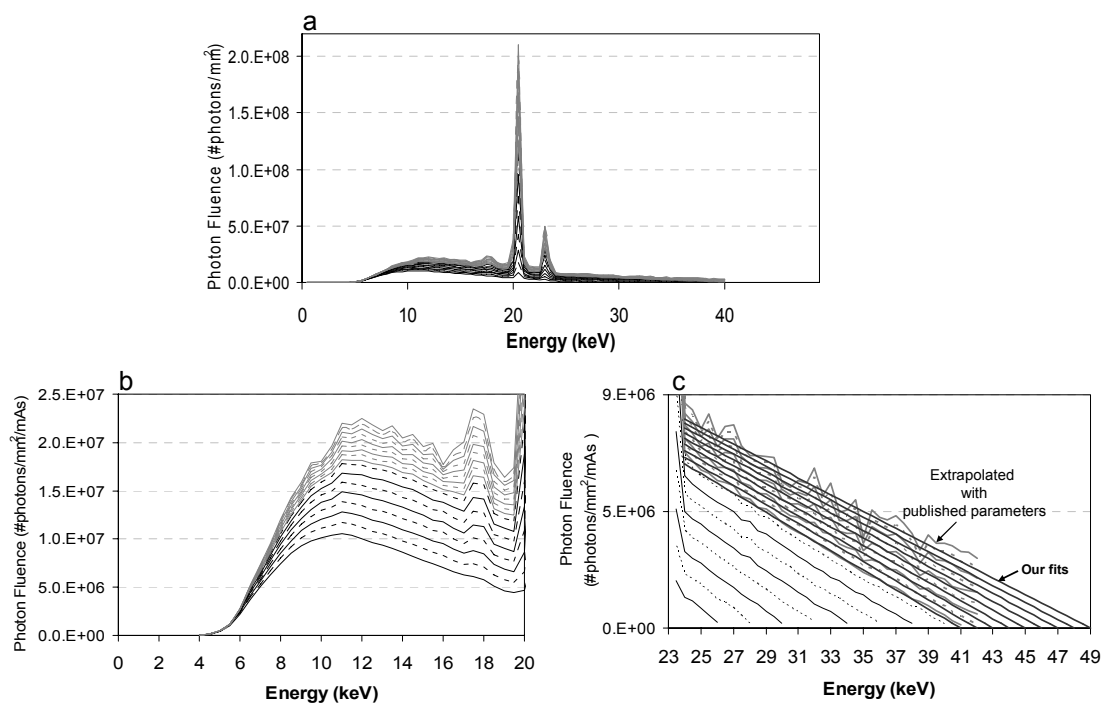


Figure 2: a) X-ray spectra from 26 kV to 49 kV using Boone's parameters. Note that the extrapolated spectra (grey) have the same shape as the published spectra by Boone (black). b) Detail of the low-energy region of the spectra shown in a). Note that the fluctuations in the extrapolated spectra are artifactual. c) Detail of the tails of the spectra shown in a). These fluctuations are also artifactual.

We validated our simulations using a least-squares comparison (i.e., minimizing the χ^2 values) between measured and simulated attenuation data. We used Al filters (99.997 % pure, Alfa Aesar, Ward Hill, MA) to determine the attenuation curves. The minimum χ^2 was found by adjusting the kV ($kV_{\text{equivalent}}$) and adding extra Al ($Al_{\text{equivalent}}$) to the simulated spectra. We also compared the half value layers (HVL), quarter value layers (QVL), eight value layers (EVL) and tenth value layers (TVL) of the measurements and the simulations. The measurements were performed with a Senographe 2000D (GE Medical Systems, Milwaukee, WI). The Senographe 2000D was operated with a Rh target and 0.25 mm Rh or 0.27 mm Cu filtration. We used the Cu filter to emphasize the tails. The tube has a 0.69 mm thick Be window; a 2 mm thick compression paddle was in the x-ray beam; the distance from the target to the exposure meter was 43 cm.

We modeled this system by filtering our fitted Rh spectra with added filtration simulated to match the experimental setup. Tables 1 and 2 demonstrate that the extrapolation of Boone's spectral models agree well with our measurements. Shown are the equivalent kV ($kV_{\text{equivalent}}$) and equivalent Al filtration ($Al_{\text{equivalent}}$) of the simulated spectra for a nominal kV that results in the smallest χ^2 . HVL and QVL are also presented for Rh and Cu filters; EVL and TVL are only presented for the Rh filter. The largest difference between the measured and simulated HVL, QVL, EVL and TVL is 1.8 % for the QVL at 49 kV with a Rh filter (48 $kV_{\text{equivalent}}$ and 0 mm $Al_{\text{equivalent}}$). Figure 5 show examples of Rh spectra

filtered with 0.27 mm Cu. The largest difference between the measured and simulated HVL and QVL is 1.3 % for the QVL at 34 kV (33.5 kV_{equivalent} and 0 mm Al_{equivalent}). This occurs in the range of energies fitted by Boone. In the extrapolated range, the largest difference, 0.6 %, was found for the QVL at 49 kV (48.4 kV_{equivalent} and 0 mm Al_{equivalent}).

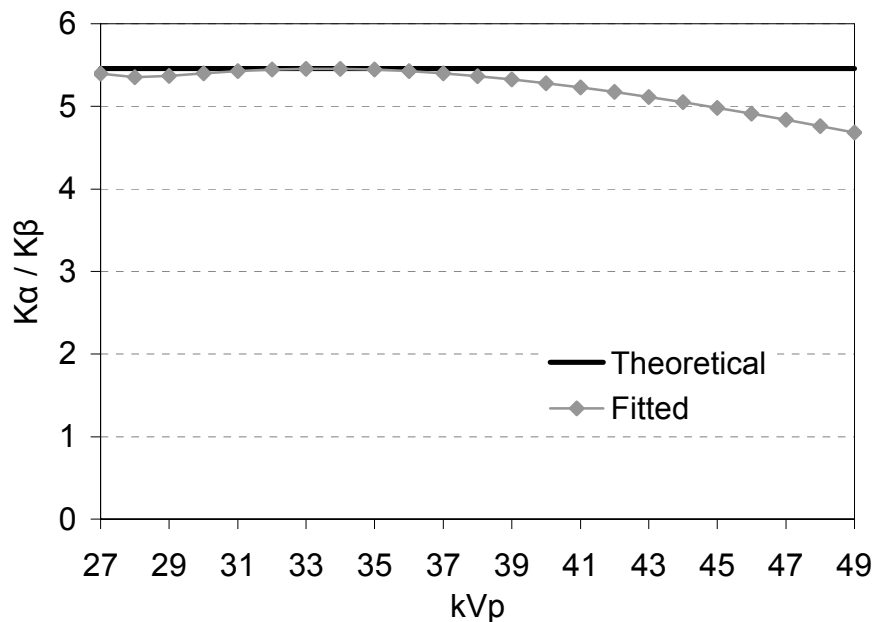


Figure 3: K_{α}/K_{β} for a thin Rh target (theoretical) and as calculated in the fitted spectra. Note that K_{α}/K_{β} decreases from 38 kV.

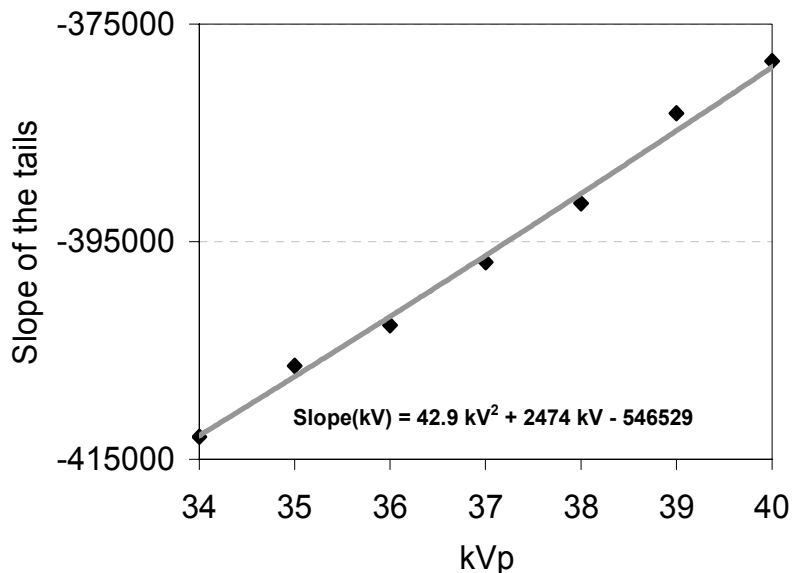


Figure 4: Slopes of the tails for the published spectra from 34 to 40 kV. A least squares fit was used to determine the slopes of the tails of the extrapolated spectra.

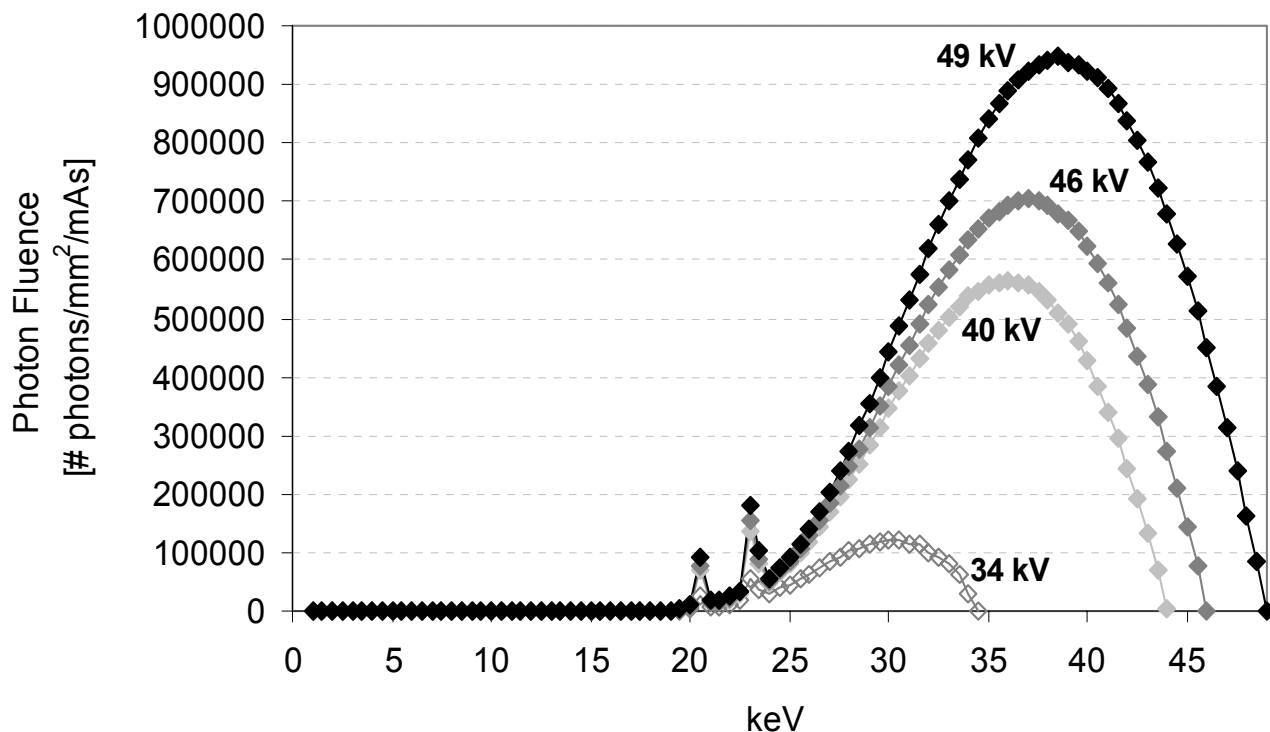


Figure 5: Examples of x-ray spectra from a Rh target filtered with 0.27 mm Cu. The fluence is specified 43 cm from the target.

Table 1: Comparison of the measured and simulated attenuation data for a Rh target filtered with 0.25 mm Rh. HVL, QVL, EVL and TVL are expressed in mm Al.

Nominal kV	kV _{equivalent}	Al _{equivalent}	Measured				Simulated				
			HVL	QVL	EVL	TVL	HVL	QVL	EVL	TVL	X ²
25	25.3	0.000	0.361	0.820	1.382	1.574	0.359	0.822	1.378	1.573	0.0001
28	28.4	0.000	0.412	0.949	1.589	1.818	0.411	0.950	1.593	1.819	0.0001
34	33.5	0.000	0.478	1.116	1.868	2.120	0.482	1.114	1.859	2.118	0.0001
40	39.8	0.000	0.556	1.244	2.088	2.382	0.546	1.258	2.092	2.384	0.0001
46	45.0	0.000	0.578	1.341	2.228	2.575	0.586	1.346	2.243	2.563	0.0005
49	48.0	0.000	0.612	1.365	2.309	2.625	0.605	1.390	2.325	2.662	0.0006

Table 2: Comparison of the measured and simulated attenuation data for a Rh target filtered with 0.27 mm Cu. HVL and QVL are expressed in mm Al.

Nominal kV	kV _{equivalent}	Al _{equivalent}	Measured		Simulated		
			HVL	QVL	HVL	QVL	X ²
34	33.5	0.0	1.711	3.532	1.713	3.579	0.0001
40	39.4	0.0	2.232	4.750	2.238	4.738	0.0001
46	45.5	0.0	2.779	5.978	2.787	5.978	0.0001
49	48.4	0.0	3.060	6.619	3.063	6.578	0.0001

4. SCATTER

We performed CE-DBT without a grid. We have performed experiments to determine the effect of scatter on the quantification of iodine uptake. The magnitude of the scatter was determined using the scatter fraction, SF :

$$SF = \frac{S}{S + P}$$

where S is scatter and P is primary radiation. SF was measured with Pb-disks⁹ with diameters from 3.9 to 11 mm. The signal intensities (SI) in the shadows of the Pb-disks and in an unperturbed ROI were measured. The logarithms of the measured SF as a function of Pb-disk diameter were plotted. The inverse logarithm at zero disk diameter of a linear fit through the measured values gave the SF for an infinitesimally small disk. These measurements were repeated as a function of position and breast equivalent thickness in 50 % glandular-50 % fatty breast equivalent phantoms (CIRS, Norfolk, VA). The phantoms were positioned so as to mimic the MLO position, including higher order scatter from the chest (Figure 6 a). A 49 kV spectrum with a 0.27 mm Cu filter was used.

4.1. Scatter dependence as a function of position in the breast.

Figure 6 b shows the SF as a function of position in the breast. The SF is smaller at the lateral sides of the breast equivalent phantoms. The SF is slightly asymmetric across the centerline of the breast phantom. As expected, the SF increases from the chest wall side towards the center of the breast and then falls off again towards the nipple side. The SF varies significantly over the field of view. For example, for a 60 mm 50 % glandular-50 % fatty breast equivalent phantom, the SF at the edge of the breast phantom is 0.31, but it increases to 0.52 near the center of the field.

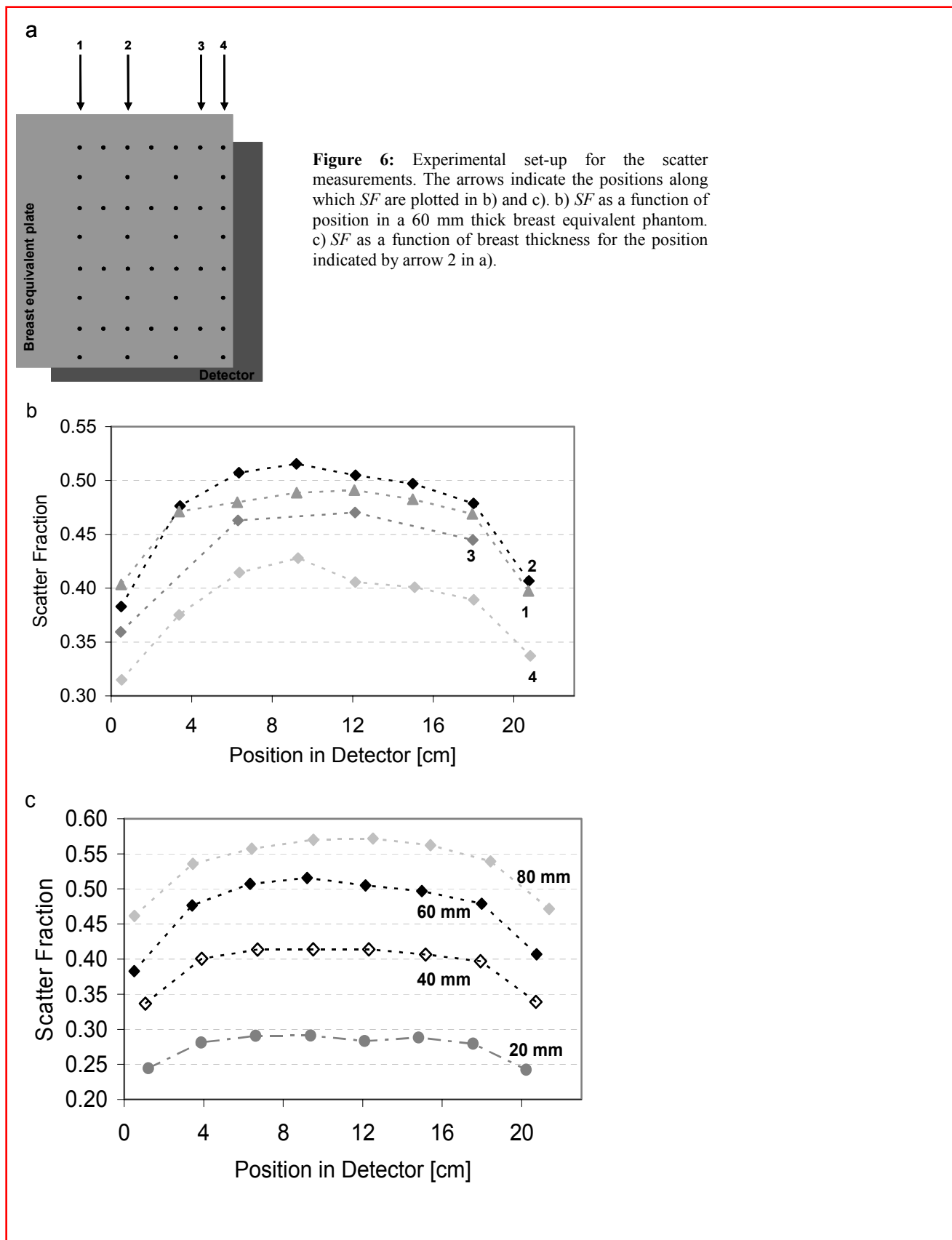
4.2. Scatter dependence as a function of breast thickness.

Figure 6 c illustrates SF profiles for 2 cm, 4 cm, 6 cm and 8 cm thick breast equivalent phantoms. The SF profiles are shown for the position in the phantom labeled "2" in Figure 6 a. As expected, the SF is higher for thicker breasts.

4.3. Effect of scatter on the quantification of the iodine concentration

We modeled the effect of scatter on the quantification of the iodine concentration for various breast thicknesses. To do so, we simulated a Senographe 2000D tube operated at 49 kV with a Rh target and 0.27 mm Cu filtration. The simulation includes the attenuation of the Be-window, Cu-filter, compression plate, air, ICRU-44 breast tissue, and the CsI detector. We used the SF measured near the center of the breast equivalent phantoms. We calculated the contrast as a function of iodine uptake for the various breast thicknesses and calculated then the error in the iodine concentration estimate due to the scatter.

Figure 7 shows the extent to which the iodine concentration will be underestimated if not corrected for scatter. For example, consider a 2.5 mg/cm² iodine concentration. Failure to correct for scatter will result in an underestimation of the iodine concentration by 28 % for a 20 mm breast thickness, 40 % for a 40 mm breast thickness, 47 % for a 60 mm breast thickness and 54 % for a 80 mm breast thickness. Failure to correct for scatter when using a grid also results in an underestimation of the iodine concentration by 22 % for a 40 mm thick breast. This is relevant for quantitative CE-digital mammography.



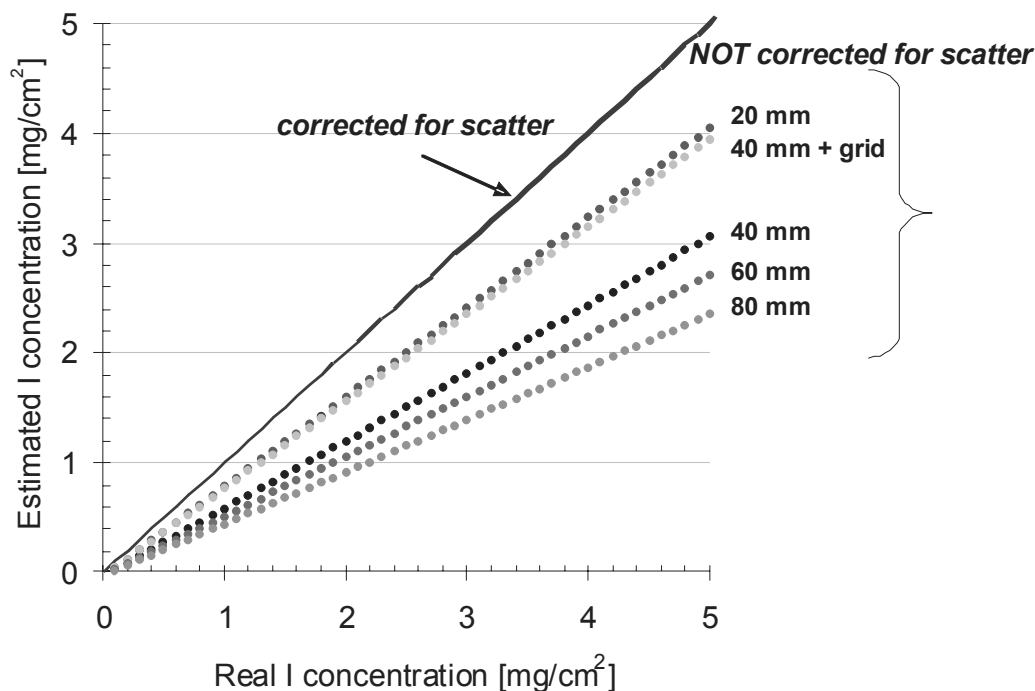


Figure 7: Iodine concentration will be underestimated if not corrected for scatter. The simulation parameters were a Rh target, 49 kV and 0.27 mm Cu filter. No grid was used except where specified.

5. PATIENT MOTION

In temporal subtraction, images from pre- and post-contrast series are subtracted. Any breast motion between series will result in artifacts. In our experiments with patients, the total acquisition time can exceed 10 minutes. Breast motion is inevitable. We calculated the following measure to demonstrate the effect of breast motion on the estimated iodine uptake. In patient images, we selected ROIs with uniform breast thickness. The absolute values of relative SI variations were calculated between pixel positions that are Δx apart from each other. We varied Δx from 1 to 128 pixels (0.1 - 12.8 mm). We used SF measured near the center of the breast equivalent phantoms.

We calculated the contrast as a function of iodine uptake for the various displacements and then calculated the error in the iodine concentration estimate due to the displacements. These measurements were calculated for displacements in the horizontal and vertical direction. The relative SI variations were related to the corresponding estimates of iodine concentration to demonstrate the effect of motion on the quantification of iodine. Figure 8 a shows the SI in a homogenous ROI of a breast image acquired at 49 kV with a 0.27 mm Cu filter. The SF in this 45 mm thick ROI was ~ 0.40 . Figure 8 b and c show the relative SI variations arising from various displacements. Even for 1 pixel (0.1 mm) displacements, half of the pixel signal intensities vary by 0.7 % and the maximum change is 4.7 % (Figure 8 d). A 4.7 % SI variation would correspond to 2.3 mg/cm² iodine. That is greater than the 2.2 mg/cm² iodine that we predicted with our simple physiological model for a 0.5 cm lesion.

A clinical example of patient motion is illustrated in Figure 9. The image is the difference of a post-contrast projection image and a pre-contrast projection image. Two lead BBs were placed near the nipple of the patient. The arrows in the image demonstrate examples of patient motion. The lower BB shows a displacement of approximately 5 mm. We have found that the greatest motion in the breast generally occurs in the dependent (lower) portion of the breast.

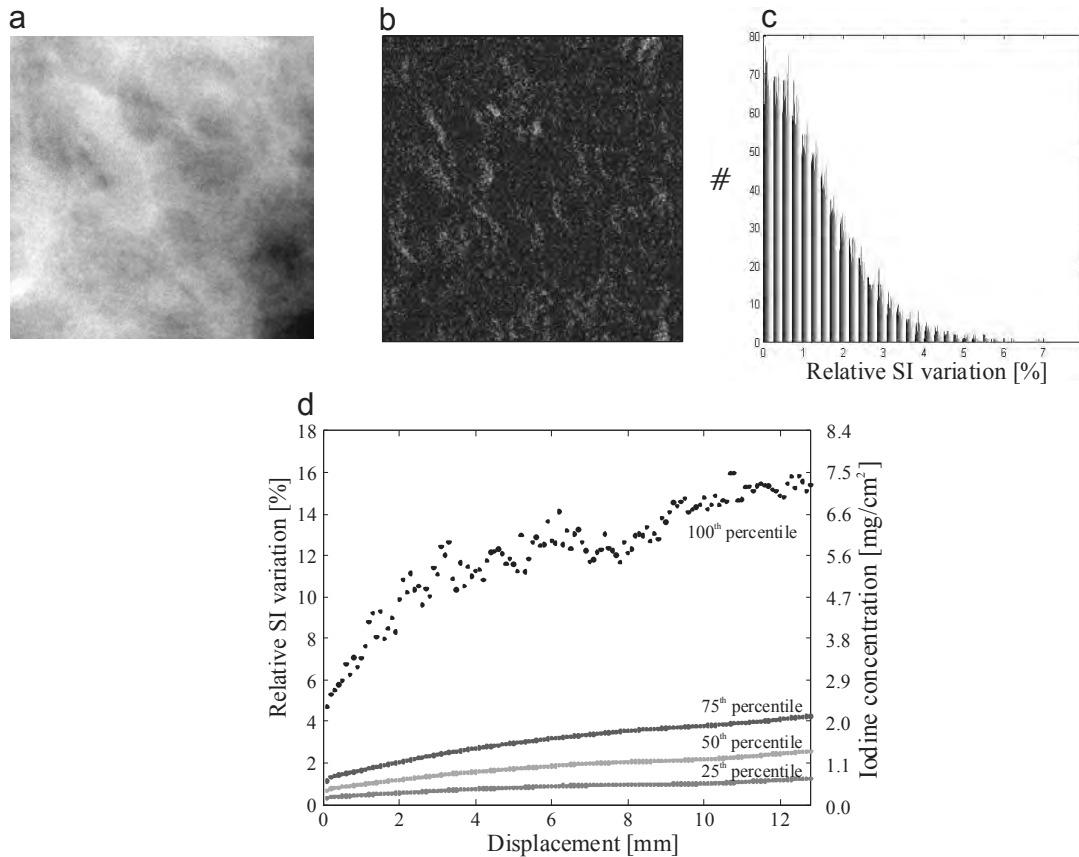


Figure 8: a) Example of a homogeneous ROI in a pre-contrast mammogram that has been acquired with a Rh target at 49 kV and with 0.27 mm Cu. b) Relative SI variations obtained by subtracting the ROI in a) shifted by 1 mm in the horizontal direction. c) Histogram of the relative SI variations shown in b). d) Relative SI variations arising from various displacements. The relative SI variations are equated with iodine uptake.

6. DETECTOR: TEMPORAL STABILITY

The stability of the temporal response of the detector depends on the exposure level, time delay between acquisitions and breast thickness¹⁰. Our experiments confirm the results presented by Jeunehomme *et al*¹⁰. The timing of the clinical CE-DBT projection images in our clinical trial at the University of Pennsylvania is as follows: nine projections are acquired while sweeping the x-ray tube over a 50° arc; one projection is acquired every 30 s; the first post-contrast image is obtained 90 s after the start of the contrast injection, and the x-ray tube is again swept over a 50° arc.

Figure 10 illustrates the relative SI variation as a function of time for a typical clinical acquisition sequence. A 40 mm PMMA plate was exposed at 49 kVp with a Rh target and 0.27 mm Cu filter. The SI in the detector was ~ 7000. This experiment was repeated 4 times. The error bars are a measure for the repeatability of the temporal instability. Based on our spectral model, the temporal response will result in an error in iodine uptake of ~8 % for a typical patient dose.



Figure 9: Example of patient movement. The image is the result of subtraction of a post-contrast projection image from a pre-contrast projection image. Two lead BBs were attached near the nipple. The arrows indicate patient motion.

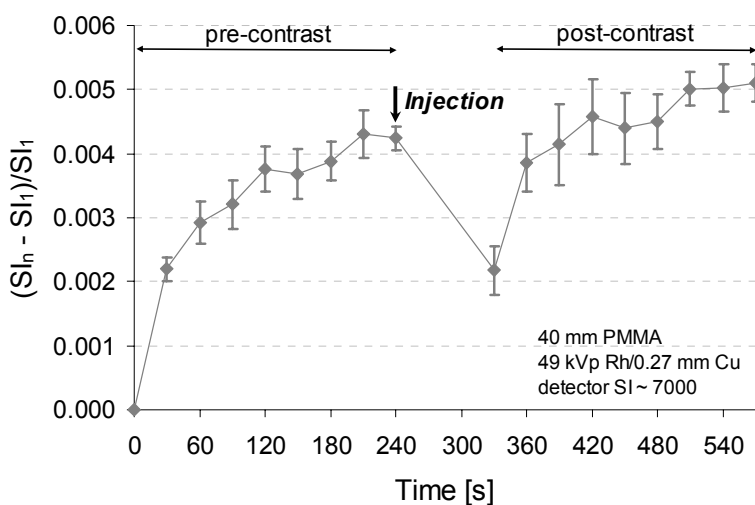


Figure 10: Example of the relative SI variation in a ROI of the nth image to the same ROI in the 1st image. The pre-contrast and post-contrast series each consist of an x-ray tube sweep in which 9 projection images are acquired. One image is acquired every 30 s. The first post-contrast image is acquired 90 s after the last pre-contrast image. The images were acquired under typical clinical conditions.

7. CONCLUSIONS

CE-DBT offers the potential to visualize the vascular characteristics of breast lesions as an adjunct to mammography. Based upon our initial clinical experience, and the work reported here, it is clear that the quantification of the iodine uptake for CE-DBT is complex. For the design of a CE-DBT system, attention should be paid to scatter and patient motion. At the current time, we are working on the reduction of patient motion and we are evaluating alternative subtraction methods using dual energy CE-DBT.

ACKNOWLEDGEMENT

We would like to thank the financial support of Philips Medical Systems/RSNA Research Seed Grant 2005 and the National Cancer Institute Grant PO1-CA85484. We would like to thank General Electric Medical Systems for their technical help. Interested parties should contact the first author to obtain a copy of the spectral parameters.

REFERENCES

1. Folkman, J., *The role of angiogenesis in tumor growth*. Seminars in Cancer Biology, 1992. **3**(2): p. 65-71.
2. Kaiser, W.A. and E. Zeitler, *MR imaging of the breast: fast imaging sequences with and without Gd-DTPA. Preliminary observations*. Radiology, 1993. **187**: p. 493-501.
3. Skarpathiotakis, M., et al., *Development of contrast digital mammography*. Medical Physics, 2002. **29**(10): p. 2419-26.
4. Jong, R.A., et al., *Contrast-enhanced digital mammography: Initial clinical experience*. Radiology, 2003. **228**: p. 842-850.
5. Lewin, J.M., et al., *Dual-energy contrast-enhanced digital subtraction mammography: Feasibility*. Radiology, 2003. **264**: p. 261-268.
6. Niklason, L.T., et al., *Digital tomosynthesis in breast imaging*. Radiology, 1997. **205**(2): p. 399-406.
7. Boone, J.M., T.R. Fewell, and R.J. Jennings, *Molybdenum, rhodium, and tungsten anode spectral models using interpolating polynomials with application to mammography*. Medical Physics, 1997. **24**(12): p. 1863-74.
8. http://xdb.lbl.gov/Section1/Table_1-3.pdf.
9. Fahrig, R., et al., *Performance of glass fiber antiscatter devices at mammographic energies*. Medical Physics, 1994. **21**(8): p. 1277-82.
10. Jeunehomme, F., et al., *Controlling gray level variation in contrast enhanced digital mammography: design of a calibration procedure*. Proceedings of SPIE, Physics of Medical Imaging, 2003. **5030**: p. 338-348.

Optimization of Contrast-Enhanced Digital Breast Tomosynthesis

Ann-Katherine Carton, Jingjing Li, Sara Chen, Emily Conant,
and Andrew D.A. Maidment

University of Pennsylvania, Department of Radiology,
3400 Spruce Street, Philadelphia, PA, USA, 19104
{ann-katherine.carton, sara.chen, emily.conant,
andrew.maidment}@uphs.upenn.edu

Abstract. Digital breast tomosynthesis (DBT) is a tomographic technique in which individual slices through the breast are reconstructed from x-ray projection images acquired over a limited angular range. In contrast-enhanced DBT (CE-DBT) functional information is observed by administration of a radiographic contrast agent. The uptake of iodine in the breast is very small and causes changes in x-ray transmission that are smaller than 5%. This presents significant technical challenges if quantitative assessment of contrast agent concentration in tissue is desired. We modeled CE-DBT acquisition by simulating x-ray spectra from 40 to 49 kV. Comparison of attenuation data of our simulated and measured spectra were found to agree well. We investigated the effect of patient motion and scatter on iodine uptake. These parameters were evaluated by means of experiments and theoretical modeling.

1 Background

Digital breast tomosynthesis (DBT) is a tomographic technique for imaging the breast morphology at a dose comparable to digital mammography. However, as breast tumor growth and metastasis are accompanied by neoangiogenesis, a functional tomographic imaging technique is desired. Contrast-enhanced digital breast tomosynthesis (CE-DBT) [1] would potentially integrate the benefits of both CE digital mammography [2, 3] and DBT [4-7]; thus, providing both functional information and improved breast cancer morphology by minimizing the superimposition of nonadjacent breast tissues that occurs with projection mammograms. Temporal analysis of contrast enhancement may further help to distinguish benign and malignant lesions.

The uptake of iodine in the breast is very small and thus causes only small changes in x-ray transmission; typically less than 5%. This presents significant technical challenges if quantitative assessment of contrast agent uptake is desired [1]. Technical factors that significantly influence quantitative analysis of CE-DBT exams are exposure reproducibility, linearity of the detector as a function of position, temporal response of the detector, scatter and patient motion. In this paper, we will discuss scatter, and patient motion.

2 Methods

We have used a modified GE 2000D under IRB approval to gain initial experience in CE-DBT. In the experiments described, we have used temporal subtraction. High energy images are acquired before and after administration of an iodinated contrast agent. Logarithmic subtraction of these images is then performed. The signal intensities (SI) of the resulting images are proportionally to the uptake of iodine.

2.1 Spectrum

To model the acquisition process, x-ray spectra in the range of 40 to 49 kV were simulated by extrapolating Boone's model [8]. We validated our simulations using a least-squares comparison (χ^2 values) between attenuation data from our simulated spectra and attenuation data measured with the GE Senographe 2000D. We used high-purity Al filters to determine the attenuation curves. Minimum χ^2 values were found by adjusting the kV ($kV_{\text{equivalent}}$) and adding or subtracting Al ($Al_{\text{equivalent}}$) to the simulated spectra. We also compared the half value layers (HVL) and quarter value layers (QVL) of the simulations and the measurements. In this paper, we compare simulated and measured attenuation data from a Mo-target with 1 mm Al filtration, and a Rh-target with 0.27 mm Cu filtration.

2.2 Scatter

We performed CE-DBT without a grid. Scatter, S , was estimated by extrapolation of signal intensity measurements under Pb-disks with diameters of 3.9 to 23 mm to a disk of zero diameter. Scatter fractions (SF) were then calculated as the fraction of S to the SI value in the open field at the same position, which consist of S and primary radiation, P . These measurements were repeated as a function of position in 50% glandular-50% adipose breast equivalent phantoms (CIRS, Norfolk, VA), and various breast equivalent thickness. The phantoms were positioned so as to mimic the MLO breast position, including higher order scatter from the chest. A 49 kV spectrum with a 0.27 mm Cu filter was applied.

As part of our clinical CE-DBT trial, we have measured SF in the MLO projection images of 6 patients. Pb-disks 12 mm in diameter were positioned on top of the compression plate while the breast was compressed and a series of projection images was acquired over a 50° arc (as measured at the fulcrum, 20 cm above the breast support). SF were then calculated from the SI measured in the shadows of the Pb-disks, giving S , and the SI was also measured at the same position in the previously acquired pre-contrast projection images, thus giving $P + S$. The SF in the clinical data were compared with the SF calculated from the 12 mm Pb-disks in the phantom images. The same mammography unit and spectrum were used as in the phantom measurements.

We modeled the effect of scatter on the quantification of the iodine concentration for various breast thicknesses. We simulated a Senographe 2000D tube operated at 49 kV with a Rh target and 0.27 mm Cu filtration. Our simulation includes the attenuation of the Be-window, Cu-filter, compression plate, air, ICRU-44 breast tissue, and the CsI detector material. We used the SF measured near the center of the breast equivalent phantoms. We calculated the contrast as a function of iodine uptake for the various breast thicknesses and then calculated the error in the iodine concentration estimate due to the scatter.

2.3 Patient Motion

In temporal subtraction, pre- and post-contrast images are subtracted. Any breast motion between series will result in artifacts and an erroneous estimate of the iodine uptake will be calculated. In our clinical trial, the total acquisition time could exceed 10 minutes, depending on the experimental protocol. Thus, breast motion is inevitable.

We developed a measure to demonstrate the effect of breast motion on the estimated iodine uptake. In 12 patient images, we selected ROIs where the breast thickness was constant. The relative SI variations, corrected for scatter by using measured SF, were calculated between pixel positions that are Δx apart from each other. We varied Δx from 1 to 128 pixels (0.1 - 12.8 mm). These measurements were calculated for displacements in the horizontal and vertical direction. The relative SI variations were related to corresponding iodine concentrations using our simulation. These simulations considered a Senographe 2000D x-ray tube operated at 49 kV with a Rh-target and 0.27 mm Cu filtration. The simulation includes the attenuation of the Be-window, Cu-filter, compression plate, air, ICRU-44 breast tissue, and the CsI detector material.

3 Results

3.1 Spectrum

A comparison of the simulated and measured attenuation data are presented in Tables 1 and 2. The measured attenuation data in Table 1 are from a GE Senographe 2000D operated with a Rh-target and 0.27 mm Cu filtration. The tube has a 0.69 mm Be window, and a 2 mm compression plate was in the x-ray beam. The measured attenuation data in Table 2 are from a GE DMR. The Mo-target x-ray source was used with 1 mm Al filtration. The x-ray tube window was composed of 0.69 mm thick Be and a 2 mm compression plate was again in place.

Table 1. Comparison of the measured and simulated attenuation data for a Rh-target tube filtered with 0.27 mm Cu

nominal kV	kV _{equivalent}	Al _{equivalent}	Measured		Simulated		χ^2
			HVL	QVL	HVL	QVL	
34	33.5	0.0	1.711	3.532	1.713	3.579	0.00009
40	39.4	0.0	2.232	4.750	2.238	4.738	0.00012
46	45.5	0.0	2.779	5.978	2.787	5.978	0.00005
49	48.4	0.0	3.060	6.619	3.063	6.578	0.00006

Table 2. Comparison of the measured and simulated attenuation data for a Mo-target tube filtered with 1 mm Al

nominal kV	kV _{equivalent}	Al _{equivalent}	Measured		Simulated		χ^2
			HVL	QVL	HVL	QVL	
22	21.1	0.075	0.388	1.285	0.385	1.286	0.00007
28	28.0	0.100	0.538	1.844	0.540	1.841	0.00005
34	35.0	0.050	0.607	2.050	0.609	2.197	0.00009
40	39.4	0.100	0.654	2.420	0.649	2.442	0.00070
46	45.4	0.150	0.698	2.734	0.686	2.736	0.00071
49	49.0	0.175	0.739	2.907	0.703	2.911	0.00422

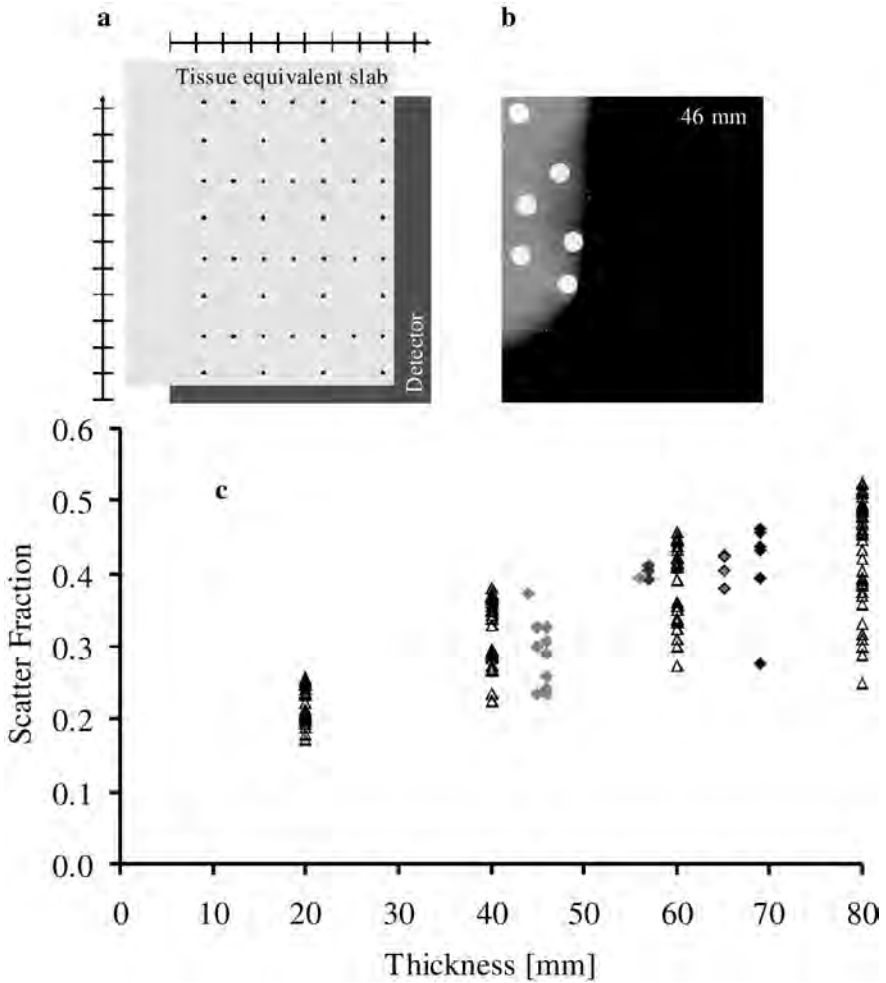


Fig. 1. (a) Geometry of the scatter measurements; 50% glandular, 50% adipose breast equivalent phantoms were used. The black dots indicate the positions where SF were measured. The distance between the ticks on the horizontal and vertical rulers is 2 cm. (b) Image of 12 mm diameter Pb-disks exposed on top of a breast in the MLO position. Breast thickness is shown in the upper right corner. (c) SF as a function of breast thickness in 0° projection images of 50% glandular-50% adipose breast equivalent phantoms (open triangles) and six clinical breast images (solid diamonds).

Shown are $kV_{\text{equivalent}}$ and $Al_{\text{equivalent}}$ of the simulated spectra for a nominal kV that results in the smallest χ^2 . The measured and simulated estimates of the HVL and QVL are also presented. The simulated values are those that minimize the χ^2 . The results in both tables demonstrate that the extrapolation of the Boone's spectral models agree well with our measurements.

3.2 Scatter

Figure 1a and b show the geometry used for the scatter measurements in the breast tissue-equivalent phantoms and in the patient data. Using the method of extrapolating the SF to zero disk diameter in breast equivalent phantoms demonstrates that scatter fraction increases with thickness, as expected. We measured SF = 0.29 for a 20 mm phantom, 0.43 for a 40 mm phantom, 0.52 for a 60 mm phantom, and 0.57 for a 80 mm phantom as measured near the center of the phantom.

Figure 1c illustrates SF derived from the shadows under 12 mm Pb-disks as a function of breast thickness. The SF correspond to the various positions in the field of view as indicated in Fig 1a and b. This analysis shows that the SF in real mammograms are similar to the SF measured in breast-equivalent phantoms for corresponding thicknesses.

Figure 2 shows the extent to which the iodine concentration will be underestimated if a correction for scatter is not applied. The amount by which the iodine concentration will be underestimated is dependent upon the breast thickness. Consider, for example, the situation were the breast has an actual iodine concentration of 2 mg/cm². Failure to correct for scatter will result in an error in the estimated iodine concentration of 29% for a 20 mm thick compressed breast and 50% for a 80 mm thick compressed breast. Note that even if images are produced with a grid, the iodine concentration is still underestimated. This has relevance for those attempting to perform contrast-enhanced digital mammography.

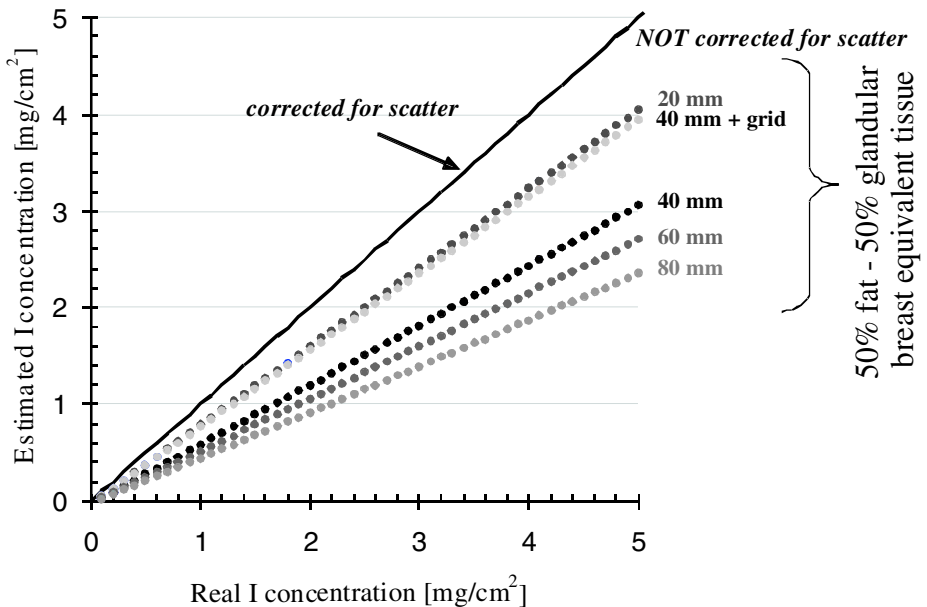


Fig. 2. Iodine concentration will be underestimated if not corrected for scatter. The simulation used a Rh target, 49 kV and 0.27 mm Cu filter. No grid was used if not specified.

3.3 Patient Motion

Figure 3 shows a clinical example of patient motion. The image was produced by subtracting a post-contrast reconstructed image of the breast from a pre-contrast reconstructed image. Two lead BBs are shown attached to the skin near the nipple. The arrows indicate patient motion. In our clinical trial, we consistently noted the greatest motion in the dependent (lower) portion of the breast.



Fig. 3. Example of patient motion

We have attempted to estimate the magnitude of motion artifacts by simulating breast motion. Figure 4 illustrates the influence of displacements simulating patient motion on the relative SI variation and equivalent iodine concentration. The data were calculated from images of 12 women. As an example, 25% of the 6 mm displacements have on average a 1% relative SI variation; this corresponds with a 0.5 mg/cm^2 iodine uptake. However, it is relevant to note that a displacement of as little as one pixel can result in more than a 5% change in signal intensity, which can potentially exceed the anticipated signal from the iodine contrast agent. As such, it is imperative that motion be minimized.

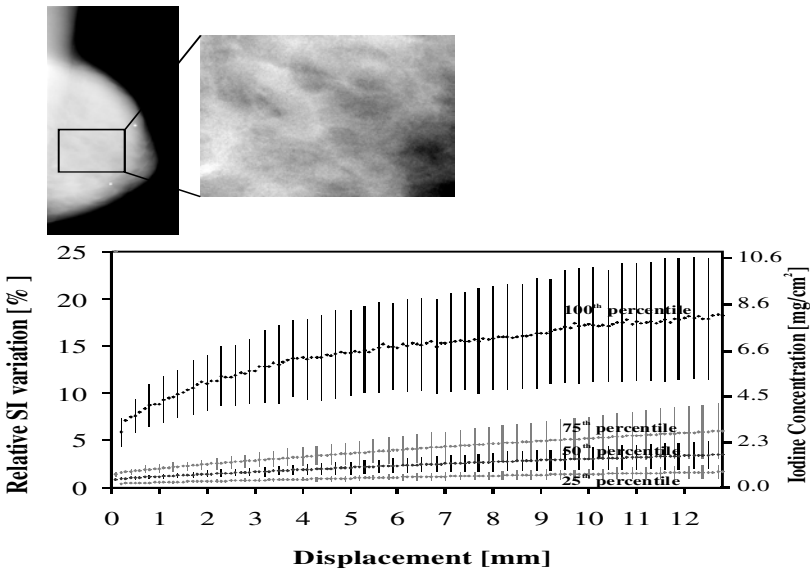


Fig. 4. Example of a ROI extracted from a projection mammogram acquired with a Rh-target x-ray tube at 49 kV with 0.27 mm Cu filtration (left). Relative SI variation between pixel displacements and the corresponding equivalent iodine concentration from 12 projection images are shown (below). The error bars represent standard deviations.

4 Conclusion

CE-DBT offers the potential to visualize the vascular characteristics of breast lesions as an adjunct to mammography. Based upon our initial clinical experience, and the work reported here, it is clear that the quantization of the iodine uptake for CE-DBT is complex. For the design of a CE-DBT system, attention should be paid to scatter and patient motion. At the current time, we are working on the reduction of patient motion and we are evaluating alternative subtraction methods using dual energy CE-DBT. We expect that these may minimize patient motion artifacts.

Acknowledgements

This work was funded in part by NIH grant PO1 CA85484 and a Philips Medical Systems/RSNA Research Seed Grant.

References

- [1] Carton A-K, Li J, Albert M, *et al.* Quantification for contrast-enhanced digital breast tomosynthesis. In: Flynn MJ, Hsieh J, editors. *Medical Imaging 2006: Physics of Medical Imaging*; p. 111-121.
- [2] Jong RA, Yaffe MJ, Skarpathiotakis M, *et al.* Contrast-enhanced digital mammography: Initial clinical experience. *Radiology* 2003;228:842-850.
- [3] Skarpathiotakis M, Yaffe MJ, Bloomquist AK, *et al.* Development of contrast digital mammography. *Medical Physics* 2002;29(10):2419-26.
- [4] Maidment ADA, Adelow L, Blom O, *et al.* Evaluation of a Photon-Counting Breast Tomosynthesis Imaging System. In: Flynn MJ, editor. *Physics of Medical Imaging, Proc. SPIE 6142*; 2006.
- [5] Wu T, Moore RH, Rafferty EA, *et al.* Breast tomosynthesis: Methods and applications. In: Karellas A, editor. *RSNA Categorical Course in Diagnostic Radiology Physics: Advances in Breast Imaging - Physics, Technology, and Clinical Applications*; 2004. p. 149-163.
- [6] Dobbins JT, 3rd, Godfrey DJ. Digital x-ray tomosynthesis: current state of the art and clinical potential. *Physics in Medicine & Biology* 2003;48(19):R65-106.
- [7] Niklason LT, Christian BT, Niklason LE, *et al.* Digital tomosynthesis in breast imaging. *Radiology* 1997;205(2):399-406.
- [8] Boone JM, Fewell TR, Jennings RJ. Molybdenum, rhodium, and tungsten anode spectral models using interpolating polynomials with application to mammography. *Medical Physics* 1997;24(12):1863-74.

P42-7: X-RAY POLARIZATION IMAGING

Andrew D. A. Maidment, Ph.D., Michael Albert, Ph.D., and Yan-Hong Kao, Ph.D.
Department of Radiology, University of Pennsylvania, Philadelphia, PA
E-mail: andrew.maidment@uphs.upenn.edu

X-rays are transverse waves; thus, one can preferentially produce x-rays in one polarization state. Passing through biological tissue, this state of polarization may be changed. Since x-rays are capable of passing through many inches of tissue, changes in the polarization state can reflect information about the tissue deep inside the body. Conventional mammography is possible because some materials absorb x-rays more than others; thus, the x-ray energy must be deposited in the body to produce an image. With polarization imaging it may be possible to produce mammographic images with the additional potential of imaging breast function and composition. Moreover, the rotation of the polarization of x-rays is accumulated by passage of the x-rays through the breast, not by attenuation. Thus, while speculative, it may be possible to significantly reduce the dose needed to image the breast.

We have investigated two potential methods of measuring x-ray polarization, comparing broad spectrum and mono-energetic x-ray sources. We first conducted experiments using the method of Barkla. A Lucite rod was positioned 40 cm from a collimated tungsten target x-ray tube. Two ion chambers were mounted at right angles to the beam, and at right angles to each other 60 cm from the analyzer. The primary photon fluence incident upon the analyzer was 2×10^{11} , the scattered fluence was 2×10^6 cm⁻², and the x-ray polarization was measured to be $P_{pol} = 0.10$. Thus, while the fluence was high giving good statistics, the fraction of the beam that was polarized was small.

The second design used a molybdenum-target x-ray source and a calcite crystal placed at 45° to the x-ray beam. The calcite reflects the K α radiation at a Bragg angle of 45° (reflected beam is emitted at 90°) on the 11 0 1 plane of the crystal. This has the advantage that the reflected beam is 100% polarized. However, there are two problems with this technique. First, only a small fraction of the incident x-rays are so reflected, thus the signal recorded is very weak. Secondly, the x-rays scattered by the sample need to be scattered at close to 90° to show 100% polarization. This further reduces the number of scatter events that can be successfully recorded. As a result, we were unable to convincingly demonstrate polarization effects. As a result, we have now decided to pursue the first of the two designs for the polarimeter.

This research, while quite fundamental in its nature, has the potential for a significant impact in breast cancer diagnosis. The use of effects related to the polarization of x-rays is a largely unexplored field. Thus imaging based on this mechanism would represent a new way of non-invasively studying the human body.

The U.S. Army Medical Research and Materiel Command under DAMD17-02-1-0593 supported this work.

P42-8: ALGORITHMIC CORRELATION OF LESION LOCATION ON FILM SCREEN MAMMOGRAPHY AND BREAST ULTRASOUND – INITIAL RESULTS

LTC M. P. McNamara Jr. and S. Izen
Case Western Reserve University, Cleveland, OH; Uniformed Services University of the Health Sciences, Bethesda, MD
E-mail: michael.p.mcnamara@us.army.mil

Background: Imaging evaluation of breast abnormalities is done primarily with mammography and ultrasound. These modalities are complementary and concordance of examination findings is critically important to quality patient care. In day-to-day practice, it can be difficult to be certain that the same lesion is being imaged by both examinations, since mammographic views are done with the patient upright and yield two dimensional coordinates whereas an ultrasound exam is done with the patient supine and location is expressed in clockface position and distance from the nipple.

Objective/Hypothesis: Mathematical analysis and cross-correlation of lesion location using a large, unambiguous 'real-world' data set of breast masses with known locations can allow development of a software algorithm that can predict lesion location, on ultrasound, given knowledge of the spatial coordinates on mammography.

Results: Although the work is in-progress and ongoing, we have devised an algorithm that predicts the ultrasound location of a mass on seen on mammography to within, on average, approximately 1.1 hours and 1.7 cm from the location actually found by sonographic examination of the patient under controlled conditions.

Conclusions: It is possible to mathematically predict, from a mammogram, where a lesion is to be found when the patient is subsequently examined with ultrasound. As we refine this algorithm our goal is to lower the margin of error to 1 hour and 1cm from predicted location to actual location.

The U.S. Army Medical Research and Materiel Command under W81XWH-04-1-0625 supported this work.

P42-9: COMPARISON OF IMAGE QUALITY AMONG VARIATIONS IN SPECIMEN TISSUE COMPRESSION USING DIFFRACTION ENHANCED IMAGING

C. A. Parham and E. D. Pisano
University of North Carolina at Chapel Hill, Chapel Hill, NC
E-mail: christopher_parham@med.unc.edu

Purpose: Previous studies utilizing the Diffraction Enhanced Imaging (DEI) method have demonstrated significant improvements in breast tissue visualization when compared with conventional mammography systems. Contrast in DEI is obtained not only from x-ray absorption, as with conventional x-ray systems, but also from x-ray refraction and ultra-small angle scatter (extinction). One of the primary reasons for breast tissue compression is to reduce x-ray scatter, a degrading factor which is almost entirely eliminated in DEI through the use of a silicon analyzer crystal. Efforts are currently underway to translate this synchrotron based technology to a more clinically realistic imaging system. This study investigates structural visualization as a function of tissue compression using DEI when compared to digital mammography.

Materials and Methods: Four mastectomy specimens containing characteristic benign and malignant features were selected for imaging at the National Synchrotron Light Source, Brookhaven National Laboratory. All tissues are mounted using Lucite immobilization plates and immersed in water to reduce the density gradient between the air and tissues. All DEI images were acquired at a beam energy of 30 keV and imaged in an uncompressed, half-compressed, and fully compressed configuration. Comparison images were acquired using a conventional digital mammography system.

Results: Initial data indicates that images acquired in certain DEI configurations are not significantly different in the uncompressed, half compressed, and fully compressed configurations. A radiologist reader study is currently underway to determine the relative differences between the possible DEI configurations.

Conclusions: Initial data indicates that DEI has the potential for breast imaging with reduced compression, but the use of in vitro mastectomy specimens limits the generalization of the study to in vivo breast imaging. However, the limited subset of mastectomy specimens used in this study provides insight into the need for compression in this multi-parameter imaging modality. The use of x-ray refraction in addition to x-ray absorption allows for imaging at higher x-ray energies, dramatically reducing absorbed dose.

The U.S. Army Medical Research and Materiel Command under DAMD17-02-1-0523 supported this work.

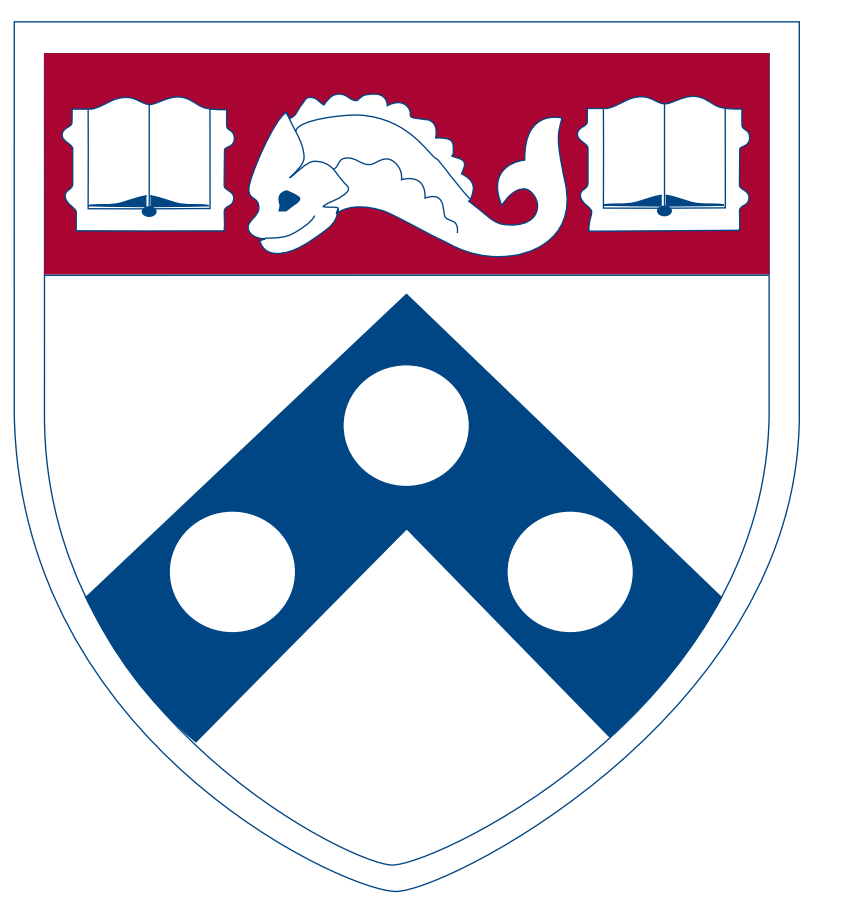
P42-10: TASK-SPECIFIC OPTIMIZATION OF MAMMOGRAPHIC SYSTEMS

R. S. Saunders and E. Samei
Departments of Physics and Radiology, Duke University, Durham, NC
E-mail: rss@duke.edu

Purpose: While Full Field Digital Mammography (FFDM) systems present several logistical advantages over traditional film-screen systems, it has not been proven whether these systems allow for a higher detection of breast cancer. Simulation methods allow one to separate the effects of different resolution, noise, and efficiency on the detection of breast lesions. This research created a framework to simulate the acquisition, image processing, and display of digital mammography images. By applying this simulation framework to a variety of clinical questions, one may optimize digital mammographic imaging for the specific task of breast cancer detection.

Methods and Materials: Accurate simulations require precise measurements of the physical characteristics of mammography systems. First, we developed characterization routines that determined the Modulation Transfer Function (MTF), Normalized Noise Power Spectrum (NNPS), and Detective Quantum Efficiency (DQE), which describe the resolution, noise, and signal to noise performance, respectively. Those routines were applied to a thorough analysis of a selenium-based direct full-field mammography detector for several x-ray beam qualities. In addition, these routines were used to analyze the resolution and noise of several medical display devices, including both Cathode Ray Tube (CRT) and Liquid Crystal Display (LCD) devices. These measurement data were applied to later simulation routines.

The first stage in mammographic simulation necessitated the modeling of breast masses and calcifications. Using this model, a simulation routine was created that inserted a simulated lesion in a normal anatomical background. The next stage modified the resolution and noise of the images to reflect the physical characteristics of the detector. In addition, the routines adjusted image contrast to account for scattered radiation. The next procedure processed the images to increase large-scale contrast and fine detail. Finally, routines adjusted image resolution according to the given display device. Observer models were utilized to detect the breast lesions under a variety of imaging conditions.



Introduction

X-rays are transverse waves; thus, one can preferentially produce x-rays in one polarization state. Passing through biological tissue, this state of polarization may be changed. Since x-rays are capable of passing through many inches of tissue, changes in the polarization state can reflect information about the tissue deep inside the body. Conventional mammography is possible because some materials absorb x-rays more than others; thus, the x-ray energy must be deposited in the body to produce an image. With polarization imaging it may be possible to produce mammographic images with the additional potential of imaging breast function and composition. Moreover, the rotation of the polarization of x-rays is accumulated by passage of the x-rays through the breast, not by attenuation. Thus, while speculative, it may be possible to significantly reduce the dose needed to image the breast.

Background

Polarization and Optical Activity:

Most biological materials are optically active to visible light. Like other materials, optically active materials can refract, absorb and scatter light, but in addition they respond differently to radiation, depending upon whether it is left or right circularly polarized. The differential absorption of light of these two polarizations is called circular dichroism, and the differential refraction is called circular birefringence, which for plane-polarized light is observed as optical rotation. Plane polarized light is composed of equal amplitudes of left- and right-polarized light. The magnitude of the optical rotation of plane-polarized light is proportional to the difference between the indices of refraction for left and right circularly polarized light and the thickness of the optically active material.

X-ray Polarization

Like other forms of electromagnetic radiation, x-ray photons can exhibit phenomena related to polarization. Bremsstrahlung x-rays produced by electrons accelerated from the cathode to the anode of an x-ray tube are partially plane-polarized with the electric field vector parallel to the cathode-anode axis [Dyson90, Agar79]. Classically, an accelerating or decelerating charged particle emits radiation whose electric field vector (at each point in space) is coplanar with the axis of acceleration or deceleration [Barut80, Rohr65, Schwing98, Jackson99]. The physical reason for this geometric fact is clearer in the related process of an electron being scattered by a photon, as it is the electric field of the incident (or emitted) photon which is chiefly responsible for accelerating (or decelerating) the electron. By way of comparison, synchrotrons produce coherent, circularly polarized radiation.

The Bremsstrahlung radiation of diagnostic x-rays is on the order of 5-10% polarized, with greater polarization for x-rays whose energy is nearly that of the incident electron. Lower energy x-rays are produced by processes in which the electron's direction might have changed prior to emission of the x-ray, and thus have less polarization. These effects were experimentally documented as early as 1905 [Barkla05], as reviewed in [Steve57]. More recent research has tended to deal with thin targets (for example, [Kuck73]) so that the kinematics at the interaction vertex are well defined. A measurement of polarization from a Phillips x-ray tube [Staun78], in a study aimed at crystallographic applications, showed general agreement with the older results. Similar agreement was reported in an abstract [Slivin71].

We have investigated two potential methods of measuring x-ray polarization, comparing broad spectrum and mono-energetic x-ray sources. Here we present our work to date on these methods.

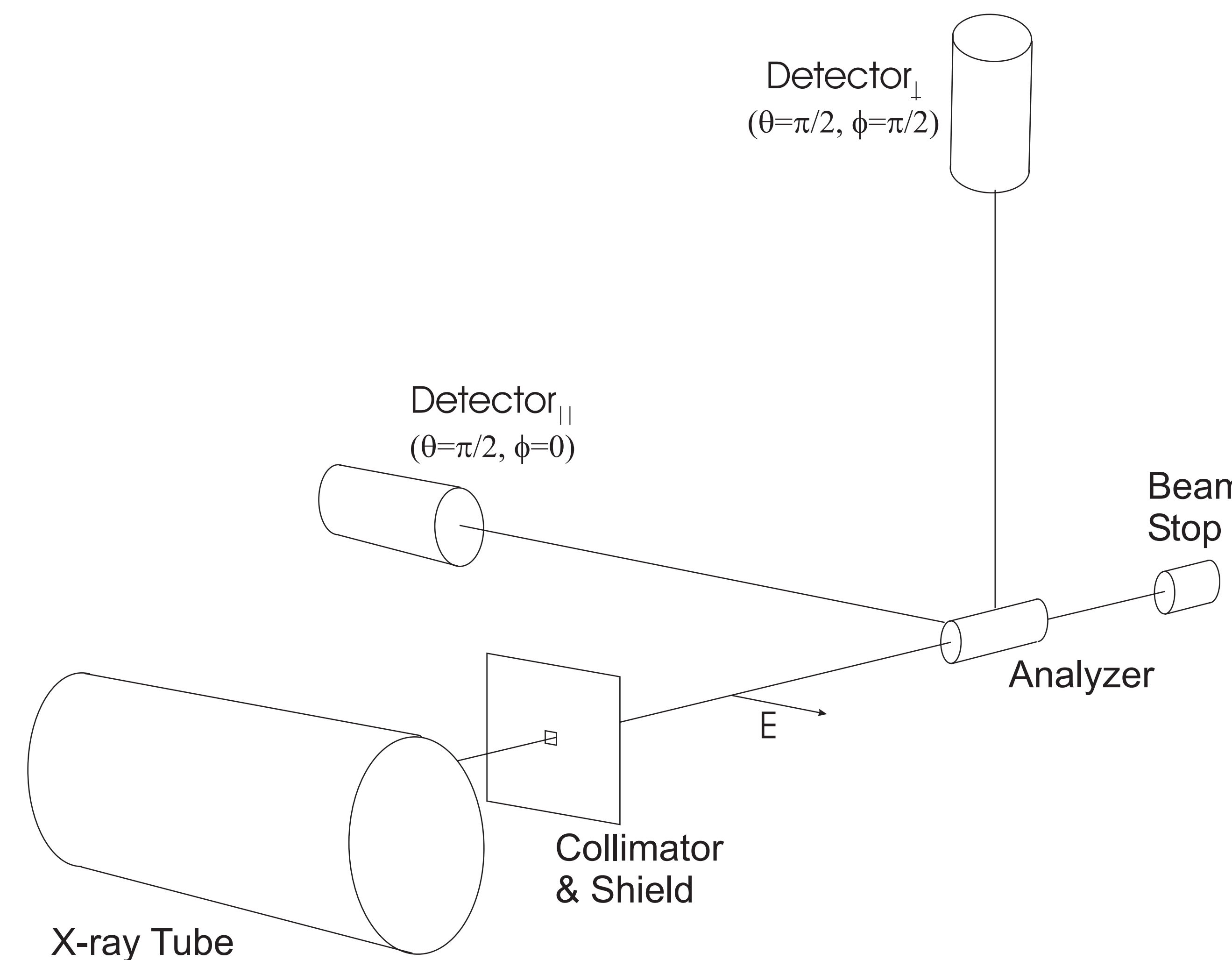
References

- [Agar79] B.K. Agarwal, X-Ray Spectroscopy, Springer-Verlag (1979).
- [Barkla05] Barkla, C.G., Phil. Trans. Roy. Soc., 204, 467 (1905).
- [Barut80] Barut, A.O., Electrodynamics and classical theory of fields and particles, Dover (1980).
- [Dyson90] Dyson, N.A., X-Rays in atomic and nuclear physics, 2nd ed., Cambridge University Press (1990).
- [Hart81] Hart M. and Rodrigues, A.R.D., Phil. Mag. (1981), B43, 321.
- [Itzak80] Itzykson, C. and Zuber, J.-B., Quantum Field Theory, McGraw-Hill (1980).
- [Jackson99] Jackson, J.D., Classical Electrodynamics, Wiley (1999).
- [Johns83] Johns, H.E. and Cunningham, J.R., The Physics of Radiology, Thomas (1983).
- [Kuck73] Kuckuck, R.W. and Ebert, P.J., "Linear Polarization of Low-Energy-Electron Bremsstrahlung", Phys. Rev. A (1973), 7, 456-462.
- [Rohr65] Rohrlch, F., Classical charged particles, Addison-Wesley (1965).
- [Schwing98] Schwinger, J., L.L. DeRaad, Jr., K.A. Milton, and W. Tsai, Classical Electrodynamics, Perseus Books, Reading, Massachusetts (1998).
- [Slivin71] Slivinsky, V. W., Am. Phys. Soc. Bull. (1971), 16, 546 (Abstract).
- [Staun78] Staun., J. et. al., "Influence of Polarization of the Incident Beam on Integrated Intensities in X-ray Energy-Dispersive Diffractometry", Acta. Cryst. (1978), A34, 84-87.
- [Steve57] S. Town Stephenson, "The Continuous X-Ray Spectrum", in Encyclopedia of Physics, S. Flügge, ed., Vol. XXX X-Rays, Springer-Verlag (1957).

Research Funded by the U.S. Army Medical Research Materiel Command grants DAMD 17-02-1-0593.

Design 1: Polychromatic X-ray Polarimeter

This design relies upon the angular distribution of the scattered beam to measure the polarization of the incident beam.



The polarimeter consists of a collimated x-ray tube, an analyzer, and two x-ray detectors at right angles. To measure polarization rotation by a sample material, the material must be placed in the primary beam, and the detectors must be mounted on a rotating gantry. In such experiments, the intensity of the scattered radiation recorded by the detectors would have a sinusoidal angular dependence.

Theory of Operation

The angular dependence of x-rays scattered from a polarized beam can be understood at the classical level. If a plane-polarized wave is incident upon a charged particle, the resulting acceleration a of the particle will be parallel to the electric vector E_{in} of the incident wave. The electric field component of the resulting scattered radiation at a distance R away from the scatterer in the direction \hat{n} (a unit vector) will be proportional to $\hat{n} \times (\hat{n} \times \mathbf{a}) / R$ [Barut80, Rohr65, Schwing98, Jackson99]. This formula has a simple geometric interpretation in that the electric field vector is proportional to the acceleration projected onto a plane perpendicular to the line of sight from the field point back to the scatterer. For a wave moving along the z-axis and plane polarized so that the electric vector lies along the x-axis (parallel to the anode-cathode axis), the angular distribution of scattered radiation per solid angle will have the form

$$d\Phi/d\Omega = r_o^2 \left[-\sin^2(\theta) \cos^2(\phi) \right]$$

where θ is the polar angle ($0 < \theta < \pi$) and ϕ is the azimuthal angle ($0 < \phi < 2\pi$).

The azimuthal variation is maximal for scattering at 90° relative to the incident radiation ($\theta = \pi/2$). In this plane, scattering would be 100% suppressed at $\phi = 0$ or π (the direction of the electric field vector E_{in} of the incident beam) if the beam were completely polarized. For incompletely polarized beams, the azimuthal variation will be less pronounced. Using radiation scattered at 90° , if $I_{||}$ represents the intensity of the scattered radiation in the direction parallel to the preferred direction of the electric field vector ($\phi = 0$) and I_{\perp} represents scattering in the orthogonal direction ($\phi = \pi/2$), the degree of planar polarization of the incident beam can be quantified in terms of

$$P_{pol} = \frac{(I_{\perp} - I_{||})}{(I_{\perp} + I_{||})}$$

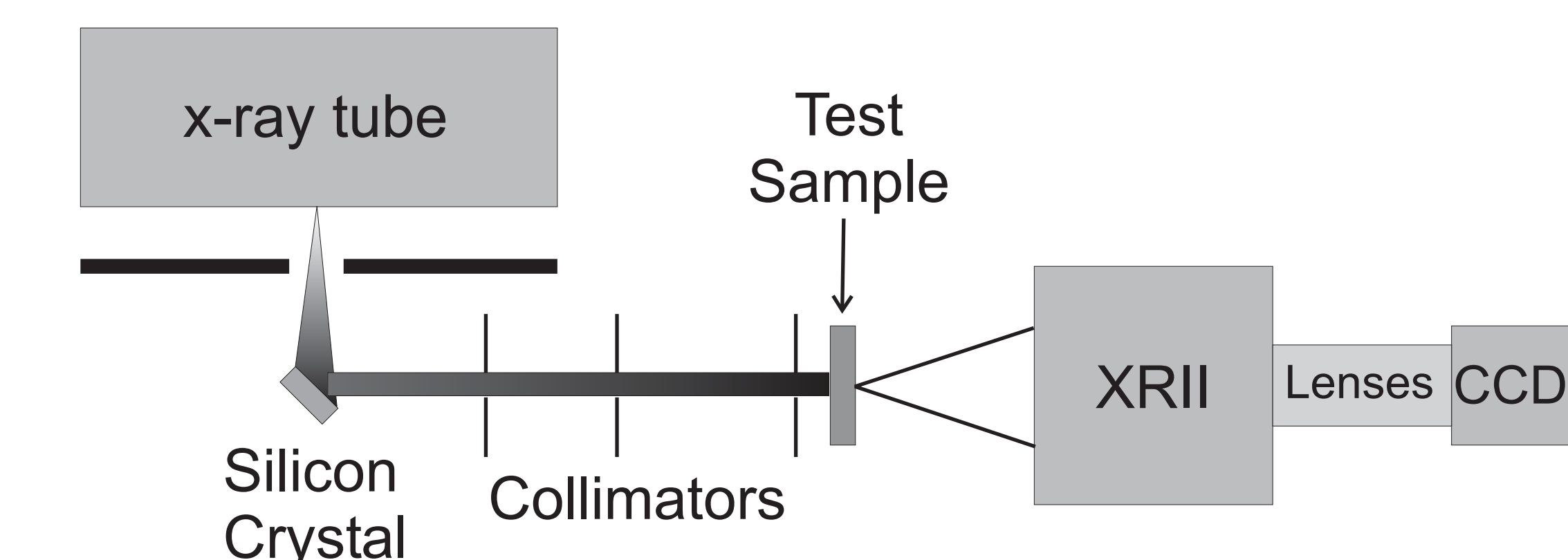
which would be 1 for a completely plane-polarized beam and is on the order of 0.05-0.1 for conditions similar to clinical x-ray tubes.

Results

We have conducted experiments using an analyzer consisted of a Lucite rod 2.5 cm diameter, and 13 cm long. The analyzer was positioned 40 cm from a tungsten target x-ray tube (Siemens Bi 150/30/50R), operated at 100 kVp and 100 mAs. The x-ray beam was collimated by a 6 mm diameter circular aperture, located 20 cm from the x-ray source. Thus, the irradiating beam was 12 mm in diameter at the analyzer. Two ion chambers were mounted at right angles to the beam, and at right angles to each other ($\theta = \pi/2$, $\phi = 0$ and $\pi/2$), 60 cm from the analyzer. The primary photon fluence incident upon the analyzer was estimated to be 2×10^{11} , while the scattered fluence at the detector in the direction perpendicular to polarization was $2 \times 10^6 \text{ cm}^{-2}$. In this geometry, we have observed x-ray polarization, measuring $P_{pol} = 0.10$.

Design 2: Pseudo-Monochromatic X-ray Polarimeter

We have also examined a polarimeter design based on a molybdenum x-ray source and a silicon crystal placed at 45° to the x-ray beam. The calcite will reflect the $K\alpha$ radiation at a Bragg angle of 45° (reflected beam is emitted at 90°) on the 11 11 11 plane of the crystal, so that the reflected beam is 100% polarized.

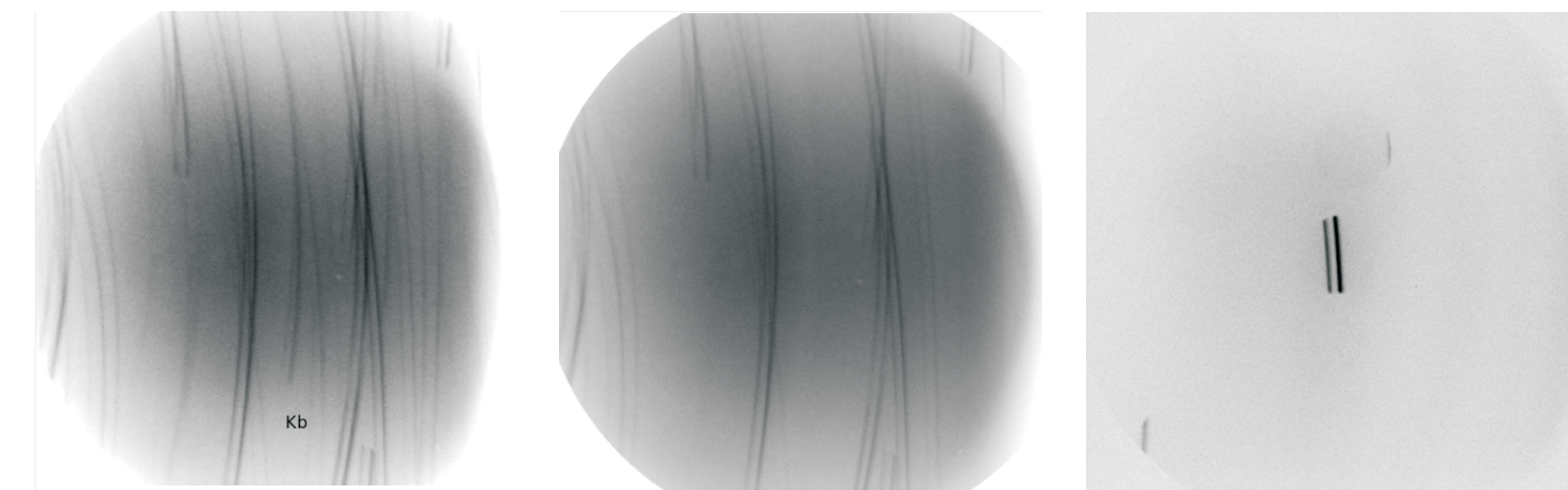


The x-ray tube produces a poly-energetic spectrum. The silicon crystal reflects the $K\alpha$ radiation ($\sim 17.3 \text{ keV}$) at 90 degrees. This polarized, mono-energetic beam is passed through a series of collimators and hits the test sample. The test sample then scatters the incident x-rays. The angular distribution of the scattered x-rays varies due to the x-ray polarization. This image is produced with the x-ray image intensifier (XRII) and then recorded by the CCD.

Theory of Operation

This design has the advantage that rather than attempting to measure changes in polarization with a signal of $\sim 10\%$, the signal has 100% amplitude. There are two problems with this technique. First, only a small fraction of the incident x-rays are so reflected, thus the signal recorded is very weak. Secondly, the x-rays scattered by the sample need to be scattered at close to 90° to show 100% polarization. This further reduces the number of scatter events that can be successfully recorded.

Results



The images above show the energy resolved x-ray spectra from a single crystal of silicon. The leftmost image is acquired with the crystal at 45° . Multiple reflections of the $K\alpha$ and $K\beta$ lines of molybdenum from different crystal planes are shown. In addition, there is a general background signal from the molybdenum bremsstrahlung spectrum. The center image is acquired under the same geometry, with a niobium filter in the reflected beam. Now, the $K\beta$ lines (19.6083 keV) have been removed, as the k-edge of Niobium (18.986 keV) is of a lower energy. Finally, a collimated image of the $K\alpha 1$ (17.4793 keV) and $K\alpha 2$ (17.3743 keV) are shown. The reflection from the 11 11 11 crystal plane for the $K\alpha$ reflection occurs at 45.9179° and the $K\beta$ reflection occurs at 46.2767° , thus the x-rays in this collimated beam are essentially 100% polarized.

Conclusions

Work on developing the polarimeters is ongoing. Both devices provide challenges that still need to be overcome. The polychromatic design has the benefit of substantially higher fluence through the specimen and hence incident upon the analyzer crystal. However, as only 10% of the x-ray beam is polarized, the resulting signal variation due to optical activity is difficult to detect. On the other hand, the monochromatic polarimeter design allows use of an interrogating x-ray beam which is 100% polarized. Unfortunately, the fluence rate is low, and hence the detected scattered signal is also low.

Contact Info:

Please direct inquiries to Dr. Andrew Maidment, Andrew.Maidment@uphs.upenn.edu.